Summer 7-18-2014

A Molecular Picture of Biofuel Decomposition: Pyrolysis of Furan and Select Furanics

Kimberly Noelle Urness
University of Colorado Boulder, Kimberly.Urness@colorado.edu

A Molecular Picture of Biofuel Decomposition:

Pyrolysis of Furan and Select Furanics
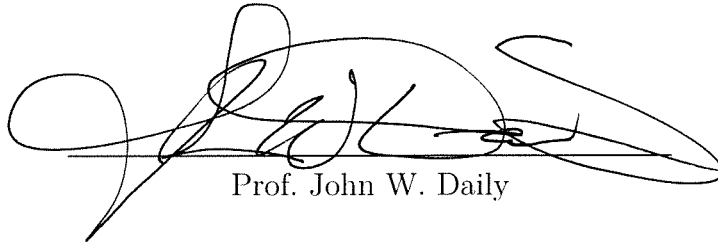
by

Kimberly N. Urness

B.S., University of St. Thomas, St. Paul, MN (2007)

M.S., University of Colorado, Boulder, CO (2010)
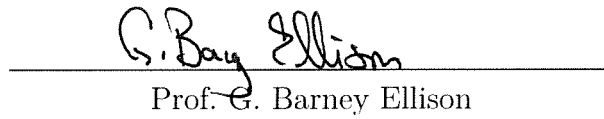
A thesis submitted to the

Faculty of the Graduate School of the

University of Colorado in partial fulfillment

of the requirements for the degree of

Doctor of Philosophy

Department of Mechanical Engineering

2014

This thesis entitled:
A Molecular Picture of Biofuel Decomposition:
Pyrolysis of Furan and Select Furanics
written by Kimberly N. Urness
has been approved for the Department of Mechanical Engineering

Prof. John W. Daily

Prof. G. Barney Ellison

Date _11 July 2014_

The final copy of this thesis has been examined by the signatories, and we find that both the content and the form meet acceptable presentation standards of scholarly work in the above mentioned discipline.

Urness, Kimberly N. (Ph.D., Mechanical Engineering)

A Molecular Picture of Biofuel Decomposition: Pyrolysis of Furan and Select Furanics

Thesis directed by Prof. John W. Daily

Limited fossil fuel resources and climate impacts due to carbon dioxide emissions have made it critical that we use renewable, carbon-neutral fuels. Biomass, in the form of crop waste or the inedible portion of plants, has the potential to be a renewable and economical source of energy. Recent developments in the conversion of lignocellulosic biomass have sparked an interest in the production of biofuels and valuable platform chemicals, synthesizing molecules such as alkylated furans, furanic ethers, and various lactones. Early studies indicate that many of these potential furanic and lactonic fuels have similar properties to gasoline or diesel, however, little is known about their pyrolytic and combustion behavior.

In order to establish a molecular picture of the first thermal products formed from the pyrolysis and oxidation of furanic biofuels, a microtubular flow reactor was used to thermally decompose furan, 2-methoxyfuran, and select lactones. Dilute samples of these molecules were entrained in He or Ar and thermally cracked in a heated silicon carbide microreactor. Products, including radicals and metastables formed at early pyrolysis times ($50-200\ \mu$s), were detected by 118.2 nm (10.487 eV) photoionization mass spectrometry (PIMS), tunable synchrotron vacuum ultraviolet PIMS and Ar matrix infrared spectroscopy. As most initiation rates need to be calculated because they are too difficult to measure, the experimental results presented in this thesis demonstrate progress towards validating these calculations, aiding in the development of accurate initiation chemistry for kinetic mechanisms.

The published mechanism for pyrolysis of furan (C_4H_4O), the parent compound of the more complicated furans described above, involves decomposition *via* a pair of carbenes. The product branching ratio of this reaction was measured over a range of temperatures and compared to predictions of three published furan kinetic mechanisms. A higher-energy

radical channel that produces propargyl radical (HCCCH$_2$) and H-atom was also detected and quantified.

The unimolecular and low-pressure bimolecular decomposition mechanisms of the simplest furanic ether, 2-methoxyfuran, were also studied. Recent electronic structure calculations indicate this substituted furan has an unusually weak O$-$CH$_3$ bond, which results in bond scission and the production of CH$_3$ and 2-furanyloxy radicals. The final products detected from the ring opening of 2-furanyloxy radical include 2 CO, HCCH and H. Secondary products resulting from H or CH$_3$ addition to the parent and radical reactions with 2-furanyloxy were also detected and include CH$_2$=CH-CHO, CH$_3$-CH=CH-CHO, CH$_3$-CO-CH=CH$_2$ and furanones. In addition to detection and quantification of the primary pyrolysis products, this work also includes the first experimental characterization of 2-furanyloxy radical by the assignment of several vibrational bands in an Ar matrix and a low-resolution estimate of the ionization threshold of this allylic lactone. Finally, the pyrolysis products of the lactones 2(5H)-furanone, 2(3H)-furanone and α-angelica lactone (5-methyl-2(3H)-furanone) were identified by 118.2 nm PIMS and Ar matrix IR spectroscopy as these species were also shown to be relevant to the decomposition of 2-methoxyfuran.

Furans and lactones are among a variety of molecules derived from non-edible biomass that offer a renewable path to biofuels. Since the pyrolytic behavior of these oxygenated fuels are not well-known this work contributes to the field by identifying the first thermal products, helping to elucidate possible chemical mechanisms for emission formation from these biofuels.

Acknowledgements

Since this is my doctoral thesis, and just a few (we'll call them short) years ago I was writing a master's thesis, the first people I absolutely have to thank are my co-advisors Profs. Barney Ellison and John Daily for taking me back into the program and giving me the opportunity to finish this beast that is a doctorate. Along those lines I also want to thank my former lab mates Beth Reed and AnGayle (AJ) Vasiliou for being instrumental in convincing me it was the right thing to do. Ever since undergrad, I've been a bit of an academic loner...I'm neither a full-blooded chemist nor engineer, but instead something of a hybrid. I still haven't quite figured out where these roles will take me, but I'm confident I'll make it work.

John and Barney, you have been a great advising team and I'm so lucky to have been able to work with both of you as you have such different sets of expertise. John, one thing in particular that stands out is how you've continually encouraged me to get out of my comfort zone. I'm grateful to you for sending me to conferences right away in my graduate career, long before I was mentally ready for it. You've also given good advice on how to sell the science, which will no doubt be valuable throughout my career. Barney, thanks for training me to become a better chemist while in the process making me laugh. From day 1 the Ellison lab has been an enjoyable place to work, in large part because the science is just plain fun, but also because I never quite know what to expect. I appreciate how available you have been and excited to discuss the latest research results.

The Ellison group members have made a huge impact on my graduate experience. AJ, thanks for being both my teacher and my friend over the years. I learned so much from you

and I'm grateful for the time and enthusiasm you gave to me in lab. From time to time I still bring up to half a dozen little containers to the lunch table, and it always makes me smile thinking about how you made fun of me. Luis Cuadra-Rodriguez...aka Alberto...what else can I say, PB-gays. Your smart-assed comments have been missed around the lab since you left. Beth Reed, the "fearless postdoc" as AJ liked to say...book club has disintegrated since you left Boulder...and I still think it's wild you and Alberto got hitched and had a baby! Jong Kim, I enjoyed your goofy Korean attitude in the lab. Talking with you at lunch made me realize how much of my vocabulary is slang! Oh American English. I wish you the best of luck in Taiwan. Thanks also go out to Josh Baraban for helping me diagnose my PIMS issues...without that smidgen of insight who knows if I would be writing this thesis! You've also been a good lunch buddy - I've enjoyed our chats and laughs. Adam Scheer, I enjoyed your positive attitude in the lab and during recent ALS visits...you are an eloquent speaker and writer, so much to Barney's dismay, you will make it in the policy world. Tom Ormond, you're a careful spectroscopist and do good work - hopefully you will have the opportunity to take over more light sources in the future! And of course the newest members: Jessie Porterfield and Grant Buckingham. It's been fun having you in the lab...you both have such positive energy and an eagerness to make things work better...keep it up - don't lose steam! Jessie, it's been fun working with you and learning how to be a teacher. Grant, I enjoy your goofy attitude and your crazy-ridiculous whistling abilities. Good 'ole Whistling Jack.

Qi Guan, from the first day I met you I knew we'd get along. I don't remember the exact words you used, but when you introduced yourself to me in our old office you said something along the lines of "my name is Qi, glad to be your friend"...it was super cute. I'd also like to think I have a better understanding of fluid dynamics thanks to you. Bret van Poppel - you were a big part of my first few years here in Colorado and I feel like I learned a lot about how the world works thanks to you. Your energy and enthusiasm are unparalleled; I miss our coffee chats and the sort of "take over the world" attitude that you brought to almost every endeavor.

In addition, no experiment in the Ellison lab would ever have worked if it wasn't for the CIRES shop: Don David, Jim Kastengren, Ken Smith and Yehor Novikov. Don, I tried to take in as much of your infinite knowledge as I could in my time here at CU; however the breadth of knowledge you possess is deep and I will miss being able to walk down the hall to ask you and the rest of the crew for help.

I'd also like to thank the many scientists and collaborators I've had the opportunity to work with and learn from over the years. The Advanced Light Source (ALS) has been an amazing part of my graduate experience...some of the most exhausting times but also the most rewarding. For this I'd like to thank the ALS/California crew: Amir Golan, Tyler Troy, Musa Ahmed, and David Osborn. Amir and Tyler - I can't thank you enough for the time and energy you put into ensuring our ALS visits were a success. I'd also like to thank John Simmie for helpful discussions these last few months and for looking over my last couple thesis chapters. John Stanton for frequent visits to Boulder and for assistance on ALS data analysis, and of course Mark Nimlos and David Robichaud at NREL for their expertise and laboratory assistance.

The ion supergroup including Professors Veronica Bierbaum, Mathias Weber, Carl Lineberger and graduate students provided an encouraging environment to present my latest and greatest research endeavors. Although giving a presentation is not my idea of a good time, the talks I gave at supergroup were always the most enjoyable. I'd also like to specifically acknowledge Ronnie for her kind yet inquisitive demeanor. Thanks for giving my thesis a thorough read..and of course how can I forget the weekly bagels...they never failed to brighten my day.

In the mechanical engineering department I'd like to thank Sharon Anderson for being the best graduate advisor on campus (and she has the awards to prove it). You alway know what's going on and are happy to help...a great combination of skills. I'd also like to thank Professor Michael Hannigan for being both a mentor and a friend. You gave me the opportunity to work on GEARS which was seriously the best thing that came out of my first

year in graduate school. And of course thanks for all those crazy awards you gave me at the GEARS banquets...most expensive experiment described...loved it!

I also want to acknowledge my friend and soon-to-be roomie Darren Forman for always stimulating conversations and for employment in the final hour. It's been fun working with you this spring, trying something new. Gratitude also goes out to Prof. Bob McLeod for taking a risk on this chemist/engineer.

I'd like to thank my two best girlfriends Nichja Dryg and Lydia Novotny: you have both been great friends over the years. Nichja - I've known you for so many years and I will continue to be inspired by your persuasive talents. I have a feeling I will be taking notes on your confident communication skills throughout my career. Lydia - my athletic partner in crime - I do need to specifically thank you for introducing me to CrossFit; the sport has revived my energy level and helped keep me sane when experimental frustrations took hold.

Big thanks go out to my wonderful hubby Adam for his continued support over the years, from the first year struggles and dilemmas to the end of this grad school journey. Thanks for always listening to all my practice talks and providing me thoughtful comments. Having you by my side throughout has made it all worthwhile.

And finally I must thank my parents for their continuous support. I know you don't quite understand what it is I've been doing here...yes it is considered 'school' but it really is just a job after the first couple years. I appreciate that you've taken the time to come visit so often since I've moved away...I never really feel like you're very far away, and that's nice...you really are just a phone call or a quick plane ride away. Love you both so much.

Contents

Chapter

Tables

Table

xiv

Figures

Figure

Chapter 1

Introduction

1.1   The Importance of Renewable Fuels

Meeting our society's increased demands for transportation accounts for a large portion of world energy consumption. According to the Energy Information Agency, the U.S. alone consumed just over 6.7 billion barrels of petroleum in 2012, accounting for about 21% of world consumption [134]. High energy-density batteries or hydrogen fuel cells may still be the way of the future for transportation, but hydrocarbon-based fuels will remain important in the short term. However, limited fossil resources and climate impacts due to carbon dioxide emissions have made it critical that we find ways to produce and use renewable, carbon-neutral fuels.

Biomass is abundant and has the potential to be a renewable source of energy, but is primarily in the form of non-volatile carbohydrates and thus conversion to remove excess oxygen is necessary. The first generation of biofuels converted sugars and starch to ethanol; however, ethanol as a stand-alone transportation fuel is not ideal because its energy density is only 70% that of gasoline [109] and with blends greater than $10-15\%$ it is corrosive in most standard combustion engines. In addition, due to its polar molecular structure ethanol is hygroscopic and forms an azeotrope with water, thus requiring an energy intensive distillation process to remove dissolved water. Finally, fuels derived from sugar and starch are disruptive to the food chain and are not sustainable with an ever-growing world population. Recent developments in the conversion of lignocellulosic biomass have sparked a renewed interest in

biofuels, with the goal to produce valuable fuels derived from the inedible portion of plants, such as less valuable crop waste or dedicated crops not part of the food system [130].

1.2   Composition of Biomass

In order to utilize the energy stored in the carbon-hydrogen bonds of biomass it is important to understand the chemical structure of the plant itself. Biomass primarily consists of three biopolymers: cellulose and hemicellulose, both polysaccharides, and lignin.

Cellulose is the most abundant organic compound on the planet [100], making its use very desirable. This biopolymer is formed entirely of glucose monomers, linked together by β-1,4 glycosidic linkages as shown in Fig. 1.1. The individual strands of cellulose arrange themselves into bundles, with a high-degree of hydrogen bonding between the individual strands [44], providing structural support to the plant cell walls and creating a rigid structure that is difficult to depolymerize.
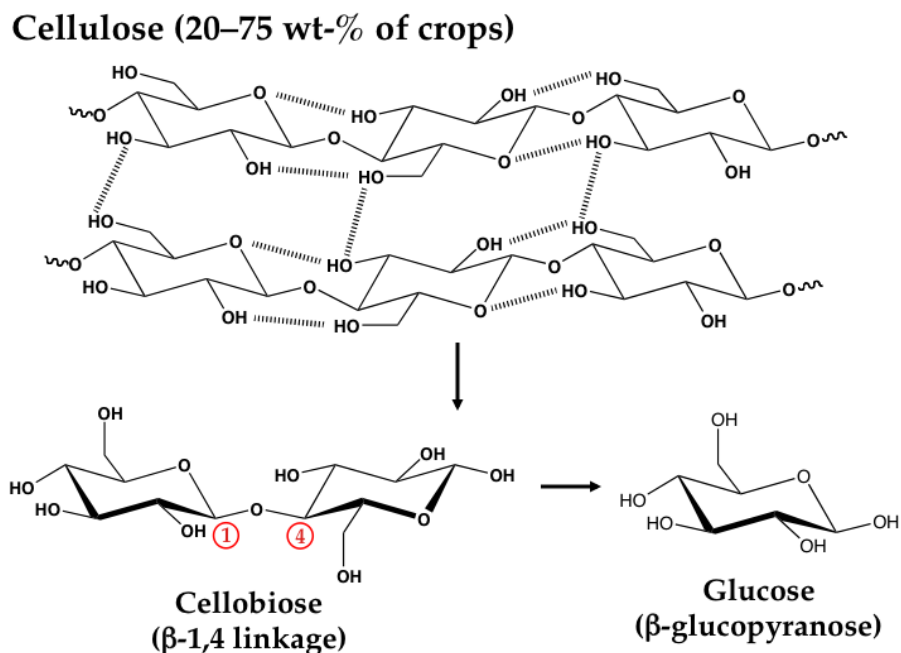
Figure 1.1: Cellulose is a long (10,000+ monomer units), linear biopolymer of glucose with a high-degree of hydrogen bonding between the linear strands.

Hemicellulose is also a polysaccharide, accounting for an average of $20-50\%$ of the plant mass [21]. In contrast to the linear, homogeneous nature of cellulose, hemicellulose contains long, heterogeneous branched chains of both five-carbon sugars, such as xylose [74], and six-carbon sugars. Strands of hemicellulose are interwoven into the cell wall, forming a "hairy coat" around the cellulose bundles [44], adding flexibility while simultaneously increasing the strength of the cell wall. The third major component of lignocellulosic material is lignin, a complex biopolymer of phenolic ethers that forms a protective, rigid layer within the cell wall creating a resistance to enzymatic attack.

Together these three biopolymers are referred to as lignocellulosic biomass and include crop waste materials such corn stover and sawdust or specifically dedicated crops such as switchgrass [21]. Converting lignocellulosic material to high-valued end-products allows dedicated non-food crops to be cultivated on marginal land and can also enable the use of local agricultural resources. However, to utilize a variety of feedstocks also requires that the conversion methods are flexible, because every plant species has a different composition of these three biopolymers.

1.3   Conversion of Lignocellulosic Biomass

In recent years there have been numerous studies documenting the challenges of converting these low-value waste materials to potential valuable fuels and platform chemicals [44, 52, 70, 86]. Three common techniques for converting lignocellulosic biomass to useful end-products include thermochemical, biochemical and non-enzymatic chemical conversion.

1.3.1   Thermochemical and Biochemical Conversion

Two common methods for upgrading lignocellulosic biomass to fuels or platform chemicals are thermochemical and biochemical processing. Thermochemical processing involves gasification, pyrolysis or combustion of the whole feedstock. In order to make liquid fuels the raw material is mechanically processed and is introduced into a reactor of varying oxygen

concentration where it undergoes pyrolysis (no oxygen) or gasification (some oxygen) to make intermediates which can then be reformed into desirable end-products. If implemented on a large scale, thermochemical processing has the potential to be one of the most time-efficient conversion processes [88], however it requires large capital and transportation costs to handle the quantities of feedstock needed for operations.

Another technique for converting lignocellulosic biomass to valuable fuels is biochemical processing, which converts the feedstock directly into sugars (saccharification) followed by either fermentation to make alcohols (ethanol, butanol) or chemical conversion schemes with catalysts to make a number of potential fuel molecules. Biochemical conversion schemes are considered suitable for operations on a smaller scale compared to thermochemical processing [44], reducing transportation and capital costs; in addition such facilities can be designed around regional feedstocks and local economies.

1.3.2   Non-Enzymatic Chemical Conversion

The first generation of biofuels in the United States were produced by biochemical conversion techniques, first using acids to catalyze the hydrolysis of starches found in corn, followed by fermentation of the released sugars to ethanol. This process, though extremely well understood and optimized, is time-consuming (on the order of hours to days) and requires an energy intensive distillation to separate trace amounts of water from the desired fuel. Enzymatic pathways to convert lignocellulosic biomass to bio-ethanol are also available [103], but the scalability and selectivity of the necessary enzymes is daunting. Ethanol as a stand-alone transportation fuel is also not ideal, as discussed in Section 1.1. It is desirable that any new fuels have physical properties that allow them to be efficiently distributed and stored utilizing the existing infrastructure and also burned in existing engines; thus any potential biofuel should ideally offer similar properties to gasoline or diesel.

There are hundreds of different molecules that can be synthesized from lignocellulosic biomass and potentially used as fuels; two such classes of molecules are furanic [13, 48, 71]

and lactonic [3, 55, 70] based fuels and chemicals, including but not limited to alkylated furans, furanic ethers and lactones, examples of which are shown in Fig. 1.2.
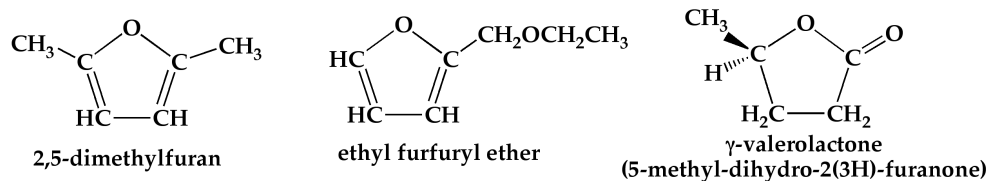
Figure 1.2: Examples of potential furanic and lactonic biofuels: alkylated furans (2,5-dimethylfuran), furanic ethers (ethyl furfuryl ether), and lactones (γ-valerolactone)

In the past several years these potentially useful molecules have been efficiently synthesized from biomass-derived carbohydrates such as fructose [106]. More recently pathways to non-enzymatically convert untreated lignocellulosic material has been demonstrated [12, 13]. As an example, the work of Binder and Raines [13] have demonstrated a process that converts the cellulose in untreated lignocellulosic biomass to 2,5-dimethylfuran (DMF) with 9% efficiency (based on an estimate of the cellulose content of the starting material) as shown in Fig. 1.3. They use ionic liquids to assist in the fast initial breakdown, or "decrystalization" of the biomass [14], eliminating the use of other time-consuming pretreatment processes. The ionic liquids also act as solvents in mild ($< 250°C$), yet fast hydrolysis of the glycosidic bonds in the polymers of cellulose and hemicellulose [115] to obtain the desirable sugar precursors. Catalysts then convert these sugars to the platform chemical 5-hydroxymethylfurfural (HMF), a hexose (six-carbon) dehydration product that is a gateway molecule to other useful industrial chemicals and potential fuels. Hydrogenolysis of HMF over a Cu catalyst removes two more oxygen atoms from the ring, yielding DMF. In contrast to the fermentation of sugars to ethanol, where for every molecule of glucose (6 carbon atoms) only two-thirds of those carbon atoms are actually converted into potential useful energy ($C_6H_{12}O_6 \rightarrow 2\ CH_3CH_2OH + 2\ CO_2$) and the remainder lost to CO_2, in the production of DMF all of the carbon atoms in the original starting material are retained.

Analogous to the conversion of cellulose to HMF, is the conversion of the pentoses in
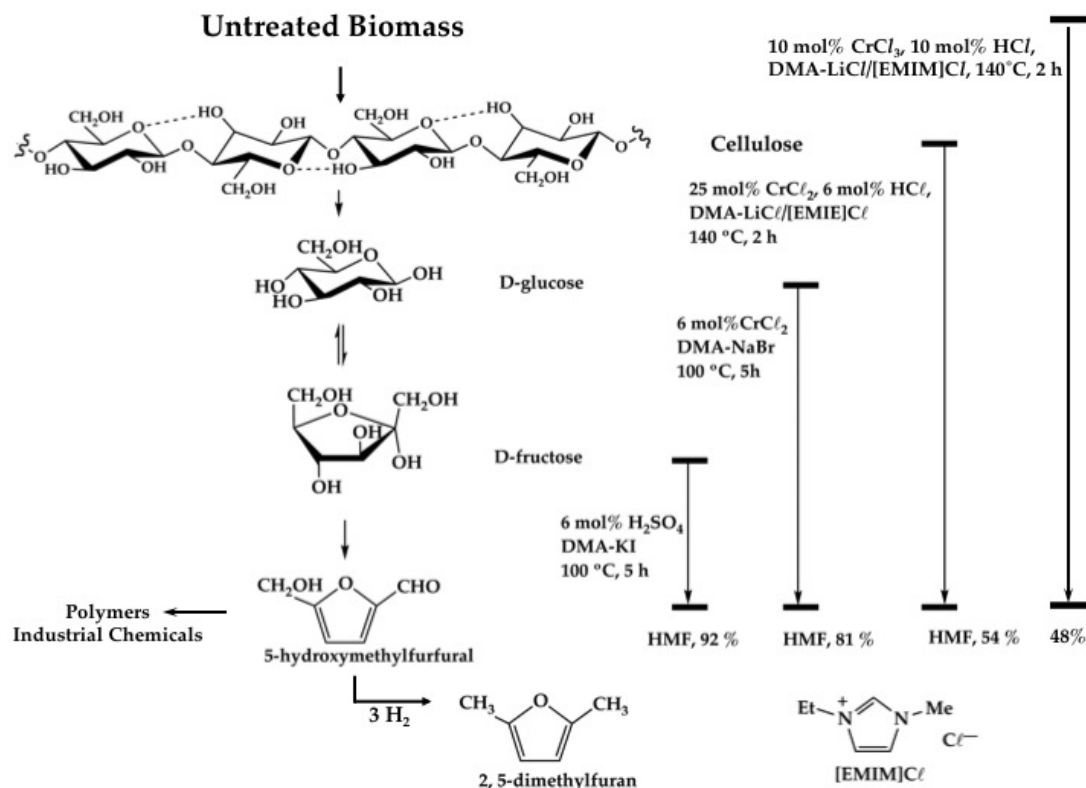
Figure 1.3: A demonstrated non-enzymatic chemical conversion scheme of untreated lignocellulosic biomass to 2,5-dimethylfuran, a potential biofuel (adapted from [13])

hemicellulose to furfural. Similar to HMF, furfural is also considered a platform chemical because it is an important intermediate for synthesizing other useful chemicals and fuels [11]. Converting hemicellulose to furfural is not a new processes, as furfural has been a common industrial chemical derived from lignocellulosic biomass for decades. It was first discovered at the Quaker Oats Company [22] where they produced it by acid-hydrolysis and dehydration of xylan, a polymer of xylose, found in the hemicellulose of the feedstock. The process to achieve high yields of furfural from xylose and hemicellulose has been optimized in recent recent years through use of solid-acid catalysts [37, 50, 151]. Additional processing of furfural can yield 2-methylfuran through direct hydrogenation [151] or other furfural-based oligomers can be synthesized to high-quality high-molecular weight diesel fuels [74]. The biofuel platform to produce furanic ethers first hydrogenates furfural to furfuryl alcohol [71],

followed by conversion to the ethers in the presence of solid acid catalysts and low molecular weight alcohols (methanol or ethanol), as shown in Fig. 1.4. Conversion schemes to lactones proceed through the platform chemical levulinic acid (CH_3-CO-CH_2CH_2-COOH) instead of furfural [42].
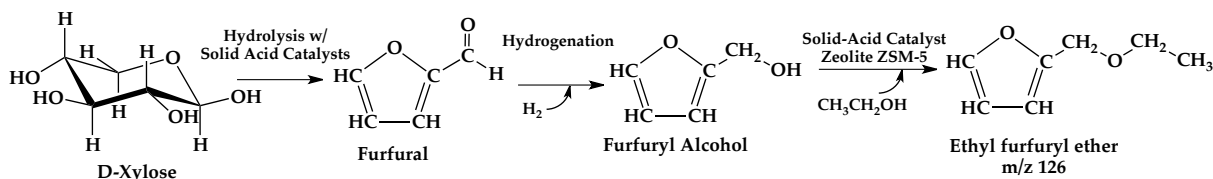
Figure 1.4: A chemical conversion scheme of the xylose found in hemicellulose to furfural, upgraded to potential furanic fuels such as ethyl furfuryl ether.

1.4   Beyond Bioethanol

It is likely the fuel of the future will not necessarily be a single molecular component, but rather will include a blend of any number of molecules. Which blends can be produced quickly and cost effectively has yet to be determined. There are numerous factors to consider when attempting to create renewable and cost-competitive bio-based fuels, one such consideration is the energy content of the fuel relative to its cost. As a first generation biofuel the lower heating value (LHV) of ethanol is 70% that of gasoline ($LHV_{EtOH} = 21.3$ MJ L^{-1}, $LHV_{gas} = 31.9$ MJ L^{-1}) [139], therefore more fuel volume is required per mile traveled. On the other hand the energy content of some proposed substituted furans more closely match that of gasoline ($LHV_{DMF} = 29.3$ MJ L^{-1}, $LHV_{EFE} \approx 28.3$ MJ L^{-1} [33]). These oxygenated fuels also have low solubility in water, possess a high research octane number [26] and have a similar laminar burning velocity to that of gasoline [147], all factors which are compatible with existing infrastructure and engines.

On the production side, one must also consider the cost and CO_2 intensity of producing the fuel in addition to any potential environmental consequences associated with producing or distributing the fuels. As an example, Lange *et al.* [71] discuss the footprint of upgrading

furfural to several potential fuels, including furanic ethers. Their findings show that the CO_2 intensity of producing ethyl furfuryl ether (EFE) from furfural is a factor of 2 to 4 lower than that of other fuel upgrades under present consideration, in part due to the fact that fewer hydrogenation steps with H_2 are required. In order to be a truly renewable fuel and address impacts of climate change, the CO_2 emissions from soil to tailpipe must be neutral.

Finally, if these molecules are to be burned in our vehicle engines, it is important to understand both the pyrolytic and combustion behavior of the potential fuels [66, 120]. The combustion processes of these complex, oxygen-containing species is of current interest [147, 148] and only recently have some of them been subjected to engine studies [33, 139, 146]. To date there have been several experimental and theoretical gas-phase pyrolytic studies of the alkylated furans, 2-methylfuran and 2,5-dimethylfuran, [78, 79, 118, 121] however, very few studies have been performed on the furanic ethers or lactones shown in Figure 1.2. It is important to have a complete understanding of the elementary reaction steps of these potential fuels and to identify important reaction intermediates. Understanding these initial processes can help elucidate possible chemical mechanisms for emission formation.

1.5   Experimental Motivations and Thesis Outline

In order to establish a complete molecular picture of the first thermal products formed from the pyrolysis and oxidation of furanic and lactonic biofuels, a microtubular flow reactor was used to thermally decompose furan, 2-methoxyfuran and the select lactones shown in Fig. 1.5. The experimental methods allow the identification of the initiation reactions that can produce radicals and other reactive intermediates. As most initiation rates need to be calculated because they are too difficult to measure, the experimental results presented in this thesis demonstrate progress towards validating these types of calculations, aiding in the development of accurate initiation chemistry for reaction mechanisms.

Chapter 2 describes the microreactors used for these studies and the complementary diagnostic techniques photoionization mass spectrometry and matrix isolation infrared spec-
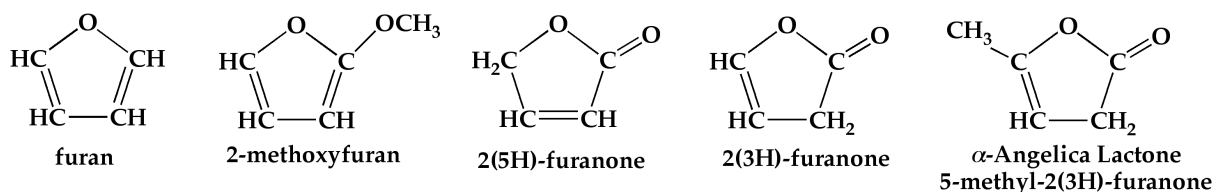
Figure 1.5: The furans and lactones pyrolyzed in a microreactor

troscopy. Chapter 3 describes the nature of the pyrolysis of furan, the first molecule in Fig. 1.5 and the parent compound of the furanic fuels. In addition to spectroscopic detection of the pyrolysis species, this study also includes quantification of the two primary product channels and quantifies the radical product channel. Chapter 4 documents the pyrolysis of the smallest furanic ether, 2-methoxyfuran, along with identification and quantification of an allylic lactone, 2-furanyloxy radical. Chapter 5 delves more deeply into some of the lactones that were also shown to be relevant to the decomposition of 2-methoxyfuran. Included for reference in Appendix A is the calibration procedure for quantitative analysis of the chemical reactions in the continuous flow microreactor, including mass discrimination factors and an experimental determination of the chemical temperature in the reactor. Appendix B includes a procedure for quantifying uncertainty in the experimental measurements and presents the supplementary results for the furan measurement uncertainties. Finally, Appendix C is an extra resource for the methoxyfuran and lactone experimental results, including assigned vibrational frequencies and additional spectra.

Chapter 2

Experimental Methods

A molecular picture of the first thermal products formed from the pyrolysis of furanic biofuels is investigated by thermally decomposing furan, 2-methoxyfuran, and select lactones in a microtubular (μtubular) flow reactor, as described in Chapter 1.5. The microreactor is an adapted version of Peter Chen's hyperthermal nozzle [65], which was originally designed as a source to produce radicals and other reactive intermediates [59, 105, 158]. In recent years the Chen nozzle has been modified to study the thermal decomposition mechanisms of molecules relevant to biomass pyrolysis [58, 111–113, 136–138] and those proposed as potential biofuels [62]. The microreactor offers a short residence time (approximately 50-200 μs) coupled with sensitive diagnostics. The short residence time eliminates most, if not all, bimolecular chemistry, allowing for the identification of isolated unimolecular reaction schemes, and is short enough to detect radicals and other reactive intermediates. Upon exiting the reactor the molecules expand supersonically into a high-vacuum which rapidly cools the temperature in the molecular beam, quenching further reactions. The products, including radicals and metastables, are identified with two complementary diagnostic techniques: photoionization time-of-flight mass spectrometry to determine the mass of the species and matrix isolation infrared spectroscopy to determine the molecular structure. This chapter describes the reactors, diagnostic techniques, and analytical procedures used to identify and quantify the pyrolysis products.

2.1   Microtubular Reactor

The microreactor is a unique type of flow reactor; if operated under dilute conditions it can isolate unimolecular reaction schemes and allows one to examine thermal products formed at the earliest time scales (approximately 100 μs). However, from a fluid dynamics and heat transfer perspective, the experiments conducted in the μtubular reactor also come in three distinct forms: pulsed flow in helium or argon and continuous flow in helium. The experiments performed with a pulsed flow include fixed-frequency photoionization time-of-flight mass spectrometry (PIMS) using He carrier gas and matrix isolation Fourier transform infrared (FT-IR) spectroscopy with Ar carrier gas. Another set of PIMS experiments are performed at Lawrence Berkeley National Laboratory's Chemical Dynamics Beamline (9.0.2) at the Advanced Light Source (ALS) with a reactor operated with a continuous flow of helium.

2.1.1   Pulsed Reactors

One version of the pulsed flow reactor assembly is shown in Fig. 2.1. The reactor consists of a resistively heated silicon carbide (SiC) tube (2.5 to 3.8 cm in length, 1 mm i.d., 2 mm o.d.). The reactor is heated using fitted carbon disks attached to molybdenum clips, passing up to 5 A through the reactor to heat to 1600 K. The heated length is about half to two-thirds the length of the reactor with the temperature of the outer wall monitored by a tungsten/rhenium Type C thermocouple (Omega, wire pairs W/5% Re and W/26% Re, diameter 0.005 in). Upstream of the reactor is a pulsed valve (Parker General Valve, series 9, 0.25 mm orifice). The valve is controlled with an Iota One pulsed valve controller (open time of the valve is on the order of hundreds of μs [158]), set to operate at 10 Hz for pulsed He and 20 Hz for pulsed Ar experiments. The temperature of the pulsed valve is monitored with a Type-K thermocouple (Omega, chromel-alumel, 0.01 in diameter) and can also be controlled (Love Controls, series 16A) with a flexible heater (0.75 in by 2 in, Minco). A 1 cm i.d. alumina cylinder surrounds the SiC reactor to reduce radiative heat losses.
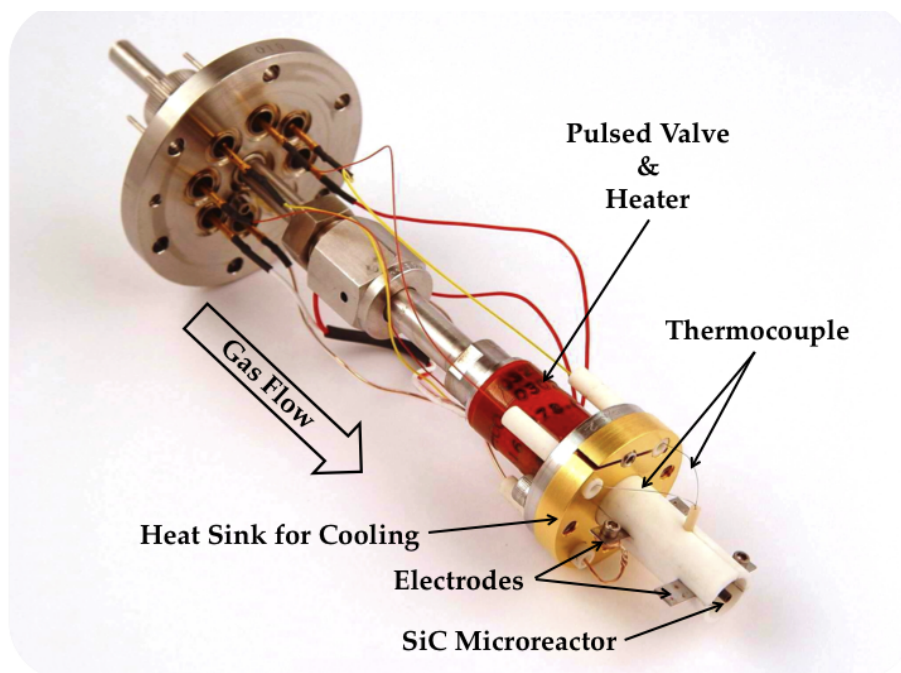
Figure 2.1: Inner pyrolyzer assembly with pulsed valve

The reactant mixtures for the pulsed experiments range from $0.03\%-0.1\%$ in He or Ar carrier gas. Liquid precursors with adequate vapor pressure to prepare gaseous mixtures are degassed using a freeze-pump-thaw cycle and used without purification from the manufacturer, unless otherwise indicated. The total backing pressure to the pulsed valve is about 1500 Torr He for PIMS experiments and 800 Torr Ar for IR experiments. The pressure at the reactor exit for both experiments is maintained at approximately $1-10$ μTorr. Reactants with vapor pressures less than about 1 Torr at 300 K are placed in a small quartz sample tube (1.5 mm i.d., 15 mm long) and are gently heated to at most 60°C with a sample probe placed directly behind the pulsed valve in order to entrain the vapor in a stream of helium or argon before entering the reactor. The reactant concentrations for these experiments are more uncertain due to lack of accurate vapor pressure measurements for many of these molecular species.

The flow at the reactor exit chokes (reaches the local sonic velocity) and undergoes a supersonic expansion. It is estimated that the free-jet expansion rapidly cools the molecules in the beam to about 40 K (rotationally) [158] within a tube diameter, eliminating any

additional reactions. The degree of vibrational cooling in the molecular beam is unknown at this time and can affect interpretation of the photoionization experiments.

2.1.2 Continuous Flow Reactor

2.1.2.1 Experimental

The continuous flow microreactor, illustrated in Fig. 2.2, is a SiC tube (0.66 mm i.d, 2 mm o.d., 2.5 cm long), mounted to a standard stainless steel Swagelok fitting (1/8" to 3/8" reducing union) and secured with a graphite ferrule (Restek, 1/8" tube, inner diameter drilled out to fit reactor).
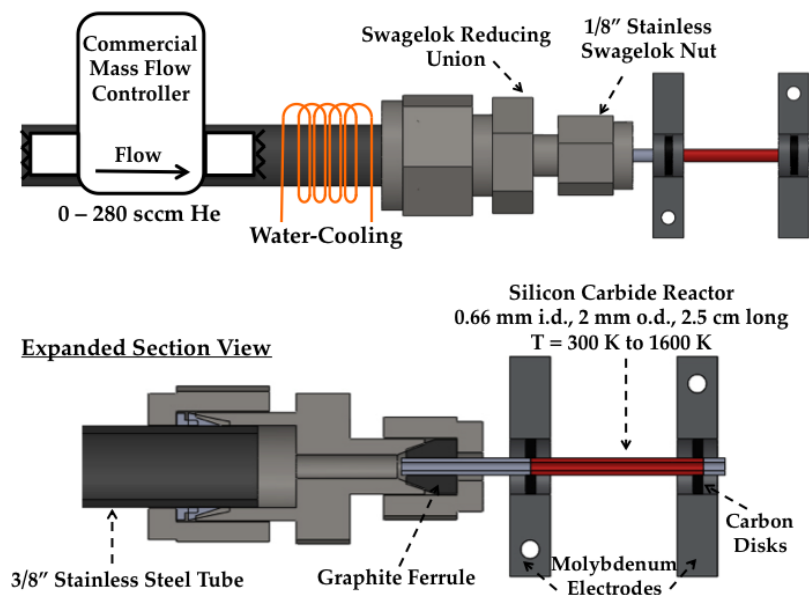
Figure 2.2: Schematic of the continuous flow reactor for experiments performed at the Advanced Light Source

Approximately 1.5 cm of the SiC is resistively heated and the temperature of the outer wall of the SiC reactor is measured with a Type-C or Type-K thermocouple and also monitored with an infrared thermometer (Omega iR2P temperature controller, range $600°C-1600°C$). Dilute gaseous reactant mixtures are prepared in stainless steel cylinders with concentrations between $0.0025\%-0.15\%$ reactant in helium (final tank pressure between

2000−5000 Torr). Less volatile reactants are heated to at most 60°C with a sample probe to entrain the vapor in a stream of helium before entering the reactor. The mass flow rate is held constant at 280 sccm He with a commercial mass flow controller (MKS P4B 0-200 sccm N_2). The pressure upstream of the reactor is monitored with a MKS Baratron capacitance manometer and increases approximately linearly with the operating temperature. At room temperature the upstream pressure is about 100 Torr and with a reactor temperature of 1600 K the upstream pressure is about 290 Torr; the pressure at the reactor exit is measured with a Micro-Ion gauge (Granville-Phillips) and remains constant at about 10 μTorr.

2.1.2.2   Reactor Modeling

To understand the chemical reactions in these microreactors requires that the flow field within the reactor be understood. However, since the reactor is very small (a few centimeters in length and 0.6−1 mm in inner diameter) it is not possible to either insert sampling probes or readily gain optical access, as would be the case for a larger scale reactor or shock tube. While the reactor is a large aspect ratio straight tube of constant diameter, the flow within it cannot be described as simple Poiseuille flow. The tube is resistively heated to high temperatures using attached electrodes and through simulation [49] and experimental observation it was shown that the portion of the tube that is outside the span of the electrodes is at a lower temperature due to convective and radiative cooling. Therefore there is a strong axial gradient in the wall temperature, usually starting at the inlet, and this complicates the flow field. The heating also accelerates the flow, and if the mass flow rate is high enough the local Mach number will increase rapidly and the flow will choke near the exit. It was also found computationally [49] that because the chamber pressure downstream of the tube exit is so low it is possible for the local Knudsen number within the tube to increase to the point where the continuum Navier-Stokes equations no longer exactly apply. When this occurs, one must account for "slip" both in momentum and thermal energy at the walls, as this affects the radial profiles of velocity and temperature. Taking the above into account, it
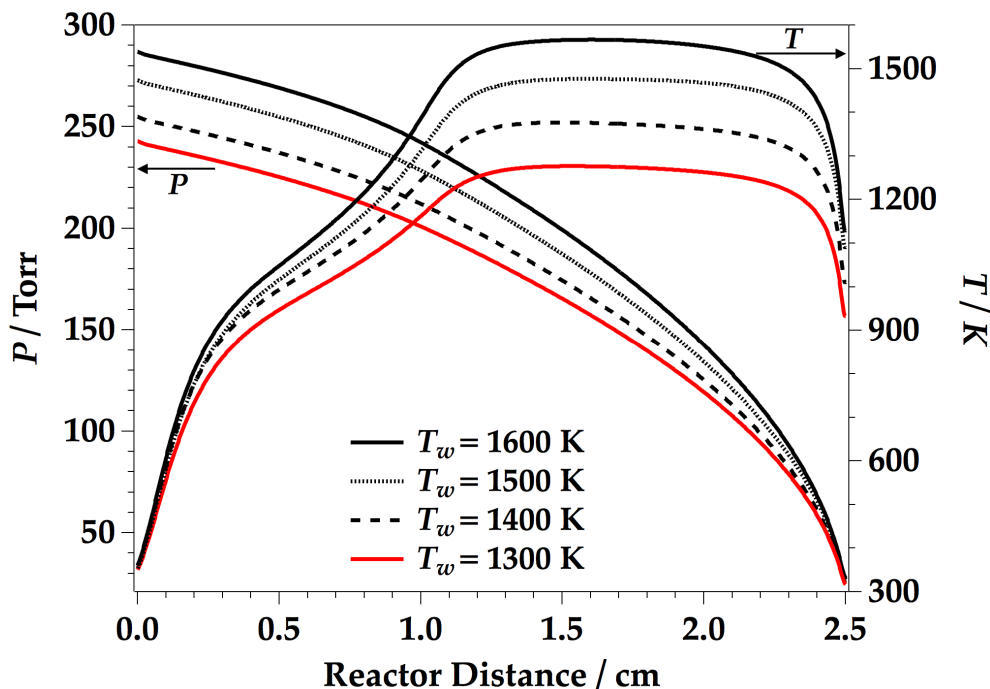
Figure 2.3: Simulated centerline pressure (left) and temperature (right) profiles for a 280 sccm continuous flow of helium along the length of a 2.5 cm reactor (0.66 mm i.d.) as a function of wall temperature (T_w) [49]. The electrodes for resistive heating are placed at 1 cm and 2.4 cm.

was found that accounting for slip permits simulation of the flow using computational fluid dynamics (CFD) such that the measured pressure boundary conditions and mass flow rate can consistently be reconciled, lending considerable confidence that the simulations [49] are accurate.

The CFD simulations predict that the pressure profile inside the reactor rapidly decreases along the length of the reactor as shown in Fig. 2.3. The contributor to this decrease in pressure is an accelerating flow, as shown in Fig. 2.4. The simulations also show that the temperature of the gas along the centerline of the reactor is relatively constant between the electrodes (placed at 1 cm and 2.4 cm along the reactor). Most recent reactive CFD simulations [49] indicate that most of the interesting chemistry occurs between 0.5 to 2 cm of the reactor length, where both the temperature and pressure are elevated. The reaction rates
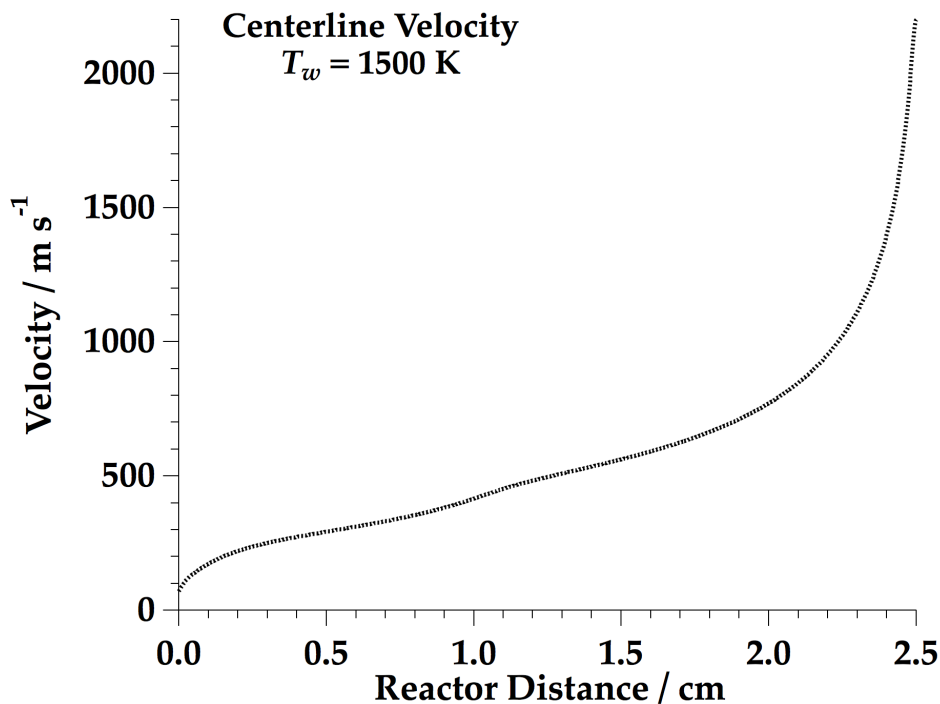
Figure 2.4: Simulated centerline velocity profile for a 280 sccm continuous flow of He along the length of a 2.5 cm reactor (0.66 mm i.d.) at $T_w = 1500$ K [49]. The electrodes for resistive heating are placed at 1 cm and 2.4 cm.

rapidly fall off when approaching the reactor exit (in the last 0.5 cm), due to the reduced pressure.

Another important operating factor to consider is the residence time in the heated portion of the reactor. The longer the residence time, the more possibilities there are for radical-radical reactions and radical addition or abstraction reactions with the precursors under investigation. These types of reactions greatly complicate the analysis of the desired unimolecular processes. One way to assess the possibility of bimolecular reactions is based on collisions. Considering the single particle collisional frequency, z_{ii}:

$$z_{ii} = \frac{N_i}{V}\sigma\sqrt{2}\left(\frac{8kT}{\pi m_i}\right)^{1/2} = \frac{P}{kT}\sigma\sqrt{2}\left(\frac{8kT}{\pi m_i}\right)^{1/2} \quad \text{(collisions s}^{-1}\text{)} \quad (2.1)$$

with an intermediate temperature (T) and pressure (P) of 1200 K and 200 Torr assumed (see Fig. 2.3), the collisional frequency in the reactor (z_{ii}) is on the order of 100 collisions

μs^{-1} (assuming a collisional cross-section (σ) of 0.4 nm^2 and a molecular weight (m_i) of 40 amu, values between He and CO$_2$; k is the Boltzmann constant with a value of 1.38(10^{-23}) J K^{-1}). Incorporating a dilution of 0.01% (a partial pressure of 0.02 Torr) and a fixed residence time of 100 μs, a rough estimate of the collisions between potentially reactive species is on the order of 10 collisions. Reactions that occur at the gas kinetic rate could be influential at these conditions, but most rates will be at least an order of magnitude lower and therefore won't be significant compared to the unimolecular reaction scheme of interest. Decreasing the residence time in the reactor is not a viable way to avoid bimolecular reactions because it is essentially a fixed experimental parameter due to limited pumping capabilities, so instead this task is accomplished through dilution.

A discussion of the use of chemical thermometers coupled with CFD to simulate the fluid dynamics in the continuous flow microreactor is also included in Appendix A. These early experimental results, performed in a longer SiC reactor and at a reduced mass flow rate of 25 sccm He, indicate that the external wall temperature measurements for these experiments are about 150 K higher than an effective "chemical temperature" in the reactor. However, more recent CFD simulations of 280 sccm He flow suggest that the temperature difference between the wall and the internal gases may be closer to 25−50 K [49]. Ongoing characterizations of the thermodynamic conditions within and outside the reactor using both computational fluid dynamics (CFD) and spectroscopic techniques are underway.

At this time only the continuous flow reactor has been characterized by CFD. The transient nature of the pulsed experiments, while excellent for gaining qualitative information of the products, is very complicated to model.

2.2   Diagnostics

Molecules exiting the μtubular reactor are probed with two different diagnostic techniques: photoionization time-of-flight mass spectrometry or matrix isolation FT-IR absorption spectroscopy. In Boulder the masses of the thermal cracking products are identified by fixed-

frequency vacuum ultraviolet photons of the 9th harmonic of an Nd:YAG laser. A second set of experiments performed at the Advanced Light Source (ALS) in Berkeley, CA utilize tunable VUV synchrotron radiation to identify products emerging from the microreactor.

2.2.1   Photoionization Time-of-Flight Mass Spectrometry (PIMS)

A schematic of the reactor combined with the photoionization mass spectrometer in Boulder is shown in Fig. 2.5. This technique is considered "soft" ionization because it ionizes a molecule close to its ionization threshold, reducing or even eliminating the severe fragmentation of ions observed with electron impact ionization [4, 20].
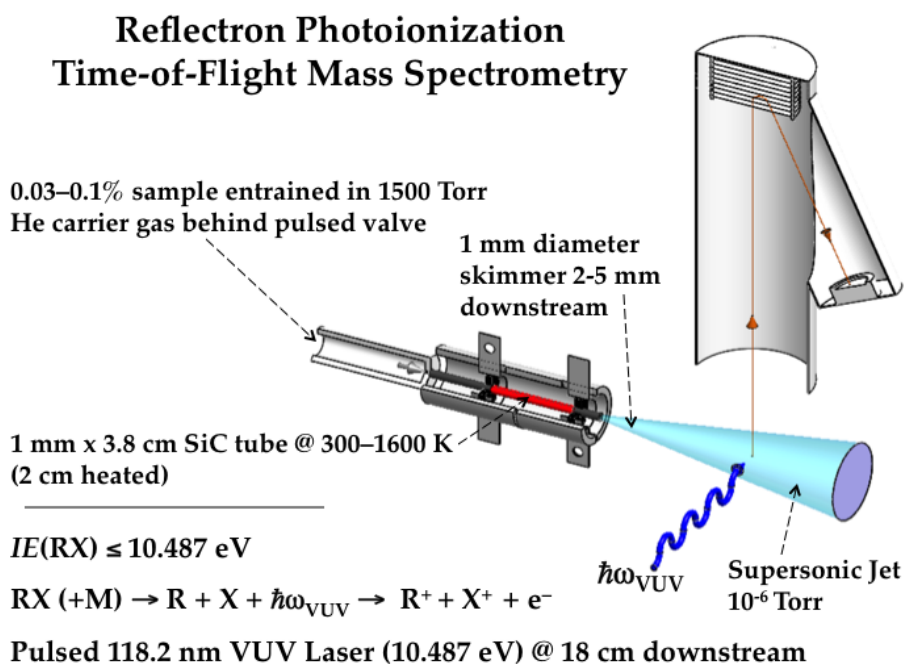
Figure 2.5: Reflectron photoionization time-of-flight mass spectrometer in Boulder with fixed frequency photons at 118.2 nm.

A Spectra Physics Quanta-Ray Pro 10 Hz pulsed neodymium-doped yttrium aluminum garnet (Nd:YAG) laser (fundamental wavelength 1064 nm) is tripled twice to generate vacuum ultraviolet (VUV) photons at 118.2 nm (10.487 eV), the 9th harmonic of the Nd:YAG. The 118.2 nm light is generated by first tripling the 1064 nm fundamental to 355 nm in a harmonic

generator with KD*P (potassium dideuterium phosphate) crystals. The 355 nm light is then focused into a xenon:argon gas cell with a fused silica lens, where a small fraction of the incoming light is tripled again to 118.2 nm (estimated at 10 μJ per pulse at 10 Hz [158]). The tripling cell is 30 cm long and has a total cell pressure of about 130 Torr (Xe:Ar ratio 1:10 [68, 69]). A schematic of the laser alignment and time-of-flight operations is shown in Fig. 2.6.

Generating Vacuum Ultraviolet (118.2 nm)
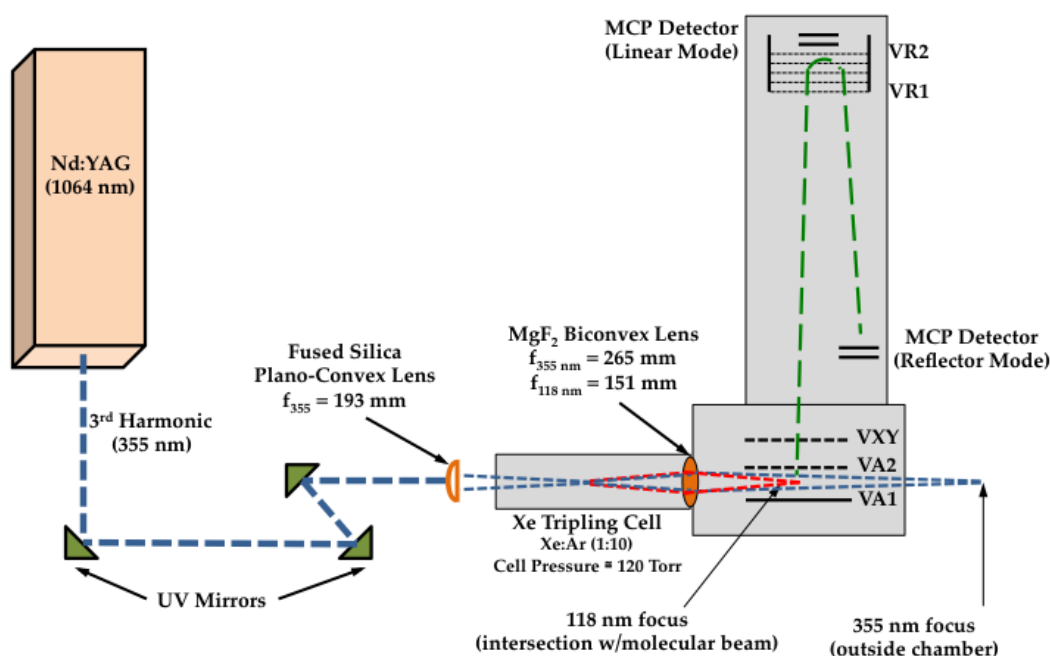
Figure 2.6: Generation of 118.2 nm photons (10.487 eV) and ion flight path in the reflectron time-of-flight mass spectrometer

Molecules in the molecular beam with ionization thresholds less than 10.487 eV are ionized and separated for detection in a 100 cm Jordan (Jordan TOF Products, Inc.) reflectron time-of-flight mass spectrometer. The ions are accelerated from the source region by a repeller plate behind the packet of ionized molecules (VA1 = 1597 V) and then drawn through an extraction grid (VA2 = 953 V). Ion optics (VXY = 38 V) guide the ion packet into a field-free region of the flight tube where separation occurs based on the mass-to-charge ratio (m/z).

The ions are reflected at the opposite end of the flight tube, reversing their direction of travel (VR1 = 1058 V, VR2 = 1748 V). Assuming all ions created by the 118.2 nm light have a charge of +1, the lighter molecules will travel faster than the heavier molecules and reach the detector first. Ions are detected with a microchannel plate (MCP) detector (dual plate, chevron-type, VD = -1850 to -1900 V), creating an avalanche of electrons. For every ion that hits the detector approximately 10^6 electrons are ejected from the plates, thus amplifying the signal [145]. The MCP signal for the fixed-frequency experiments in Boulder is reported as an analog voltage.

The mass resolution in the spectrometer is limited by the temporal width of the ion packet (which is determined by the pulse width of the ionization source) and the velocity distribution of the ions, determined by where they were formed spatially with respect to the extractor plates (VA1, VA2). The reflectron-type separation of the ions reduces the kinetic energy distribution of an individual mass within the ion packet, thus improving the resolution of the spectrometer. The mass resolution (m/Δm) in the Jordan reflectron in Boulder is about 800 amu.

A second set of PIMS experiments use tunable synchrotron radiation at the Advanced Light Source (ALS) to ionize the products emerging from the microreactor. A portion of the flow exiting the reactor passes through a 2 mm skimmer approximately 1 cm from the reactor exit and enters the ionization region, where the molecular beam is interrogated by synchrotron radiation about 12 cm downstream. The Chemical Dynamics Beamline (9.0.2) at the ALS produces tunable VUV radiation (7.3 eV$-$30 eV) at a rate of 500 MHz tuned by a Czerny-Turner grating monochromator. The sampling rate of mass spectra is limited only by the gating electronics on the spectrometer, set to 10$-$17 kHz, depending on the desired mass sampling range. The optimum pulse sequence of the ion optics is determined daily, with a typical voltage sequence of: VD = -4000 V, VA1 = 1200 V, VA2 = 1193 V, VXY = 71 V, focus = 0.4, pulser = 0.25 kW (4.7 mA), VR1 = 1057 V, VR2 = 2010 V. The ions are detected by a microchannel plate and the signal recorded as ion counts. A similar 100

cm Jordan reflectron time-of-flight spectrometer is used at the ALS and it also has a mass resolution of about 800 amu.

Photoionization efficiency (PIE) curves for a given mass-to-charge ratio (m/z) are obtained by plotting the summation of the ion signal versus the selected photon energy range, normalized by the photon flux measured by a photodiode with a calibrated energy dependent efficiency. These curves serve as an additional identification tool beyond the mass of the molecular species.

2.2.2 Matrix Isolation Infrared Spectroscopy

As a complement to the PIMS, infrared spectroscopy in an argon matrix provides structural information for the pyrolysis products, differentiating thermal products of identical mass. The molecular beam formed at the reactor exit impinges on a cold window. The products, now trapped in frozen argon, are detected by FT-IR spectroscopy, as shown in Fig. 2.7.
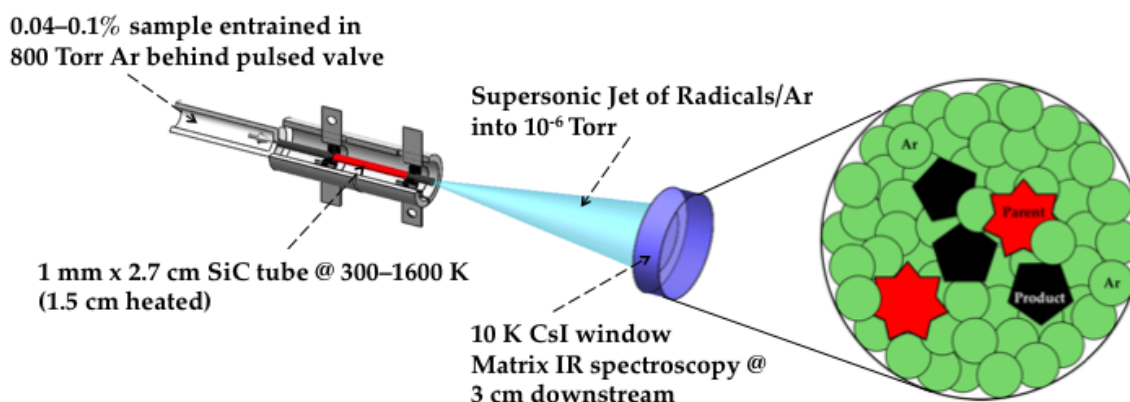
Figure 2.7: Pyrolysis products entrained in Ar exit the μtubular reactor and become trapped on a cryogenic window.

A 100 mm i.d. diffusion pump (Edwards Vacuum Systems), backed by a mechanical pump (Edwards Vacuum Systems), produces the high-vacuum conditions (10^{-6} Torr) necessary for matrix isolation spectroscopy. The flow reactor assembly is mounted to the vacuum shroud

of a two-stage closed-cycle helium cryostat (APD Cryogenics, model DE-202, 60 Hz and 2.5 W cooling capacity at 20 K; compressor model HC-2D) which cools an infrared transparent cesium iodide (CsI) window to 10 K. Figure 2.8 shows a detailed cross-sectional view of the matrix assembly and the positions for deposition and collection of the FT-IR spectrum. The CsI window is mounted in a metallic holder, which is screwed into the cold finger of the He-cryostat expansion unit. Thermal contact between the finger and the window holder is enhanced by a thin layer of indium. Molecules exiting the reactor are aimed at the cold, IR transparent window (approximately 3 cm away), and a matrix is formed by the deposition of many thin layers of the pulsed reactant gas mixture. A pair of CsI windows on opposing sides of the cryostat shroud allow an infrared beam to pass for spectroscopic detection.
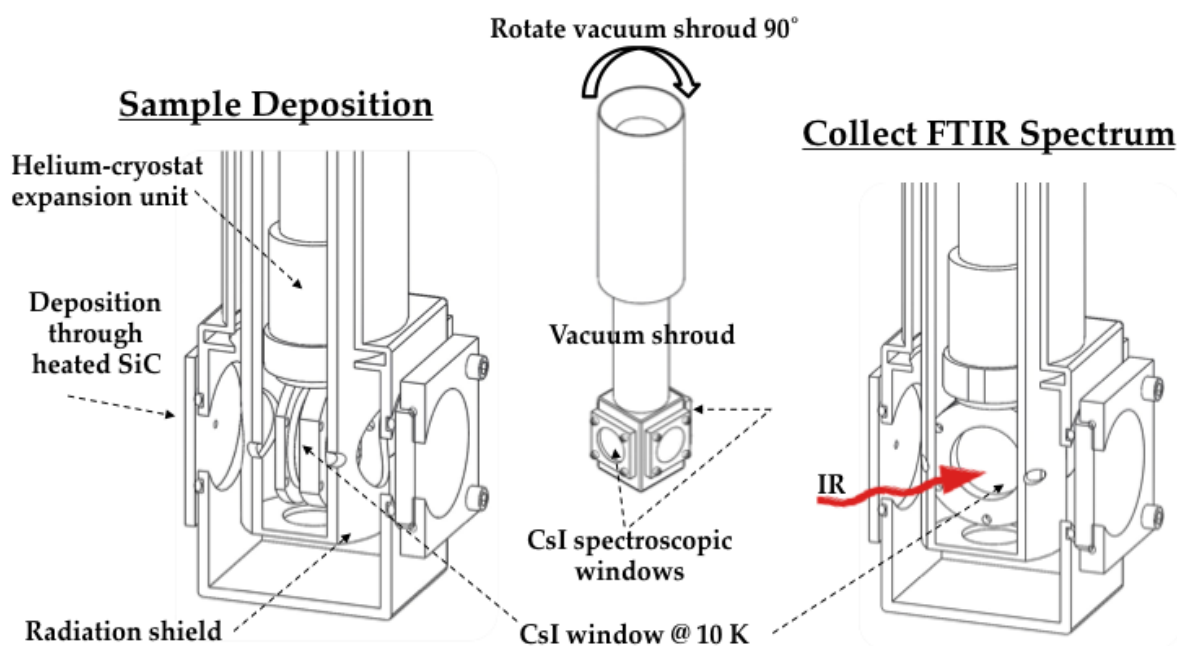
Figure 2.8: After deposition on the cold (10 K) window, the outer shroud is rotated 90° for spectroscopic analysis of molecules frozen in Ar.

Gaseous reactant mixtures were prepared in a glass 1.2 L reservoir upstream of the reactor in concentrations of $0.04-0.1\%$ in approximately 800 Torr Ar. In order to achieve resolved IR spectra typical deposition rates through a pulsed valve were 0.8 to 1 Torr min^{-1} from the reservoir (equivalent to $3-3.6$ mmol hr^{-1}), depositing between 3 to 6.5 mmol total

onto the cold window. Considering the concentration of the reactants in Ar, this is equivalent to about 10^{13} radicals per pulse [158]. The vibrational spectra are measured using a Nicolet 6700 infrared spectrometer equipped with a liquid N_2 cooled mercury/cadmium/telluride detector (MCT/A, $4,000-650$ cm^{-1}). The spectrometer is purged with purified dry air and the spectra are collected with the OMNIC software package on a Windows operating system. A background scan was taken approximately 1 to 2 hours prior to the sample scan; all spectra averaged 500 scans at 0.25 cm^{-1} resolution.

2.3   Analysis

2.3.1   Measurement of Product Ratios *via* Photoionization

The composition of a gas mixture has the potential to be quantified by photoionization spectroscopy. Ionization of a neutral target produces an ion signal which is proportional to the target concentration in the area sampled by the photon source. Beer's law can be applied to photoionization by VUV radiation, where the radiation (in photons s^{-1}) of frequency ν traversing a gas sample of distance z varies as

$$I(\nu) = I_0(\nu) \exp(-n\sigma(\nu)z) \tag{2.2}$$

where n is the density of the target gas and $\sigma(\nu)$ is the ionization cross-section. Since the VUV radiation is ionizing the gas, the resultant ion current j^+ is proportional to the difference between the incident $I_0(\nu)$ and transmitted radiation $I(\nu)$:

$$j^+ \propto [I_0(\nu) - I(\nu)] = I_0(\nu)[1 - \exp(-n\sigma(\nu)z)] \tag{2.3}$$

Finally, since it can be assumed that $(-n\sigma(\nu)z)$ is a small value, by a Taylor's series approximation the photoion current j^+ is proportional to the product $I_0 n\sigma(\nu)z$.

Converting this expression from a formulation of Beer's law to photoionization, the ion signal is a function of the number of molecules in the interaction region, the VUV photon flux through the volume, and the photoionization cross-section. However, neither the

absolute value of the volume nor the incident photon flux is known. The volume could be estimated with some uncertainty; however, it can be gathered into an empirical constant which is ultimately obtained by calibration or can factor out when taking ratios. The value of the photon flux is a power measurement using a calibrated energy-dependent photodiode. Therefore, to a first approximation the photoionization signal S_i^+ due to species i exiting the microreactor can be written as:

$$S_i^+ = Cn_i\Phi(E)\sigma_i(E) \tag{2.4}$$

where n_i is the number density of a particular species in the interaction volume, $\Phi(E)$ the photon flux at a given photon energy, and $\sigma_i(E)$ is the molecule's photoionization cross-section at the given photon energy. Here the signal S_i^+ refers to the total ion counts summed over the desired mass peak and normalized on the sampling time or number of scans. Expression (2.4) ignores the fact that, because of differential diffusion, mass differences and other factors, molecules of differing mass and collision cross-sections will be detected with different efficiency. This effect is taken into account by defining a mass discrimination factor D_i that is empirically determined by calibration [29]. Incorporating the mass discrimination factor and evaluating for the number density of the neutral target, one finds:

$$n_i = \frac{S_i^+}{CD_i\Phi(E)\sigma_i(E)} \tag{2.5}$$

where the constant C contains all the geometry dependent factors that remain unchanged with differing mass; this value could be obtained by absolute calibration.

However, while it will be difficult to use Eq. (2.5) to measure the absolute concentration of a species, it should be straightforward to measure the ratio of two different species, i and j:

$$\frac{n_i}{n_j} = \frac{S_i^+}{S_j^+}\frac{D_j\Phi_j\sigma_j}{D_i\Phi_i\sigma_i} \tag{2.6}$$

To measure the ratios *via* (2.6) requires knowledge of the photoionization cross-sections $\sigma(E)$, the measured photon flux $\Phi(E)$, and an estimate of the the mass discrimination factors

D_i. Under our operating conditions it was found using a calibrated gas mixture containing known quantities of H_2, Ar, Kr, and Xe in He that D_i is roughly proportional to $\sqrt{m_i/z}$. A similar approach to estimating mass discrimination factors was reported earlier [28].

Chapter 3

Pyrolysis of Furan in a Microreactor

The furans described in the previous chapters are the first of several possible new propellants proposed as second-generation biofuels, and the combustion and pyrolysis mechanisms of these complex, oxygen-containing species are of current interest [119, 121, 147, 148]. The goal of this thesis is to develop a complete molecular picture of the elementary decomposition steps of these molecules and this chapter will focus on the pyrolysis of furan, the parent compound of these substituted furans.

In earlier studies, the thermal decomposition of furan was studied in flow tubes [23, 47], shock tubes [39, 77, 99] and by IR homogeneous pyrolysis [54]. These studies were conducted over a wide range of pressure $(0.001-15,000$ Torr) and temperature $(500-3000$ K). The consensus from these experiments was that the initial step in pyrolysis of furan is ring opening to a diradical, ℓ-C_4H_4O. Subsequent fragmentation of ℓ-C_4H_4O led to the production of alkynes and ketene as the important primary products: furan $(+M) \rightarrow \ell$-$C_4H_4O \rightarrow [CO + CH_3C{\equiv}CH]$ or $[HC{\equiv}CH + CH_2{=}C{=}O]$. Two independent computational studies [80, 116] predicted that furan pyrolysis followed two separate paths to a pair of carbenes, collectively representing the "ℓ-C_4H_4O" species above. The α-carbene was computed to decompose to $HC{\equiv}CH + CH_2{=}C{=}O$ while the β-carbene was predicted to isomerize to allenyl-aldehyde, $CH_2{=}C{=}CH{-}CHO$, which fragments to $CH_3C{\equiv}CH + CO$ or breaks apart to radicals, $H + CO + HCCCH_2$. Calculations indicate formation of the carbene intermediate has a lower activation barrier than formation of a biradical [81, 116].

We have recently utilized a pulsed SiC μtubular reactor [137] to study the decomposition of furan. The pyrolysis experiments were carried out by passing a dilute mixture of furan (roughly 0.1%) entrained in a stream of a buffer gas (either He or Ar) through a $2-3$ cm long and 1 mm in diameter pulsed SiC reactor. The wall temperature was in the range $1200-1700$ K and the characteristic residence times in the reactor were estimated to be $100-200$ μsec. Products formed at early pyrolysis times in the reactor were identified by fixed frequency (118.2 nm or 10.487 eV) photoionization mass spectrometry (PIMS) as well as matrix-isolated infrared spectroscopy. In addition to [CO, HC≡CH, CH$_3$C≡CH, CH$_2$=C=O], clear evidence for the production of propargyl radical (HCCCH$_2$) was found. Based on these experiments [137], the predicted mechanism [81, 116] for the pyrolysis of furan was verified and is outlined in Scheme 3.1.
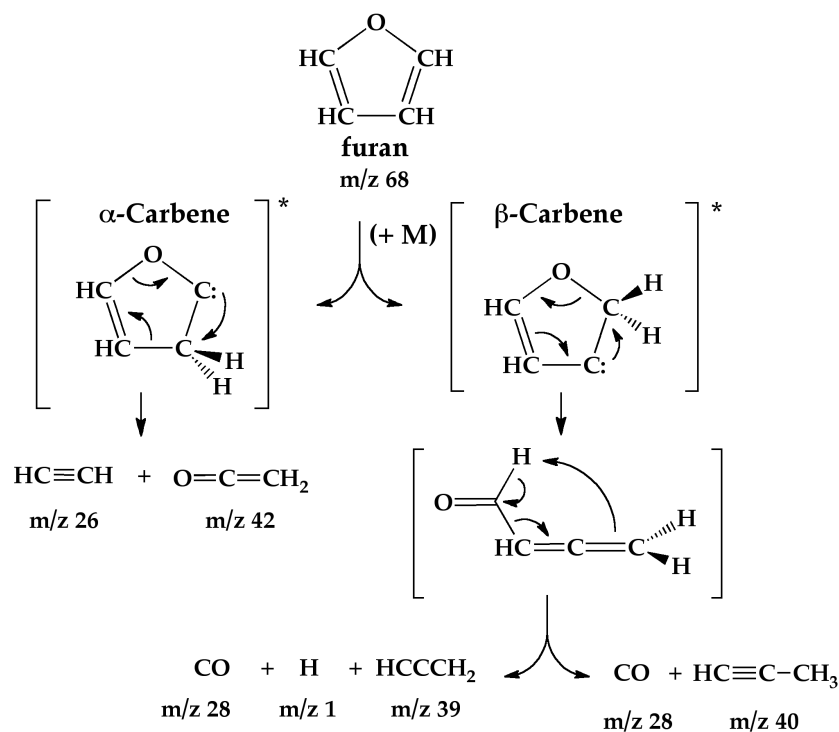
Scheme 3.1: Furan pyrolysis mechanism

The pyrolysis of furan-d$_0$ and furan-d$_4$ was re-studied in the heated continuous flow μtubular reactor described in Chapter 2.1.2. The goals of this study were to use tunable PIMS

to confirm the furan pyrolysis mechanism in Scheme 3.1 and also to measure the ratios of the different sets of products. Scheme 3.1 predicts that the observed furan pyrolysis products result from a sequence of unimolecular fragmentations involving carbene intermediates:

$$\text{Furan}(+\text{M}) \rightleftharpoons [\alpha-\text{carbene}] \rightarrow \text{HC}\equiv\text{CH} + \text{CH}_2=\text{C}=\text{O}$$

$$\text{Furan}(+\text{M}) \rightleftharpoons [\beta-\text{carbene}] \rightarrow \text{CH}_3\text{C}\equiv\text{CH} + \text{CO} \qquad (3.1)$$

$$\text{Furan}(+\text{M}) \rightleftharpoons [\beta-\text{carbene}] \rightarrow \text{H} + \text{HCCCH}_2 + \text{CO}$$
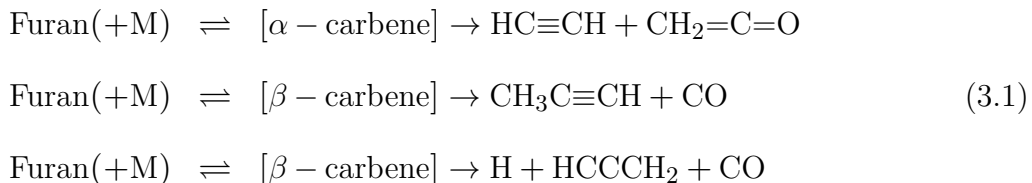
Two goals of this work are to measure the branching ratio of the pyrolysis products in Eq. 3.2 as a function of reactor temperature,

$$\frac{\alpha-\text{carbene}}{\beta-\text{carbene}} = \frac{[\text{HCCH}]}{[\text{CO}]} = \frac{[\text{HCCH}]}{[\text{CH}_3\text{CCH}]+[\text{HCCCH}_2]} = \frac{[\text{CH}_2\text{CO}]}{[\text{CH}_3\text{CCH}]+[\text{HCCCH}_2]} \quad (3.2)$$

in addition to the temperature-dependence of the ratio of propargyl radicals to methylacetylene.

As described in Chapter 2.3.1 it will be difficult to measure the absolute concentration of a species, however it should be straightforward to measure concentration ratios, specifically

$$\frac{\alpha-\text{carbene}}{\beta-\text{carbene}} = \frac{[\text{HCCH}]}{[\text{CO}]} = \frac{S_{26}^+}{S_{28}^+}\left[\frac{D_{\text{CO}}\Phi_{\text{CO}}\sigma_{\text{CO}}}{D_{\text{HCCH}}\Phi_{\text{HCCH}}\sigma_{\text{HCCH}}}\right] \qquad (3.3)$$

where the photon flux terms $\Phi(\text{E})$ cancel if the same photon energy is used to measure both species.

Similarly, the ratio of propargyl radicals to methylacetylene becomes:

$$\frac{\text{HCCCH}_2}{\text{CH}_3\text{CCH}} = \frac{S_{39}^+}{S_{40}^+}\left[\frac{D_{\text{CH}_3\text{CCH}}\Phi_{\text{CH}_3\text{CCH}}\sigma_{\text{CH}_3\text{CCH}}}{D_{\text{HCCCH}_2}\Phi_{\text{HCCCH}_2}\sigma_{\text{HCCCH}_2}}\right] \qquad (3.4)$$

with the same caveat regarding the ratio of photon fluxes. The ionization energies of carbon monoxide [38], acetylene [73], propargyl radical [41], methylacetylene [152], ketene [96], and furan [144] are known and to measure the ratios *via* (3.3) and (3.4) requires knowledge of the photoionization cross-sections of these species [27, 29, 107, 110, 156]. The mass discrimination factors D_i must also be estimated by calibration. As described in Chapter 2.3.1

and Appendix A.1, D_i is proportional to the square root of the mass, $\sqrt{m_i/z}$. A careful measurement of the ratios (3.2) and (3.4) is an important first step to quantify the initial pyrolysis steps of furan in the microreactor.

3.1   Experimental and Reactor Modeling

3.1.1   Experimental

Experiments were performed at Lawrence Berkeley National Laboratory's Advanced Light Source (ALS) using a continuous flow μtubular reactor and time-of-flight photoionization mass spectrometry (PIMS) to identify the mass-to-charge ratio (m/z) of the molecular species at the reactor exit. For the experiments presented in this chapter, the reactor is a silicon carbide (SiC) tube (0.66 mm i.d., 2 mm o.d., 2.5 cm long), mounted to a standard stainless steel Swagelok fitting (1/8 in to 3/8 in reducing union) and secured with a graphite ferrule (Restek, 1/8 in tube, inner diameter drilled out to fit reactor securely). For all experiments the mass flow rate was held constant at 280 sccm He with a commercial mass flow controller (MKS P4B 0-200 sccm N_2).

The pressure upstream of the reactor was measured with a capacitance manometer. With a constant mass flow rate the upstream pressure increased as the SiC wall temperature was increased due to larger frictional effects in the flow. Since the fluid is a gas, the increasing temperature results in increased viscosity (for He, μ approximately proportional to $T^{0.7}$); in addition, the density of the fluid is reduced as the temperature is increased, causing the velocity of the fluid to increase, resulting in more shear stress at the boundary. At room temperature the upstream pressure was about 100 Torr and with a measured SiC wall temperature of 1600 K the pressure increased to about 300 Torr. Approximately 1.5 cm of the SiC is resistively heated and the temperature of the outer wall is measured with a Type C thermocouple and also monitored with an infrared thermometer (Omega iR2P temperature controller, range 600-1600°C).

Reactant mixtures were prepared in stainless steel cylinders with concentrations between 0.0075% and 0.15% furan (furan-d_0: Aldrich, $\geq 99\%$, furan-d_4: Aldrich, ≥ 98 atom-% D) in helium. For a 0.01% mixture, furan was degassed through a freeze-pump-thaw cycle, and 0.5 Torr furan vapor collected and diluted with helium to a final cylinder pressure of 5000 Torr.

The molecular beam exiting the reactor is interrogated by synchrotron radiation about 12 cm downstream from the skimmer. The ions were detected using a microchannel plate and the signal recorded by ion counting. Most experiments reported here involved 100,000 mass spectra collected at each photon energy. Photoionization efficiency (PIE) curves for a given mass were obtained by plotting the summation of the background corrected ion signal in an appropriate mass range versus the selected photon energy, normalized by the photon flux measured by a photodiode with a calibrated energy-dependent efficiency.

3.1.2   Reactor Modeling

As described in Chapter 2.1.2.2, in order to understand the chemical reactions in these microreactors requires knowledge of the flow field within the reactor. However, since it is not possible to either insert sampling probes or gain optical access, as would be the case for a larger scale reactor or shock tube, the flow field within the reactor must be simulated using computational fluid dynamics (CFD) [49]. Since the tube is resistively heated to high temperatures using attached electrodes, there is also a strong axial gradient in the wall temperature, starting at the inlet, complicating the flow field. The heating method accelerates the flow, which results in decreasing pressure along the length of the tube. Both of these effects are shown in the calculated centerline pressure and temperature profiles along the length of the reactor in Fig. 2.3. Chemkin simulations [102] comparing the furan mechanisms of Tian [126], Sendt [116] and Wei [143] were performed to validate the pyrolysis results reported here. The μtubular reactor was simulated as a plug-flow reactor using the gas temperatures and pressures shown in Fig. 2.3 [49].

The "Tian" mechanism refers to a comprehensive mechanism of furan oxidation that

includes 206 species and 1368 elementary reactions. The secondary rate information for most species with six-carbons or less was included in the Chemkin simulations reported here, reducing the number of species to 127 and the number of reactions to 890. Larger species were excluded from the mechanism because they were not observed experimentally. Estimates of the pressure-dependence of furan dissociation [39] indicates that throughout most of the microreactor a high-pressure rate limiting expression should be valid, and therefore to a first approximation the high-pressure limiting rate constants of Tian *et al.* [126] have been used. Table 3.1 summarizes the important initiation rate constants, where FA is the abbreviation for the formyl allene intermediate of the β-carbene channel, $CH_2=C=CH-CHO$.

Table 3.1: Summary of initiation rate constants in the Tian [126] and Sendt [116] furan reaction mechanisms

Tian *et al.*: $k = AT^n \exp(-E_a/RT)$			
Reaction	A (s^{-1})	n	E_a (kJ mol^{-1})
1. Furan $\rightleftharpoons$ FA	2.3 x 10^{12}	0.414	296.6
2. FA $\rightleftharpoons$ HCO + C_3H_3	7.9 x 10^{14}	0.0	292.4
3. FA $\rightleftharpoons$ CO + CH_3CCH	6.8 x 10^{11}	0.419	185.1
4. Furan $\rightleftharpoons$ C_2H_2 + CH_2CO	1.8 x 10^{14}	0.534	362.3

Sendt *et al.*: $k = A \exp(-E_a/RT)$		
Reaction	A (s^{-1})	E_a (kJ mol^{-1})
5. Furan $\rightleftharpoons$ FA(1)	5.9 x 10^{13}	292.9
6. FA(1) $\rightleftharpoons$ FA(2)	2.2 x 10^{12}	23.6
7. FA(1) $\rightleftharpoons$ HCO + C_3H_3	1.4 x 10^{15}	289.1
8. FA(2) $\rightleftharpoons$ HCO + C_3H_3	7.9 x 10^{14}	292.5
9. FA(2) $\rightleftharpoons$ CO + CH_3CCH	1.7 x 10^{13}	167.8
10. Furan $\rightleftharpoons$ C_2H_2 + CH_2CO	9.0 x 10^{14}	344.3

The "Sendt" mechanism refers to the initiation rate constants in the Tian mechanism replaced with the rate information reported in Sendt *et al.* [116]. All secondary reaction rates and thermochemistry included in the model are those from the Tian mechanism. In contrast to Tian, the Sendt mechanism includes two rotamers of formyl allene, FA(1) and FA(2); the corresponding rate constants are presented in Table 3.1, reactions (5)−(10).

In general, both reaction mechanisms include the same initiation paths; however, the rate of conversion to the β-carbene in the Sendt mechanism is faster than in the Tian mechanism in the temperature range of these experiments. A recent ignition delay study by Wei *et al.* suggests a new rate for the conversion of furan to FA. This update is referred to as the "Wei" mechanism and includes a doubling of the A-factor of reaction (1) in Table 3.1

3.2   Confirmation of Furan Pyrolysis Mechanism

The mechanism for furan pyrolysis in Scheme 3.1 resulted from a previous set of experiments by Vasiliou et al. [137] with a SiC μtubular reactor operated with pulsed flow and fixed frequency PIMS and IR detection. Figure. 3.1 includes mass spectra that result from the thermal decomposition of furan in helium in a SiC reactor operated with continuous flow and tunable VUV ionizing radiation. In order to minimize bimolecular reactions, characterized here by the formation of methyl radical, shown in the left-panel of Fig. 3.1, a concentration of 0.01% furan in He is used. At this dilution methyl radical and other species (m/z 50, 52, and 78) due to bimolecular reactions become negligible.[1]   Accordingly a Chemkin simulation using the Tian furan mechanism [126] predicts negligible ($< 0.001\%$ of furan decomposition) formation of C_6H_6 at all temperatures and only trace amounts of CH_3 ($< 0.01\%$ of furan decomposition) as products formed by the exit of the reactor. Simulating the reactor conditions and including the secondary chemistry in the Tian mechanism indicates that all observed chemistry is unimolecular.

At 11.7 eV, the right-hand panel of Fig. 3.1 clearly demonstrates that pyrolysis of furan diluted to 0.01% in He follows the predictions of Scheme 3.1. Pyrolysis of furan-d_0 at 1600 K produces $HCCH^+$ (m/z 26), $HCCCH_2^+$ (m/z 39), CH_3CCH^+ (m/z 40), $CH_2{=}C{=}O^+$ (m/z 42) and the parent species furan (m/z 68) is almost completely consumed.

The pyrolysis of furan as a function of reactor temperature recorded at 10.4 eV ionizing

---

[1] One possible source of CH_3 could be reaction of H-atoms, produced by Scheme 3.1, with methylacetylene to give methyl radicals and allene: $H + CH_3CCH \rightarrow [CH_3CH{=}CH]^* \rightarrow CH_3 + HCCH$ and $[CH_3C{=}CH_2]^* \rightarrow H + CH_2{=}C{=}CH_2$
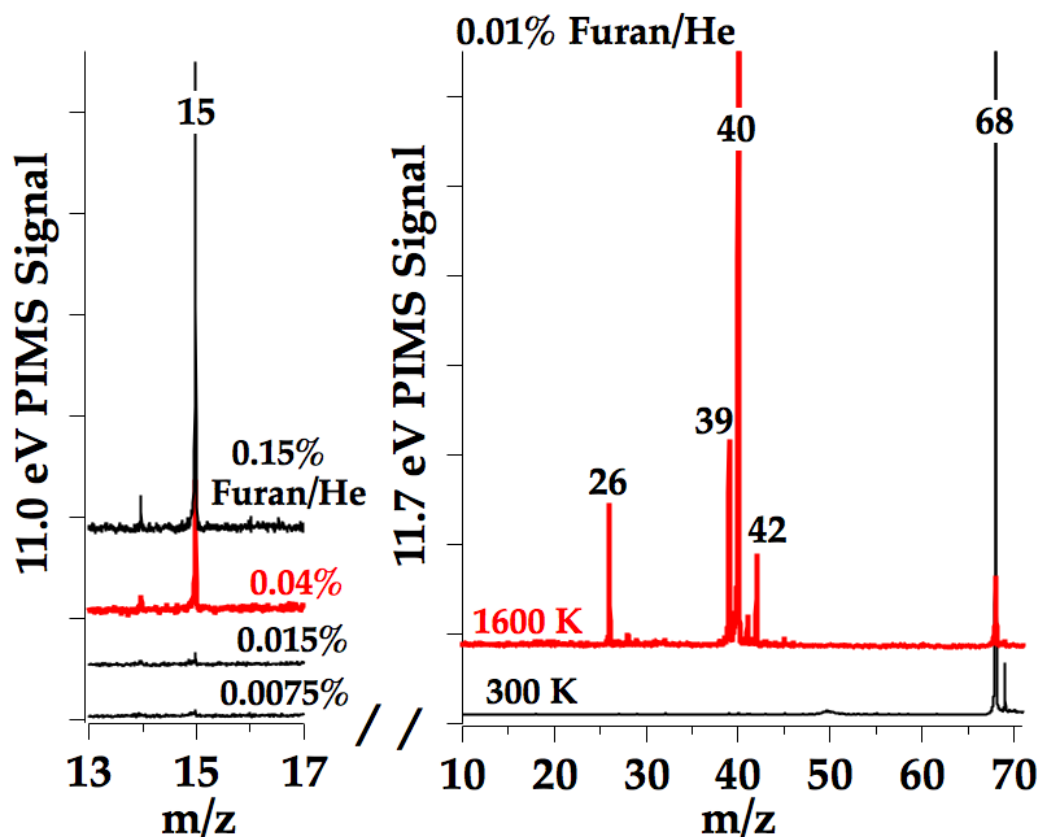
Figure 3.1: Elimination of bimolecular chemistry as shown by the disappearance of m/z 15 (CH_3), left panel. The PIMS at 11.7 eV (right-hand panel) shows primary products from furan decomposition at 1600 K in a continuous flow of helium: $HCCH^+$ (m/z 26), CH_3CCH^+ (m/z 40), CH_2CO^+ (m/z 42), in addition to propargyl radical, $HCCCH_2^+$ (m/z 39). The PIMS for the dilution study at 11.0 eV sampled 5,000,000 mass spectra, compared to 100,000 for the PIMS at 11.7 eV.

radiation is shown in Fig. 3.2. With the reactor at 300 K, only signals for furan (m/z 68) and the ^{13}C isotope peak (m/z 69) are observed. As the reactor is heated between 1200 K and 1300 K, furan decomposition begins. Signals for CH_3CCH (m/z 40) and CH_2CO (m/z 42) are identified by PIMS and corresponding PIE curves. Heating the reactor to 1500 K leads to the production of propargyl radical at m/z 39. In addition, at 1500 K and above a small amount of allene (CH_2=C=CH_2) is identified by the PIE curve at m/z 40; this molecule is likely formed [126] by isomerization of CH_3CCH and not produced by unimolecular dissociation of furan [116].
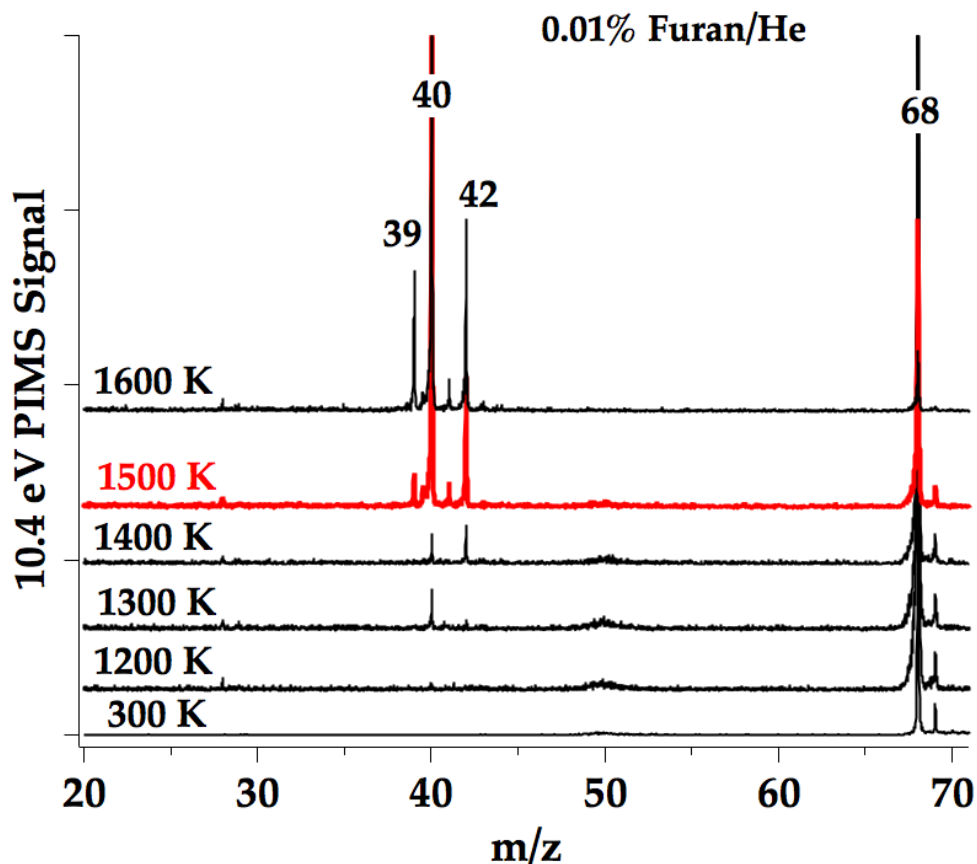
Figure 3.2: Product mass spectra at 10.4 eV as a function of SiC wall temperature. Pressure of the gas mixture at the reactor inlet (P_i) was measured as a function of wall temperature (T_w): $(T_w = 1600$ K, $P_i = 288$ Torr $)$; $(T_w = 1500$ K, $P_i = 274$ Torr); $(T_w = 1400$ K, $P_i = 256$ Torr); $(T_w = 1300$ K, $P_i = 244$ Torr); $(T_w = 1200$ K, $P_i = 225$ Torr); and $(T_w = 300$ K, $P_i = 101$ Torr)

Figure 3.3 is a set of PIE curves at m/z 39 that unambiguously identifies propargyl radical as a thermal cracking product of furan. When the reactor temperature is 1400 K no signal at m/z 39 is observed. Upon heating to 1600 K, the known ionization threshold for propargyl radical [41] is observed at 8.7 eV and the photoionization cross-section of propargyl radical [110] matches the PIE(m/z 39) resulting from furan pyrolysis until about 10 eV. Above this photon energy vibrationally hot CH_3CCH^+ and $CH_2{=}C{=}CH_2^+$ in the molecular beam can dissociatively ionize to $C_3H_3^+$, causing the signal at m/z 39 to increase. The increasing signal could also in part be due to an improperly calibrated photodiode.
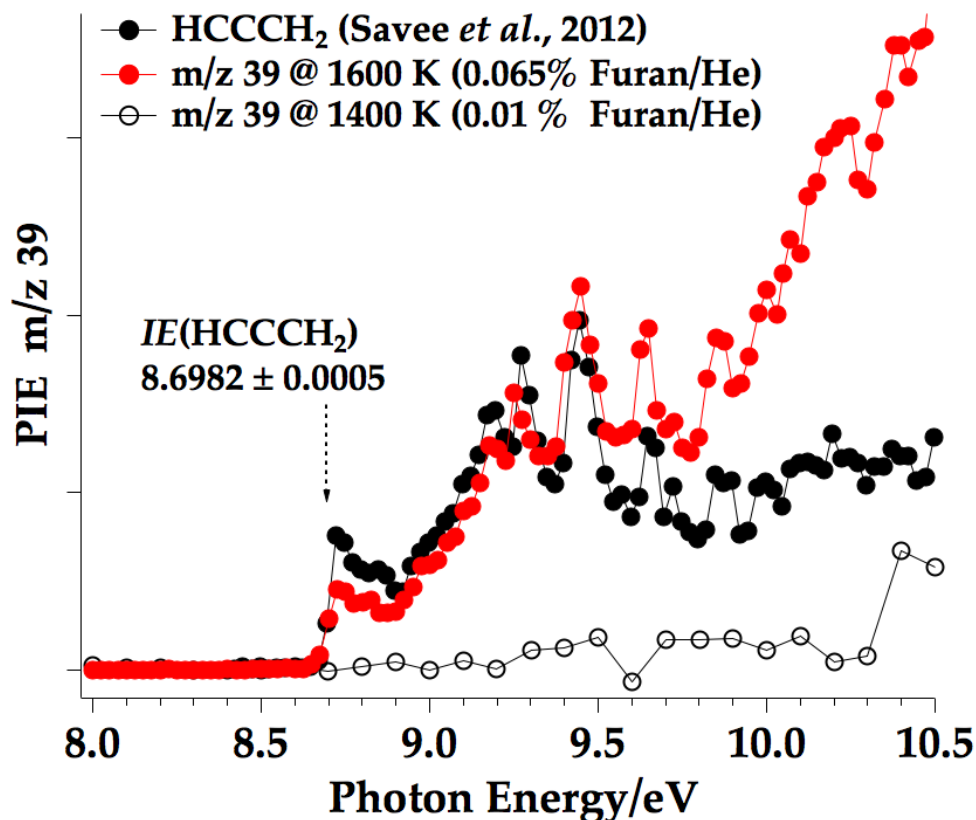
Figure 3.3: Photoionization efficiency curves of furan/He mixtures at m/z 39 compared with the measured photoionization cross-section. Curve at 1600 K grows in at 8.7 eV [41] and exhibits similar sharp features to those observed by Savee *et al.* [110] indicative of autoionization states in propargyl radical.

In addition to furan-d_0, a 0.01% mixture in He of its isotopomer, furan-d_4, was also pyrolyzed. PIE curves and PIMS at 11.7 eV detects the expected species: $DCCD^+$ (m/z 28), $DCCCD_2^+$ (m/z 42), CD_3CCD (m/z 44), and $CD_2=C=O^+$ (m/z 44). In addition, a furan-d_3 impurity (m/z 71) of approximately 4-5% is observed and produced ions at m/z 41 (propargyl-d_2) and m/z 43 (methylacetylene-d_3). When a cross-over experiment of a 0.01% 1:1 mixture of [furan-d_0:furan-d_4] is pyrolyzed, the primary products include: [$HCCH^+$ (m/z 26), $HCCCH_2^+$ (m/z 39), CH_3CCH^+ (m/z 40), and $CH_2=C=O^+$ (m/z 42)] as well as [$DCCD^+$ (m/z 28), $DCCCD_2^+$ (m/z 42), CD_3CCD^+ (m/z 44), and $CD_2=C=O^+$ (m/z 44)]. As shown in Fig. 3.4, the observed signals at m/z 41 and 43 include the ^{13}C isotope of
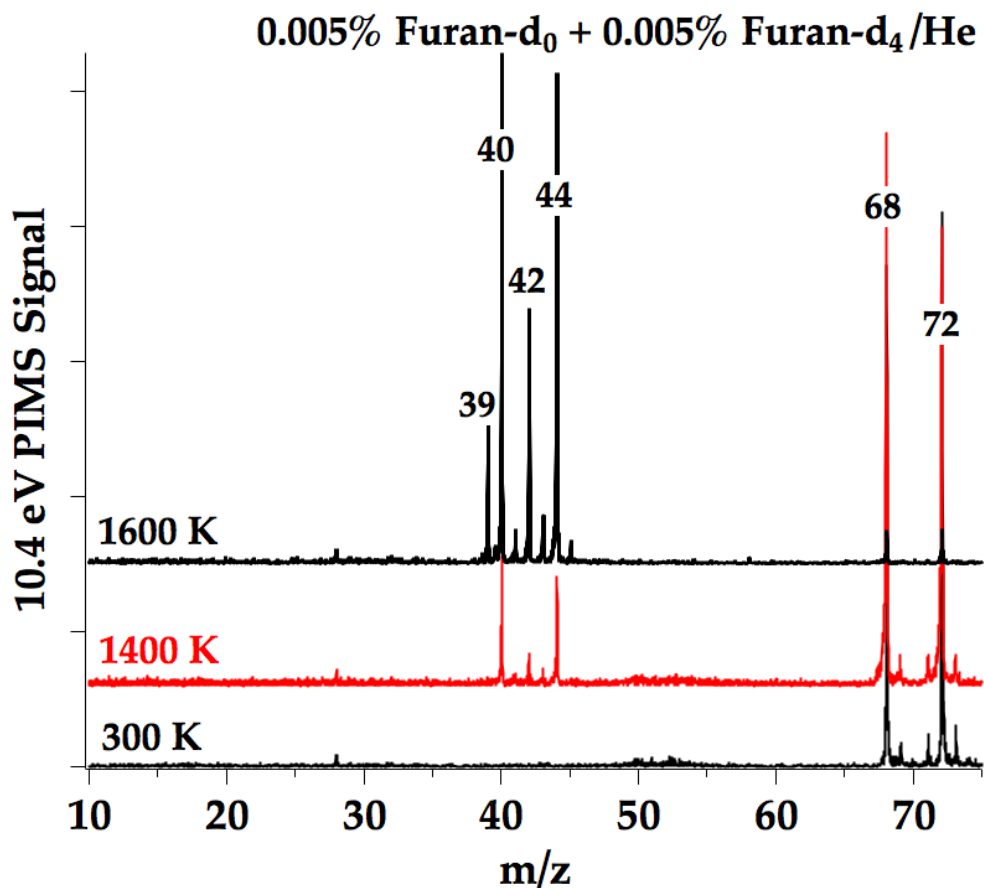
Figure 3.4: Mass spectra of a furan-d_0/furan-d_4 cross-over experiment at 10.4 eV as a function of reactor wall temperature.

CH_3CCH and $[CH_2{=}C{=}O + DCCCD_2]$, respectively. In addition propargyl-d_2 (m/z 41) and methylacetylene-d_3 or ketene-d_1 (m/z 43) are observed from the furan-d_3 impurity in the fully deuterated furan sample. Considering the expected signal from the ^{13}C isotopes and from the furan-d_3 impurity, the observed signals at m/z 41 and 43 are within the limit of uncertainty, suggesting that only unimolecular decomposition is observed at this concentration of furan.

Figures 3.1−3.4 confirm the predictions of Scheme 3.1. PIMS below 12 eV detects HCCH (m/z 26), $HCCCH_2$ (m/z 39), CH_3CCH (m/z 40), CH_2CO (m/z 42), and furan (m/z 68), but not H atoms [90] or carbon monoxide [38]. The pyrolysis of furan in a hot, continuous flow SiC microreactor is in agreement with interpretations based on the earlier shock tube measurements [39, 77] and the pulsed reactor findings [137]; moreover, the present results are

consistent with the theoretical predictions [116, 126].

3.3   Measurement of the Ketene to Acetylene Ratio

The mechanism in Scheme 3.1 predicts that the ratio of ketene to acetylene will be unity. Application of Eq. (2.6) to measure the ketene/acetylene ratio yields expression (3.5):

$$\frac{\text{CH}_2\text{CO}}{\text{HCCH}} = \frac{S_{42}^+}{S_{26}^+} \left[\frac{\sqrt{26}}{\sqrt{42}} \frac{\Phi_{\text{HCCH}}}{\Phi_{\text{CH}_2\text{CO}}} \frac{\sigma_{\text{HCCH}}}{\sigma_{\text{CH}_2\text{CO}}} \right] \tag{3.5}$$

When photoionization measurements of CH_2CO^+ and HCCH^+ are carried out at a common energy, the photon flux $\Phi(E)$ terms cancels in Eq. (3.5).
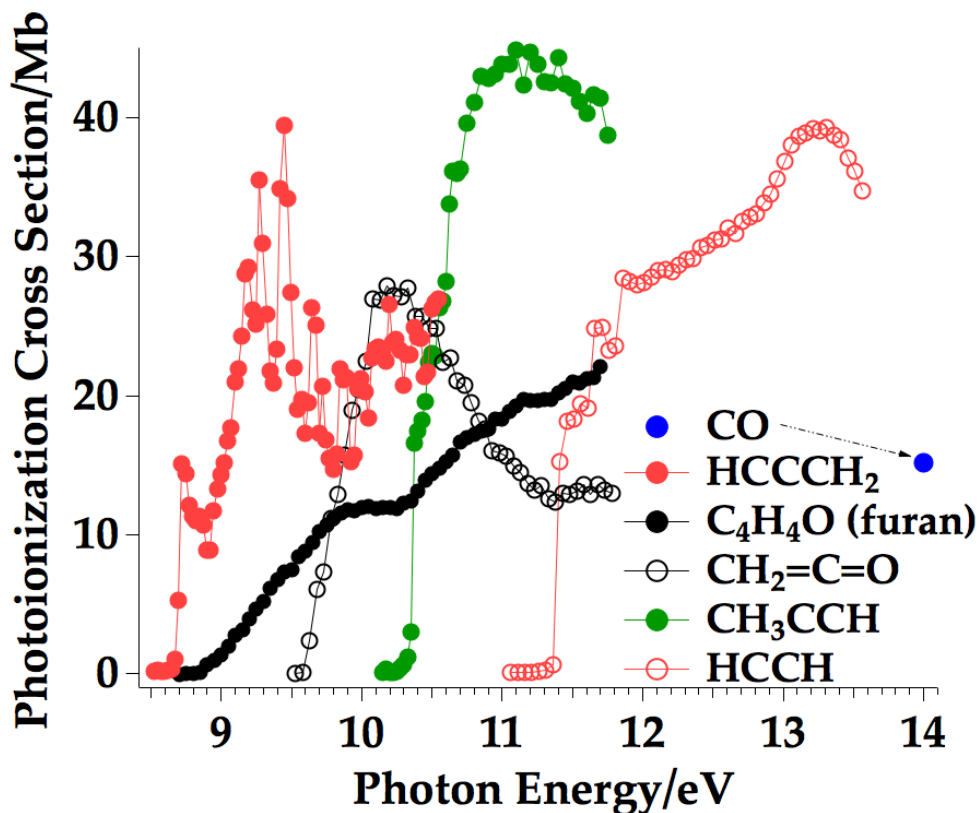
Figure 3.5: The literature photoionization cross-sections used for analysis in this work; carbon monoxide [107], acetylene [29], propargyl radical [110], methylacetylene [27], ketene [156], and furan [156].

Figure 3.5 includes the measured photoionization cross sections for carbon monoxide [107], acetylene [29], propargyl radical [110], methylacetylene [27], ketene [156], and

furan [156]. The cross sections for ketene and acetylene overlap in a small window, $11.4-11.7$ eV. However, at these energies the parent furan dissociatively ionizes to produce CH_2CO^+ and other daughter ions,

$$\text{Furan}^* + \hbar\omega_{11.7eV} \rightarrow (\text{Furan}^*)^+ \rightarrow CH_2CO^+ \tag{3.6}$$
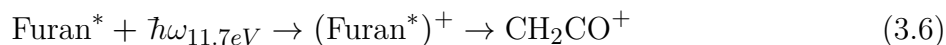
which greatly complicates the effort to estimate the ratio of acetylene to ketene *produced by the pyrolysis.* Consequently, two different photon energies were chosen to make this estimate over the entire temperature range: 10.4 or 10.5 eV for ketene, and 11.7 eV for acetylene. The results of the calculations shown in Fig 3.6 indicate an approximate temperature independence; however as a group they fall significantly below the expected ratio of unity. These calculations, however, require knowledge of the photon fluxes $\Phi(10.4$ eV$)$, $\Phi(10.5$ eV$)$ and $\Phi(11.7$ eV$)$, which are based on current measured with a photodiode and a manufacturer's calibration. We have found empirically that photon fluxes at energies above approximately $10-11$ eV are considerably underestimated by the diode measurement. In addition to the previously noted qualitative difference between the propargyl PIE curve above 10 eV a similar discrepancy was found for the PIE curve of room temperature furan. Whether this is a problem with the photodiode calibration or an unknown instrumental issue, it seems logical to attribute the "low" ketene to acetylene ratios determined above to this effect. This finding of "excess" HC≡CH is consistent with the observed differences between PIEs measured in this work, indicating that quantitative measurements of this sort must be done at the same, or very similar, photon energies to be reliable.

Fortunately, the problems above can be circumvented at the highest temperature 1600 K, where the destruction of the furan precursor is nearly complete and the ketene ions produced by dissociative ionization of furan are minimal. Using 11.6 or 11.7 eV to photoionize both acetylene and ketene, the photon flux contributions in Eq. (3.5) cancel, and the results obtained are shown in Fig. 3.6. With the common photon energy measurements the ratio is effectively unity, as expected from the chemical mechanism in Scheme 3.1 and predicted by
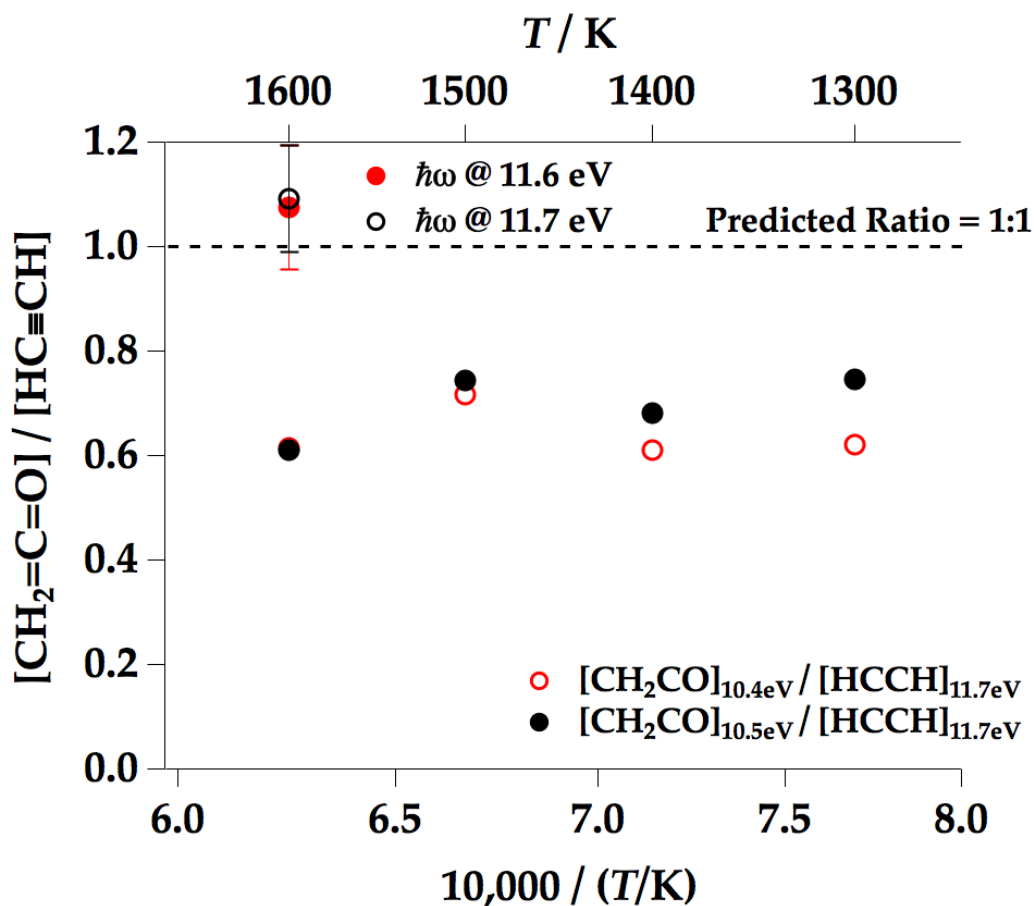
Figure 3.6: The ketene to acetylene ratio as measured from a 0.01% furan/He mixture by PIMS at 11.6 eV and 11.7 eV is unity. The ratio as measured by CH_2CO^+ signal at lower photon energies compared to $HCCH^+$ is offset from unity but consistent over the temperature range.

simulations. However, in the other measurements where different photon energies were used, the errors due to the photon flux measurement are constant and presumably independent of temperature, so that the corresponding data in Fig. 3.6 should deviate from the actual ratios by a simple scaling factor.

The uncertainties for the ketene to acetylene measurement at common photon energies in Fig. 3.6 are determined by propagating the uncertainty associated with each molecule's photoionization cross-section, the measured signal and the mass discrimination factor. The uncertainty associated with the photoionization cross-section of ketene [156] at 11.6 and 11.7

eV is estimated to be 0.8 Mb and 0.5 Mb, respectively, while the uncertainty for acetylene [29] is about 1 Mb at these energies. Since only ratios are considered for this work and not absolute number densities, the level of uncertainty with respect to the mass discrimination factor is reduced for similar masses. A detailed table of uncertainties is included in Appendix B.

3.4 Measurement of the α-Carbene to β-Carbene Ratio

The temperature-dependent PIMS in Fig. 3.2 demonstrates that thermal decomposition of furan begins with the appearance of $CH_3C{\equiv}CH$ (m/z 40) from the β-carbene and $CH_2{=}C{=}O$ (m/z 42) from the α-carbene and suggests that the branching ratio of products resulting from these two channels changes as the reactor is heated. From Scheme 3.1 it is predicted that the $[\alpha/\beta]_T$ ratio can be measured in a variety of ways as indicated in Eq. (3.2). Taking the ionization potentials and cross-sections (see Fig. 3.5) into account, the following approaches have been used to estimate this ratio experimentally:

$$\frac{[CH_2CO\ @\ 10.4eV]}{[CH_3CCH\ @\ 10.4eV] + [HCCCH_2\ @\ 10.4eV]} \tag{3.7}$$

$$\frac{[CH_2CO\ @\ 10.5eV]}{[CH_3CCH\ @\ 10.5eV] + [HCCCH_2\ @\ 10.5eV]} \tag{3.8}$$

$$\frac{[HCCH\ @\ 11.7eV]}{[CH_3CCH\ @\ 10.4eV] + [HCCCH_2\ @\ 10.4eV]} \tag{3.9}$$

$$\frac{[HCCH\ @\ 13.6eV]}{[CO\ @\ 14.0eV]} = \frac{S_{26}^+}{S_{28}^+} \frac{\sqrt{28}}{\sqrt{26}} \left[\frac{\Phi(14.0eV)\ \sigma_{CO}}{\Phi(13.6eV)\ \sigma_{HCCH}} \right] \tag{3.10}$$

however, only relationship (3.7) has been used in the construction of Fig. 3.7. Calculation of the ratio based on Eq. (3.8) gives comparable results while the latter two estimates require detailed considerations discussed below. Also included for comparison is the curve fit from Fulle *et al.* [39] who measured the ratio of HCCH to CO in a shock tube, quantifying these species using electron impact, time-of-flight mass spectrometry. Chemkin-calculated profiles of the ratio of total ketene at the reactor exit to the sum of methylacetylene, propargyl and allene using the furan mechanisms of Sendt [116], Tian [126] and Wei [143] are also included.

As shown in Fig. 3.7, the α-carbene to β-carbene ratio determined from Eq. (3.7)
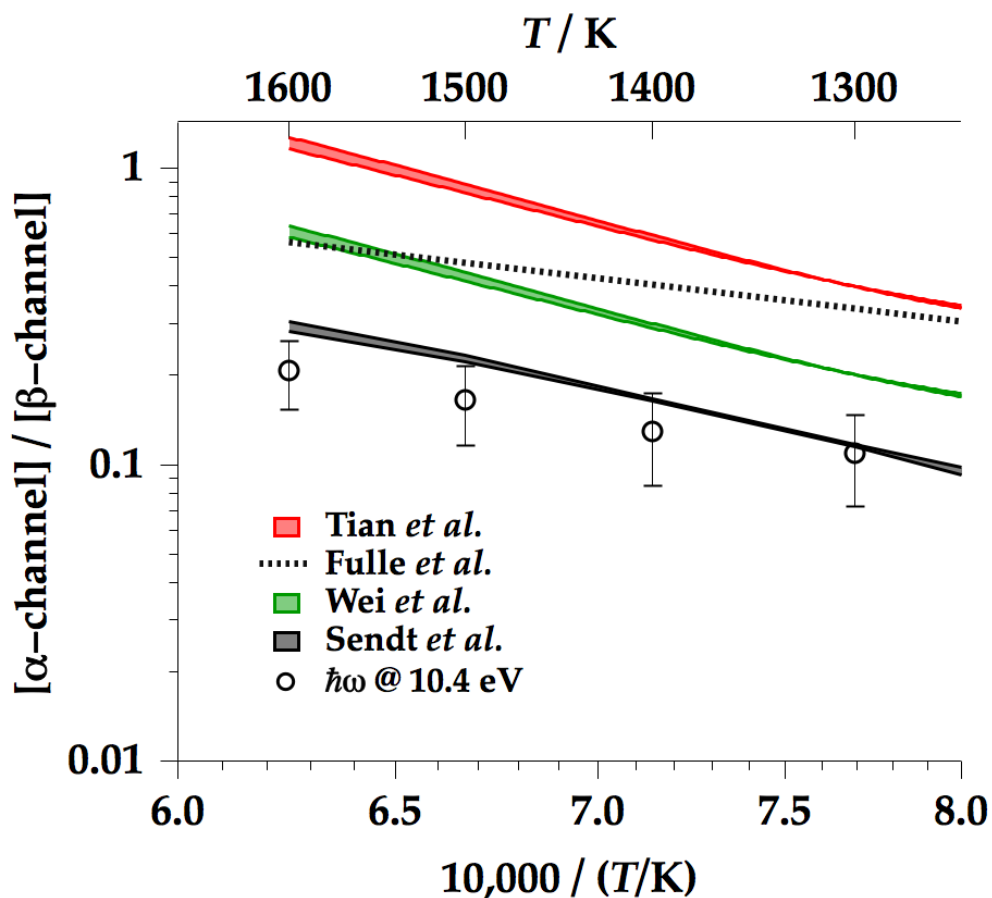
Figure 3.7: Ratio of products measured at 10.4 eV from the α-carbene (CH_2CO^+) relative to the β-carbene (CH_3CCH^+ and $HCCCH_2^+$) as a function of temperature. Also included are results of a shock tube study by Fulle *et al.* [39], and Chemkin simulations using the wall and centerline pressure/temperature conditions with three different furan kinetic mechanisms [116, 126, 143].

exhibits a smooth behavior as a function of reciprocal temperature, increasing from about 10% at 1300 K to 20% at 1600 K. The results of the shock-tube study by Fulle *et al.* [39] are qualitatively consistent with our experimental results; however they observe more flux through the α-carbene, likely because the non-uniform temperature in the microreactor results in temperatures below the measured wall temperature. For this reason, the Chemkin simulations used the pressure/temperature profiles (Fig. 2.3) at three radial locations in the reactor: centerline, along the wall and halfway between centerline and the wall [49]. As shown in Fig. 3.7, the temperature-dependence of the branching ratio as measured in

this work is consistent with the predictions of Sendt *et al.* [116], and lower than results with the Tian [126] and Wei [143] mechanisms. The upper limits on all three curves are calculated based on conditions along the reactor wall, while the lower limit is determined from centerline profiles. The origin of the discrepancy between experimental and theoretical results could be twofold. One possibility is that the initiation chemistry in the Tian and Wei mechanisms simply underestimates the rate of formation of formyl allene (CH_2=C=CH-CHO) from furan (or overestimates unimolecular formation of ketene and acetylene). A second possibility could be related to the pressure dependence of their reaction rates. Based on estimates of Fulle *et al.* [39], it is likely that the high-pressure limiting rate constants of Tian are valid at the entrance of the tubular reactor where the pressure is between 200 and 300 Torr. But as shown in Fig. 2.3, the pressure rapidly decreases along the length of the reactor, requiring rate constants valid in the fall-off region in order to make an accurate comparison between our experimental results and the simulations. Unfortunately, no pressure-dependent rate constants for the initiation reactions are provided in the Tian mechanism. Fulle *et al.* employed a formulation of furan disappearance in the fall-off region; however, this expression cannot be applied to the branching ratio of the two channels.

Table 3.2 compares the extent of furan consumption as a function of temperature to that of predictions. The fraction of furan consumed was determined by measurement of the photoionization signal at three different temperatures compared to the observed signal in a room temperature sample of the same mixture. At the upper wall temperature about 90% of the furan decomposed to products; the corresponding models predict between $35-70\%$ conversion over the temperature extremes, demonstrating the sensitivity of this decomposition to temperature. An effort to create a fully reactive CFD model including the radial temperature and pressure profiles is in progress [49].

The ratios that require measurements at different photon energies are those in Eq. (3.9) and (3.10). In order to determine ratio (3.9) an expedient workaround is to use the same photon energies used to estimate the HCCH to CH_2CO ratio (10.4 or 10.5 eV vs. 11.7 eV) in

Table 3.2: Extent of furan conversion (%) as a function of wall temperature with a mixture of 0.01% furan-d$_4$/He monitored by 10.4 eV VUV PIMS compared to predictions from Sendt [116], Tian [126] and Wei [143] mechanisms

T (K)	Exp.	%-Conversion Sendt*	Tian*	Wei*
1400	1.3 ± 0.8	$1.7-1.9$	$1.3-1.5$	$2.0-2.4$
1500	49 ± 3	$10-14$	$8.7-12$	$13-18$
1600	92 ± 6	$34-50$	$35-53$	$46-66$

*Limits of %-conversion as calculated using (T, P) at centerline (lower limit) and along-wall (upper limit)

Section 3.3. However, this introduces the same systematic error into the determination of ratio (3.9) as in the determination in Eq. (3.5). Consequently, the HCCH to (HCCCH$_2$ + CH$_3$CCH) ratio in Table 3.3 has been corrected for the average observed shift in the ratio, as shown in Fig. 3.6. When this empirical correction is applied, the curves are similar to those taken at the same photon energy.

Table 3.3: Ratio of the α-carbene relative to the β-carbene (expressed as %) as a function of reactor wall temperature using the ratios in Eqs. (3.7) through (3.10)

Eq.	eV	Wall Temperature (K) 1300	1400	1500	1600
3.7	10.4	10.9 ± 3.7	12.9 ± 4.4	16.5 ± 5.0	20.7 ± 5.4
3.8	10.5	11.6 ± 1.9	14.0 ± 1.4	17.3 ± 3.0	20.6 ± 3.6
3.9	10.4, 11.7	11.2 ± 1.7	13.5 ± 1.2	14.7 ± 2.5	21.6 ± 3.7
3.10*	13.6, 14.0	4.5	11.4	15.6	17.0

*less an estimate of the temperature-dependent background level of CO

Determination based on Eq. (3.10) uses a smaller difference in photon energies than that in Eq. (3.9), however it requires other considerations. Specifically, we know there are interfering signals at m/z 28 due to N$_2^+$ that results from photoionization of background air in the chamber by residual, higher VUV harmonics that are not filtered out from the synchrotron. In addition, at these high temperatures, CO is produced from wall reactions of the SiC μtubular reactor by oxygen impurities, and production of CO by other mechanisms (dissociative photoionization) at such high photon energies is another possibility. Taken

together, it is then perhaps not surprising that the HCCH to CO ratio estimated from Eq. (3.10) and documented in Table 3.3 does not display a smooth downward trend as a function of reciprocal temperature. Nevertheless, the ratio determined here is low, as might be expected because of both the extra sources of CO mentioned above and the higher photon energy used to measure it, but not entirely incongruent with the preferred determinations by Eqs. (3.7) and (3.8).

3.5   Measurement of the Propargyl Radical to Methylacetylene Ratio

Scheme 3.1 predicts that both CH_3CCH and $HCCCH_2$ result from the favored β-carbene fragmentation mechanism. A radical channel to form $HCCCH_2$, CO, and H is observed at the higher temperatures in Fig. 3.2. The propargyl radical to methylacetylene ratio is measured at a common photon energy, simplifying Eq. (3.4) simplifies to:

$$\frac{HCCCH_2}{CH_3CCH} = \frac{S_{39}^+}{S_{40}^+} \left[\frac{\sqrt{40}\ \sigma_{CH_3CCH}}{\sqrt{39}\ \sigma_{HCCCH_2}} \right] \tag{3.11}$$

Figure 3.5 indicates that the overlap of $\sigma_{HCCCH_2}(E)$ and $\sigma_{CH_3CCH}(E)$ is the small energy window of $10.4-10.5$ eV. Unfortunately in this energy range, m/z 39 is observed in the photoionization of rotationally/vibrationally excited methylacetylene, which is most likely due to dissociative photoionization of $(CH_3CCH^*)^+$. An adjustment for methylacetylene dissociative ionization was approximated by heating CH_3CCH over a temperature range of 1300 K-1600 K and measuring the m/z 39 ion signal relative to that of m/z 40. It is estimated that 6% of observed CH_3CCH^+ will dissociatively ionize to give m/z 39 at 1600 K and 3% at 1500 K. It should also be considered in the evaluation of Eq. (3.11) that the photoionization cross-sections of both molecules in their ground state, $\sigma(CH_3CCH)$ and $\sigma(HCCCH_2)$, may be quite different than those for the rotationally/vibrationally excited species, $\sigma(CH_3CCH^*)$ or $\sigma(HCCCH_2^*)$. For example, ionization of $CH_3C{\equiv}CH$ is a decidedly non-vertical process [10] and the dependence of the cross-section on photon energy will consequently be sensitive to vibrational excitation.
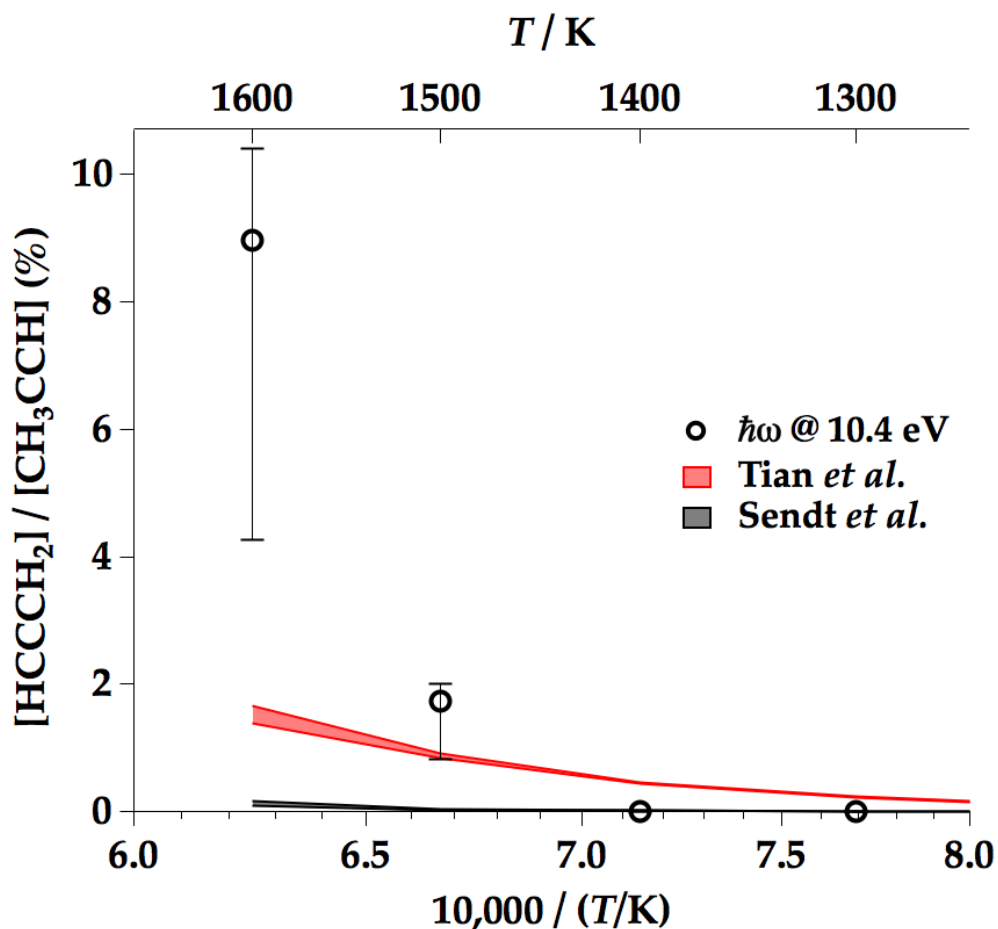
Figure 3.8: PIMS of a 0.01% mixture of furan/He were used to measure the ratio of propargyl to methylacetylene as a function of reactor temperature; here these values are compared to predictions of propargyl formation from the Sendt [116] and Tian [126] kinetic mechanisms.

Figure 3.8 includes the propargyl to methylacetylene ratio over the range of $1300\,K-1600$ K. The ratio was computed from Eq. (3.11) using the measured photoionization cross-sections for propargyl radical [110] and methylacetylene [27] and adjusted for the observations of dissociative ionization discussed above. At the lower temperatures, $1300\,K-1400$ K, there are no propargyl radicals present and only CH_3CCH is detected from the β-carbene channel. As the reactor is heated, the fraction of propargyl radical to methylacetylene rises from roughly 2% (1500 K) to about 10% (1600 K).

The furan mechanisms of Sendt [116] and Tian [126] predict much less $HCCCH_2$ radical than what is observed experimentally. A rate of production analysis shows that the Sendt

mechanism predicts that nearly all $HCCCH_2$ formed is the result of $CH_3C\equiv CH \rightarrow H + HCCCH_2$. The Tian mechanism on the other hand predicts that most propargyl is formed from unimolecular dissociation of formyl allene.

The uncertainty limits included in Fig. 3.8 have been determined by propagating the uncertainty associated with each of the components required for calculating the ratios considering the photoionization cross-sections $\sigma_i(E)$ and the measured ion signal S_i^+. As indicated above, there is a large uncertainty associated with dissociative ionization of methylacetylene to m/z 39, $CH_3C\equiv CH + \hbar\omega_0 \rightarrow (CH_3CCH^*)^+ \rightarrow H + HCCCH_2^+$. In order to make an accurate estimate of the radical channel to the closed shell channel the signal of m/z 39 should be analyzed at a lower energy, around 9 eV, and methylacetylene at 10.4 eV. However when analyzing over this large energy range we encounter the problems associated with uncertainty in the photocurrent measured by the photodiode. The ratio of $HCCCH_2$ at 9.1 eV to CH_3CCH at 10.4 eV could be as low as 4% at 1600 K and this uncertainty is indicated in the lower limits of the error bars in Fig. 3.8.

3.6   Conclusions on Furan Pyrolysis

Figures 3.1−3.3 effectively summarize the results of furan pyrolysis experiments performed in a continuous flow SiC μtubular reactor. These findings confirm the earlier results [137] for furan pyrolysis in a pulsed SiC reactor that used both He and Ar buffer gases. The initial steps in the pyrolysis are shown in Scheme 3.1, which provides a general chemical mechanism for this important process.

The branching ratio of the α-carbene relative to that of the β-carbene in Scheme 3.1 is an important measurement for proper characterization of this reaction. At the lowest temperature studied (1200 K), there are clearly products from both channels and roughly 80% of the reaction goes through the β-carbene intermediate. A weak temperature dependence is observed, which is qualitatively consistent with that found by a shock-tube study fifteen years ago [39] under slightly different reaction conditions. While the shock-tube findings of

Fulle *et al*. predict that more reactive flux goes through the α-carbene, both studies agree that the β-carbene channel is favored.

Figure 3.8 shows that as reaction proceeds through the β-carbene channel, the formyl allene intermediate, CH_2=C=CH-CHO, mostly rearranges to CH_3CCH + CO and very little decomposes to H + CO + $HCCCH_2$. Indeed, below 1500 K, there are no $HCCCH_2$ radicals detected. As the reactor temperature approaches 1600 K at most 10% of the products resulting from CH_2=C=CH-CHO decomposition are H + CO + $HCCCH_2$. The remaining 90% of products from formyl allene are carbon monoxide and methylacetylene.

This study shows the degree to which the μtubular reactor can by used to study high-temperature pyrolysis. In addition to the valuable qualitative speciation information provided in these studies, the present work has shown that quantitative information such as branching ratios can be measured with synchrotron radiation PIMS. Although practical problems with dissociative photoionization and cross-section dependence on temperature remain with such analysis, a major issue at present is the ability to use the CFD results of the thermodynamic conditions within the reactor coupled with the fluid dynamics of the supersonic expansion. With accurate simulations of this effect it should be possible to make quantitative measurements of reaction rates using the microreactor [49].

<div align="center">

Chapter 4

Pyrolysis of 2-Methoxyfuran

</div>

Alkylated furans and furanic ethers are among a variety of molecules derived from non-edible biomass that offer a renewable path to biofuels and other platform chemicals [71]. However, the combustion and pyrolytic behavior of many of these oxygenated species are not well-known and in order utilize them as fuels it is important to understand how they break apart thermally. The goal of this work is to identify the nascent pyrolysis products of 2-methoxyfuran, the simplest furanic ether.
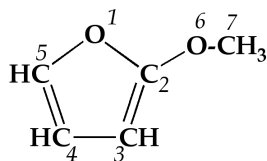
Scheme 4.1: The simplest furanic ether, 2-methoxyfuran, and the numbering scheme used throughout the text

Methoxyfuran was included in a study of several aromatic compounds relevant to coal-combustion by Bruinsma *et al.* [23]. The disappearance of methoxyfuran as a function of temperature was measured in a coiled quartz flow reactor operated at 0.125 MPa (938 Torr), a residence time of 5 s and a sample concentration of at most 500 ppm in argon. The primary products detected by gas chromatography at 10% conversion included CO, CO_2 and trace amounts of other species. The authors also noted that this molecule was extremely unstable with respect to other substituted heterocycles; the observed onset for decomposition was about 300 K lower than for other molecules included in the study. Beyond these initial

experiments of this reactive molecule, it appears no additional pyrolysis or combustion studies have been performed.

More recently, electronic structure calculations predict that 2-methoxyfuran has an unusually weak $O-CH_3$ bond, about 190 kJ mol^{-1}, which is about 200 kJ mol^{-1} weaker than the $C-H$ bonds in 2-methoxyfuran and is in fact one of the weakest known $C-O$ bonds[1] [119]. This work documents a series of experiments to identify the products from the unimolecular and low-pressure bimolecular decomposition mechanisms of the simplest furanic ether, 2-methoxyfuran.

4.1   Experimental Methods

The microreactors described in Chapter 2.1 were used to study the thermal decomposition mechanism of 2-methoxyfuran. The microreactor offers a short residence time (approximately $50-200$ μs) coupled with the sensitive diagnostics of photoionization time-of-flight mass spectrometry (PIMS) and matrix isolation infrared absorption spectroscopy. The short residence time allows for rapid heating and identification of the first pyrolysis products, eliminating most, if not all, secondary reactions. Since the only previous pyrolysis experiments of methoxyfuran [23] were recorded at long reaction time scales, no detection of the organic radicals or other reactive intermediates were possible; the use of the μtubular reactor in the present study will enable identification of these elementary reaction steps.

4.1.1   Microreactor and Sample Preparation

The microreactor used for this study consists of a resistively heated silicon carbide (SiC) tube, $2.5-3.8$ cm in length, $0.66-1$ mm i.d. and 2 mm o.d. A more detailed description of the reactor assembly is included in Chapter 2.1 and also in [138, 158]. Due to the reactive nature of the molecule being studied the temperature range was limited to $300-1300$ K. The heated length is about half to two-thirds the full length of the reactor, with the temperature

---

[1] ex. DH$_{298}$(CH$_3$O$-$CH$_3$) = 349 $\pm$ 3 kJ mol^{-1} and DH$_{298}$(C$_6$H$_5$O$-$CH$_3$) = 258 $\pm$ 1.3 kJ mol^{-1}

of the outer wall measured by a tungsten/rhenium Type C or a chromel-alumel Type K thermocouple. The flow through the reactor is either controlled with a pulsed valve (Parker General Valve, series 9) or a commercial mass flow controller (MKS P4B 0-200 sccm N_2).

Dissolved water was removed from the methoxyfuran sample (Aldrich, $\geq 97\%$) with $MgSO_4$ and the dried sample was degassed using the freeze-pump-thaw method prior to preparing gaseous mixtures in helium or argon. The reactant mixtures for the pulsed experiments range from $0.03\%-0.1\%$ in He or Ar carrier gas. The total backing pressure to the pulsed valve is about 1500 Torr for He PIMS and 800 Torr for experiments in Ar. The pressure at the reactor exit for both experiments is maintained at approximately $1-10$ μTorr.

The reactant mixtures prepared for the experiments in a continuous flow reactor are between $0.0025-0.01\%$ methoxyfuran in helium, about an order of magnitude lower than those for pulsed experiments, due to a longer residence time in this style reactor. As discussed in Chapter 2.1 the residence time is essentially a fixed experimental parameter due to limited pumping capabilities so the task of eliminating secondary chemistry is accomplished through dilution. The product distributions may differ slightly between the different carrier gases and flow conditions because of variations in the pressure/temperature time-history; however, the products themselves remain consistent. The inlet pressure to the continuous flow reactor varies linearly depending on the operating temperature of the reactor. The inlet pressure to a 300 K reactor is about 100 Torr and increases linearly to 200 Torr with a reactor temperature of 1200 K.

4.1.2 Photoionization Time-of-Flight Mass Spectrometry

There are two types of photoionization mass spectrometry (PIMS) experiments reported here. One set of experiments was operated with pulsed flow through a heated SiC reactor and pyrolysis products ionized by fixed wavelength 118.2 nm (10.487 eV) vacuum ultraviolet (VUV). Another set of PIMS spectra were collected at the Chemical Dynamics Beamline (9.0.2) at Lawrence Berkeley National Laboratory's Advanced Light Source (ALS) using a

reactor operated with continuous flow and pyrolysis products ionized by tunable VUV in the range of 7.85 to 15.5 eV.

Pyrolysis products approximately 18 cm downstream from the exit of the pulsed reactor are ionized by 118.2 nm (10.487 eV) photons produced by the 9th harmonic of an Nd:YAG laser (Spectra Physics) and identified by reflectron time-of-flight mass spectrometry (Jordan). The ions are detected with a microchannel plate and the spectra collected with a digital oscilloscope, averaging 1000 scans per spectra. A more detailed description of the PIMS experiment is provided in Chapter 2.2 and [138].

The molecular beam exiting the continuous flow reactor at the ALS is interrogated by synchrotron radiation about 12 cm downstream from the skimmer. The ions were detected using a microchannel plate and the signal recorded by ion counting. Most experiments collected 100,000 to 500,000 individual mass spectra at each photon energy. Photoionization efficiency (PIE) curves for a given mass were obtained by plotting the summation of the background corrected ion signal in an appropriate mass range versus the selected photon energy, normalized by the photon flux measured by a photodiode with a calibrated energy-dependent efficiency. The on-site photodiode measurements collected for this study were unreliable so instead the PIE curves reported in this chapter were corrected using photodiode measurements from a set of experiments on the same beamline recorded about a month prior. In addition, a thicker Type-K thermocouple (Omega, chromel-alumel, diameter 0.01 in) was used for one set of continuous flow experiments at the ALS. The potential impacts of these measurements are addressed in the text.

4.1.3 Matrix Isolation Infrared Absorption Spectroscopy

As a complement to the PIMS, infrared spectroscopy in an argon matrix provides structural information for the pyrolysis products, differentiating thermal products of identical mass. The molecular beam formed at the reactor exit is aimed at a cold infrared transparent window and the products, now trapped in frozen argon, are detected by FT-IR spectroscopy.

A two-stage closed-cycle helium cryostat (APD Cryogenics, 60 Hz and 2.5 W cooling capacity at 20 K) cools a CsI window to 10 K. Reactant mixtures were prepared in a glass 1.2 L reservoir upstream of the reactor in concentrations of $0.04-0.1\%$ 2-methoxyfuran in Ar. Typical deposition rates through the pulsed valve operated at 20 Hz were 0.8 to 1 Torr min^{-1} from the reservoir (equivalent to $3-3.6$ mmol hr^{-1}), depositing between 3 to 6.5 mmol total onto the cold window. A slow deposition rate is critical to achieve resolved IR spectra. The vibrational spectra were measured using a Nicolet 6700 infrared spectrometer equipped with a liquid N_2 cooled mercury/cadmium/telluride detector (MCT/A, $4,000-650$ cm^{-1}). A background scan was taken approximately 1 to 2 hours prior to the sample scan; all spectra averaged 500 scans at 0.25 cm^{-1} resolution.

4.2 Unimolecular Decomposition Mechanism

Recent CBS-QB3 electronic structure calculations [119] suggest that 2-methoxyfuran has an unusually weak $O-CH_3$ bond, about 190 kJ mol^{-1}, and predict the dominant pathway for thermal decomposition is loss of CH_3 to produce the allylic lactone 2-furanyloxy radical (γ-butryolactonyl radical, m/z 83) as shown in Scheme 4.2. The structure and thermochemical properties of 2-methoxyfuran and the radicals formed by loss of hydrogen atoms have also been examined computationally by Hudzik *et al.* [56].
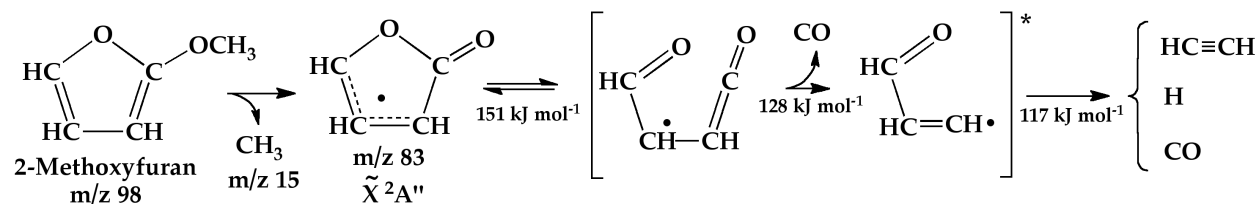
Scheme 4.2: Primary unimolecular decomposition pathway of 2-methoxyfuran, including the lowest calculated reaction barriers [119]

To date there is no experimental evidence for 2-furanyloxy radical, however the structure and stability of this allylic lactone have been discussed in several computational studies. The

2-furanyloxy radical is predicted to be an intermediate in the oxidation of 2-furanyl radical [6] and also a minor, high-energy channel intermediate in the oxidation of phenyl radical [127]. Prior to these studies, Yamamoto *et al.* [155] calculated the cyclization of the open-chain radical dione (4-oxo-but-3-enal-2-yl) in Scheme 4.2 to 2-furanyloxy.

This work includes the first experimental characterization of 2-furanyloxy radical by assignment of several intense infrared vibrational bands in an Ar matrix and a low-resolution estimate of the ion energetics of this molecule, including the ionization threshold, photoionization efficiency curve and an estimate of the photoionization cross-section at 10.0 eV. These assignments are supported by calculations of the harmonic vibrational frequencies and ion properties from Simmie *et al.* [119, 133].

As depicted in Scheme 4.2, the furanyloxy radical is predicted [119] to ring open *via* a β-scission of the ring O1−C2 bond to the dione radical 4-oxo-but-3-enal-2-yl (refer to Scheme 4.1 for the numbering system used throughout). From here, the dione intermediate can eliminate CO to give a formyl vinyl radical, prop-1-ene-1-yl-3-one. The fate of the formyl vinyl radical, shown in Scheme 4.3, is either a β-scission to acetylene (HC≡CH) and formyl radical (HCO) or a 1,3-H-shift to acryloyl (1-oxo-2-propen-1-yl or O=C-CH=CH$_2$). The acryloyl radical will then dissociate to CO and vinyl radical (CH$_2$=CH) [72, 133]. Both decomposition pathways will result in formation of two molecules of CO, one H-atom, and one HC≡CH from the ring opening of the furanyloxy radical intermediate.
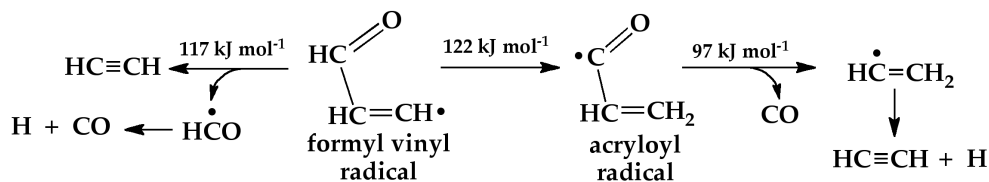
Scheme 4.3: Fate of formyl vinyl radical, m/z 55, including reaction barriers [119]

The unimolecular decomposition products of 2-methoxyfuran in helium detected by 118.2 nm (10.487 eV) photoionization mass spectrometry (PIMS) are shown in Fig. 4.1. With
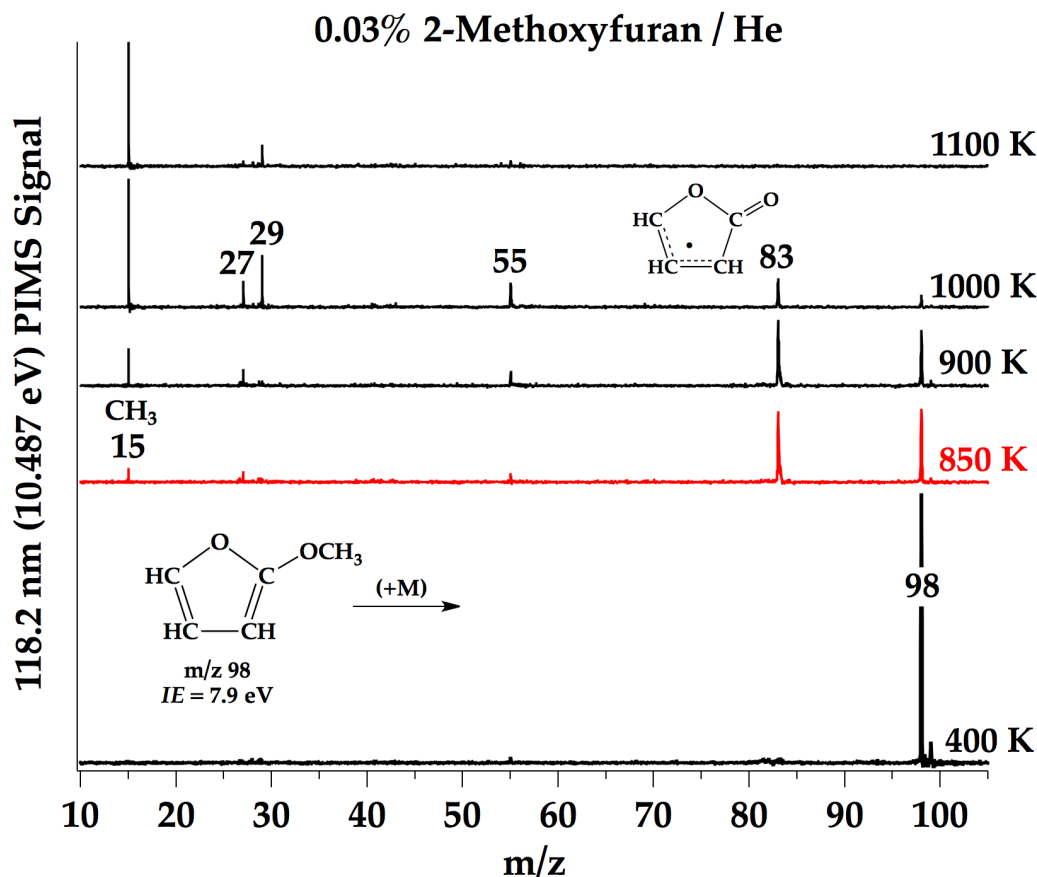
Figure 4.1: Mass spectra identify the unimolecular products from the pyrolysis of 2-methoxyfuran in helium in a pulsed flow heated SiC reactor. Products are ionized with 118.2 nm VUV photons (10.487 eV); temperatures indicated are the measured reactor wall temperature.

the SiC reactor held at 400 K, only the parent ion and the ^{13}C isotope are observed at m/z 98 and 99, respectively. Heating the reactor to 850 K triggers thermal decomposition and the observed ions are assigned as CH_3^+ (m/z 15), $C_2H_3^+$ (m/z 27), HCO^+ (m/z 29), $C_3H_3O^+$ (m/z 55), and 2-furanyloxy radical (m/z 83). However, as will be described later, only m/z 15 and 83 are assigned as thermal products; the ions observed at 27, 29 and 55 are assigned to dissociative ionization of either the parent or 2-furanyloxy. By 1100 K, all 2-methoxyfuran (m/z 98) is consumed.

Since ionization energies of carbon monoxide [38] and acetylene [10] are beyond the range of the laser at 10.487 eV (see Table 4.1), the presence of acetylene from pyrolysis

of a 0.04% mixture of 2-methoxyfuran in argon is demonstrated by detection of the IR fundamentals $\nu_3(\mathrm{HC{\equiv}CH})$ at 3287 cm^{-1} and its associated Darling-Dennison resonance at 3301 cm^{-1} in an Ar matrix, as shown in Fig. 4.2. In addition $\nu_5(\mathrm{HC{\equiv}CH})$ at 737 cm^{-1} and an absorbance feature associated with an interaction between HCCH and N$_2$ in an Ar matrix [61] appears when compared to a scan of 0.1% methoxyfuran in Ar deposited through a reactor held at 300 K. Carbon monoxide is difficult to detect because there is always a small background when the SiC reactor is heated (due to reaction with trace amounts of O$_2$), however the the main absorption at 2139 cm^{-1} and growth of ^{13}CO isotope at 2091 cm^{-1} are detected [1]; these spectra are included in Fig. C.1 of Appendix C.
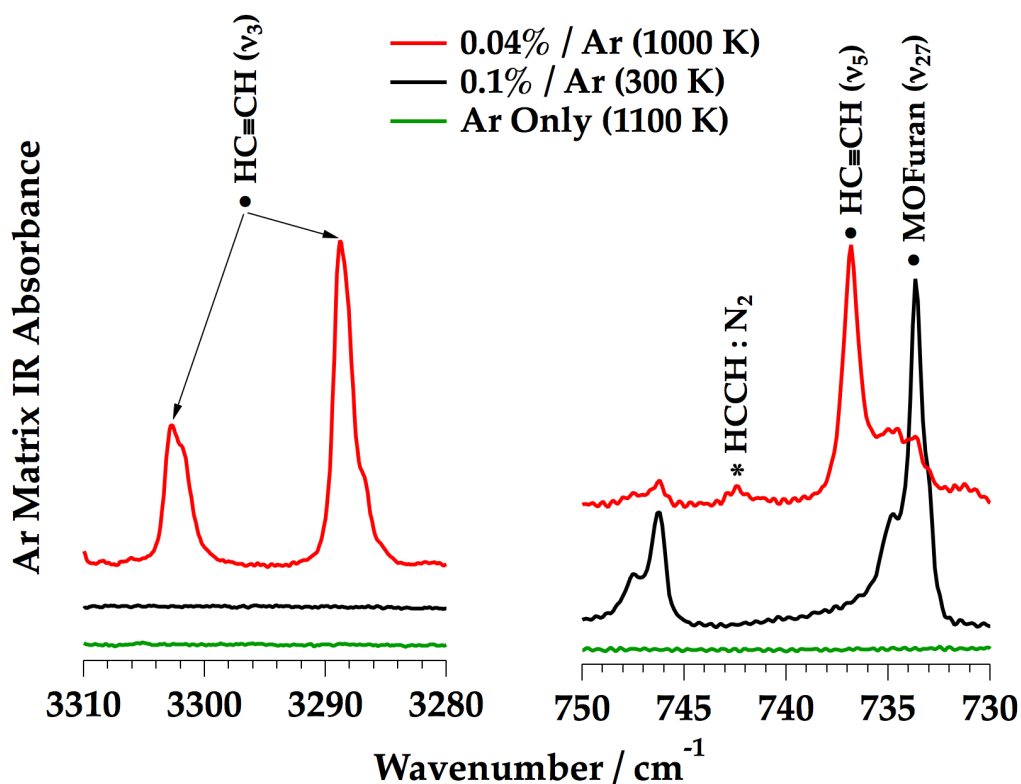
Figure 4.2: Infrared spectra identify acetylene (ν_3, ν_5) in Ar as a pyrolysis product of 2-methoxyfuran. Shown for comparison are reference scans with only argon passed through an 1100 K SiC reactor and the reactant mixture through a 300 K reactor.

The mass spectra in Fig. 4.3 show the major pyrolysis products from a 0.01% mixture of 2-methoxyfuran in helium through a continuous flow reactor at LBNL's Advanced Light
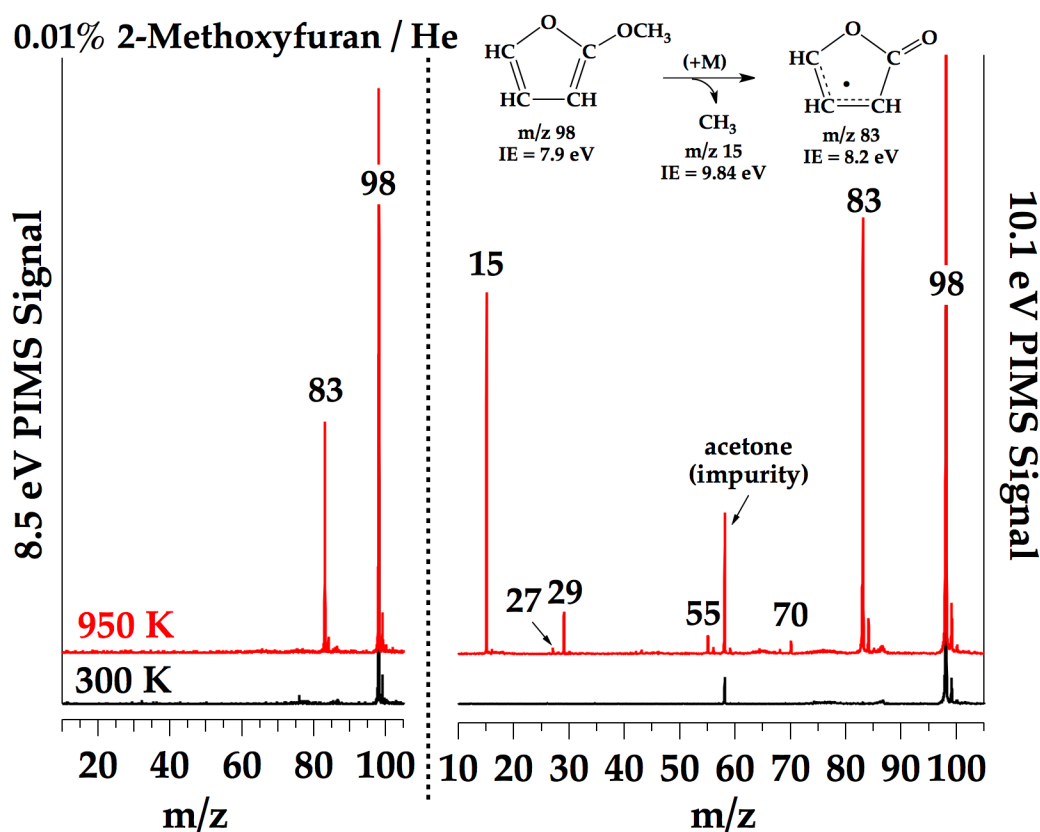
Figure 4.3: Dual photon energy mass spectra from experiments in a continuous flow reactor distinguish ions resulting from dissociative ionization from those formed thermally. Mass spectra at 950 K sampled 500,000; 300 K sampled 100,000 scans.

Source (ALS). The ionization energy of 2-methoxyfuran has not been measured experimentally, but *ab initio* electronic structure calculations predict the ionization energies of the *cis* and *trans* conformers to be 7.93 eV and 7.79 eV, respectively [133] (the lowest energy conformer of 2-methoxyfuran is the methyl group *cis* to the carbon-carbon double bond in the ring [9, 56]). Likewise the IE(2-furanyloxy radical, m/z 83) is calculated to be 8.23 eV [133]. A summary of important measured or calculated ionization energies is shown in Table 4.1.

The left-hand panel of Fig. 4.3 demonstrates that pyrolysis of 2-methoxyfuran at 950 K generates m/z 83 when 8.5 eV is used to photoionize. If the energy of the VUV is increased to 10.1 eV (right-hand panel), the CH_3 radical (m/z 15) is detected and new ions appear at m/z 27, 29, 55, and 70 (the feature at m/z 58 is not a thermal product but instead is an

Table 4.1: Chemical formulas, common names and mass of species referred to in the kinetic mechanism and throughout the text. Also included are the measured or calculated ionization potentials.

m/z	Formula	Species	IE (eV)	Ref.
1	H	hydrogen atom	13.59844 ± 0.00001	[76]
15	CH_3	methyl radical	9.8380 ± 0.0004	[17]
16	CH_4	methane	12.618 ± 0.004	[117]
26	$HC{\equiv}CH$	acetylene	11.40081 ± 0.0001	[101]
27	$CH_2{=}CH$	vinyl radical	8.468 ± 0.029	[73]
28	CO	carbon monoxide	14.0136 ± 0.0005	[38]
29	HCO	formyl radical	8.15022 ± 0.00006	[85]
30	$CH_2{=}O$	formaldehyde	10.8850 ± 0.0002	[114]
55	$CH{=}CH\text{-}CHO$	formyl vinyl radical	8.51	[133]
55	$O{=}C\text{-}CH{=}CH_2$	acryloyl radical	6.93 (*trans*)	[133]
56	$CH_2{=}CH\text{-}CHO$	acrolein	10.11 ± 0.01	[84, 135]
68	C_4H_4O	furan	8.88 ± 0.01	[144]
68	$CH_2{=}CH\text{-}CH{=}C{=}O$	vinylketene	8.45	[87]
70	$CH_3\text{-}CH{=}CH\text{-}CHO$	crotonaldehyde	9.73 ± 0.01	[135, 142]
70	$CH_3\text{-}CO\text{-}CH{=}CH_2$	methyl vinyl ketone	9.65 ± 0.02	[91, 124]
70	$CH_2{=}C(CH_3)\text{-}CHO$	methacrolein	9.92	[84]
83	$C_4H_3O_2$	2-furanyloxy radical	8.23	[133]
83	$O{=}C{=}CH\text{-}CH\text{-}CHO$	4-oxo-but-3-enal-2-yl*	7.79 (*trans-cis*)	[133]
			7.66 (*cis-trans*)	
			7.70 (*trans-trans*)	
84	$C_4H_4O_2$	2(3H)-furanone	9.31	[150]
			9.67	[140]
84	$C_4H_4O_2$	2(5H)-furanone	10.22	[150]
			10.65 ± 0.1	[159]
96	$C_4H_3O\text{-}CHO$	furfural	9.22 ± 0.01	[63]
98	$C_4H_3O(OCH_3)$	2-methoxyfuran	7.93 (*trans*)	[133]
			7.79 (*cis*)	
98	$C_5H_6O_2$	3-methyl-2(3H)-furanone	9.17	[150]
98	$C_5H_6O_2$	5-methyl-2(5H)-furanone	10.06	[150]
			10.12 ± 0.05	[125]
98	$C_5H_6O_2$	5-methyl-2(3H)-furanone	8.91	[150]
			8.97 ± 0.05	[30]

*dihedrals O=C-C-C and CCCC

acetone impurity due to an inadequate purge with He after cleaning between experiments at the ALS). We believe that the ions $C_2H_3^+$ (m/z 27), HCO^+ (m/z 29) and $C_3H_3O^+$ (m/z 55) result from dissociative ionization of either 2-furanyloxy radical (m/z 83) or a vibrationally
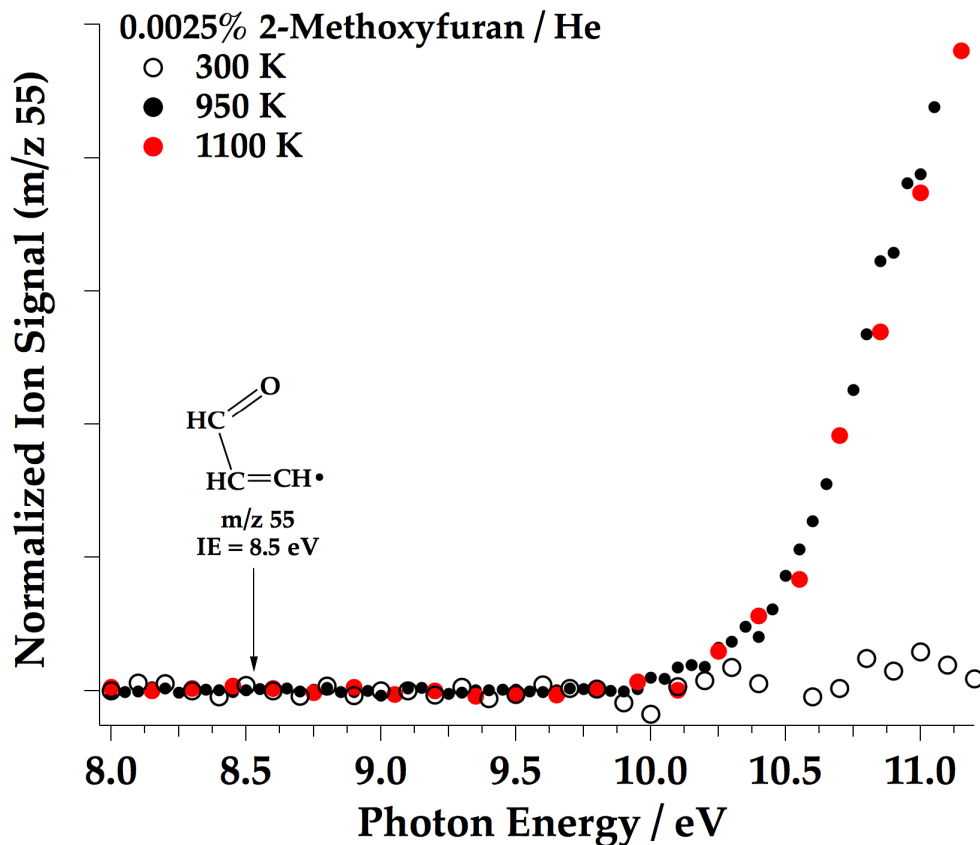
Figure 4.4: Photoionization efficiency curves of m/z 55 observed at several reactor temperatures. The lifetime of the proposed formyl vinyl radical intermediate (IE = 8.51 eV [133]) is too short to be observed at the reactor exit; instead only signals due to dissociative ionization of other species are observed above 10 eV.

excited methoxyfuran. None of these ions appear in the 10.1 eV PIMS of 2-methoxyfuran at 300 K and indeed, if they were thermal products, both m/z 29 and 55 should be observed in the PIMS at 8.5 eV. The ion at m/z 70 is a secondary pyrolysis product of 2-methoxyfuran and its origin will be discussed in Sections 4.3.1 and 4.3.2.

A set of photoionization efficiency (PIE) curves at m/z 55 are shown in Fig. 4.4. No ion signal at mass 55 is observed until above 10 eV at elevated temperatures, indicating the formyl vinyl or acryloyl radicals shown in Scheme 4.3 are not stable intermediates and their lifetimes are too short to be detected under the conditions in the reactor. Based on their predicted ionization energies shown in Table 4.1, if they were stable at the reactor exit they
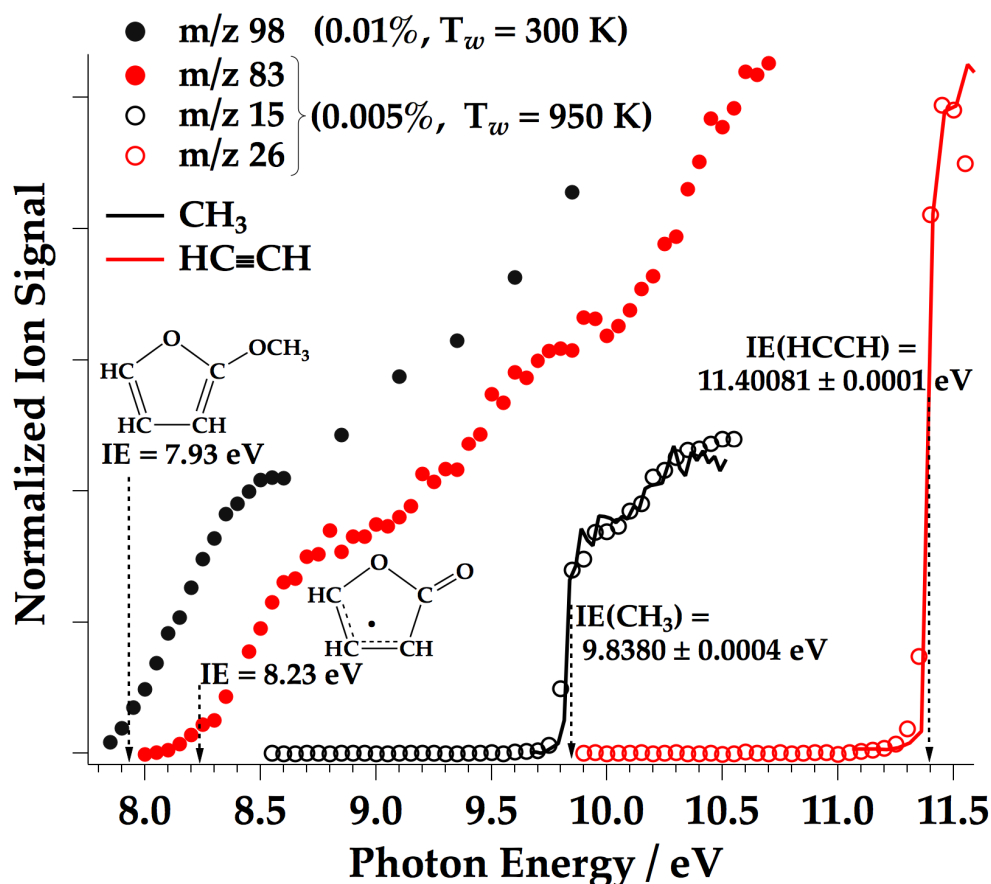
Figure 4.5: PIE curves and ionization energies [17, 101, 133] of 2-methoxyfuran (m/z 98) and the primary unimolecular products 2-furanyloxy radical (m/z 83), methyl radical (m/z 15) and acetylene (m/z 26). Shown for comparison as solid lines are the absolute photoionization cross-sections of CH_3 [123] and HCCH [29].

should ionize well below 10 eV.

Figure 4.5 includes a set of PIE curves that identify the primary unimolecular products in the thermal decomposition of 2-methoxyfuran as furanyloxy radical (m/z 83), CH_3 radical (m/z 15), and HC≡CH (m/z 26); ions from carbon monoxide also appears at 14 eV but are not included in this plot. The measured absolute photoionization cross-sections of methyl radical [123] and acetylene [29], plotted as solid lines, are shown for comparison. The observed ionization thresholds of PIE(m/z 83) and PIE(m/z 98) are consistent with the calculated values of 8.23 eV and 7.79/7.93 eV for 2-furanyloxy radical and 2-methoxyfuran, respectively [133]. The ion signal at m/z 83 begins to grow in at 8.1 eV, although 0.1 eV

lower than predicted [133], it is about 0.4 eV above the predicted ionization threshold for any of the radical dione, O=C=CH-CH-CHO, conformations (see Table 4.1). This evidence also suggests that the lifetime of the intermediate formed by ring-opening of furanyloxy is too short to be detected at the conditions in the microreactor.
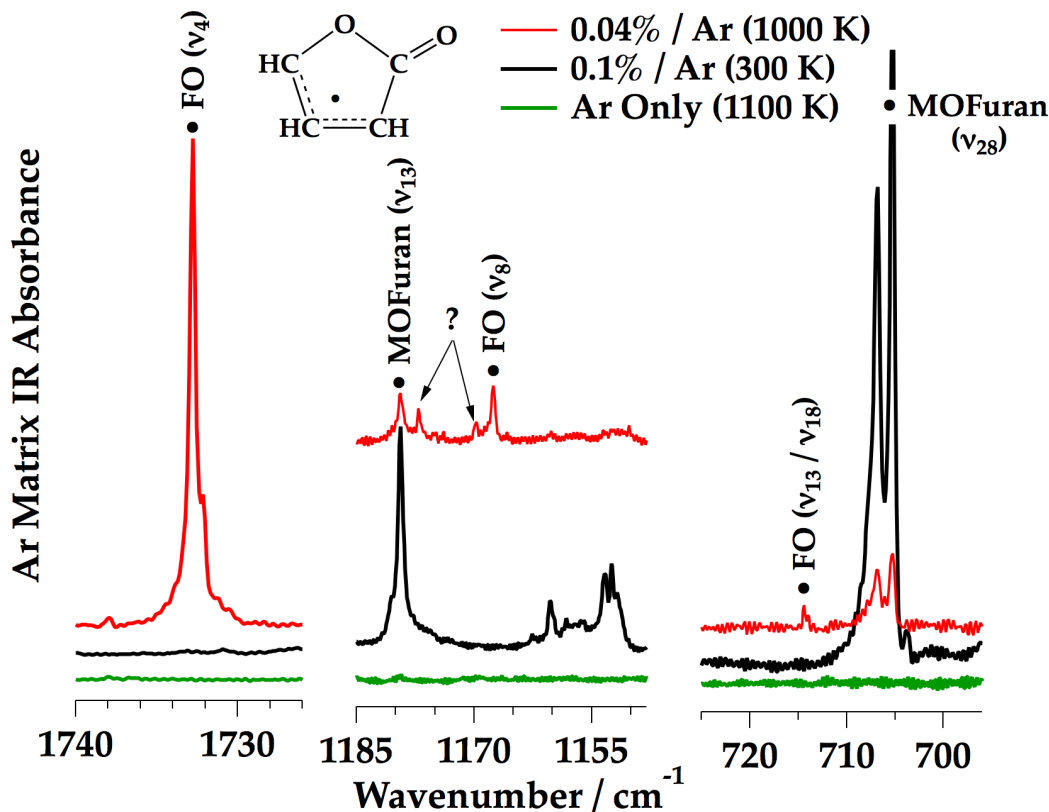
Figure 4.6: Select vibrational assignments of 2-furanyloxy radical in an Ar matrix compared to scans of only Ar through a heated reactor and methoxyfuran in Ar through a room temperature reactor. Intense feature at 705 cm^{-1} is ν_{28} of 2-methoxyfuran; features marked (?) are tentatively assigned to ν_8 of 2-furanyloxy.

The presence of 2-furanyloxy radical as a stable intermediate was also identified by IR spectroscopy in an Ar matrix, as shown in Fig. 4.6. From the electronic structure calculations [119], the intense feature at 1732.8 cm^{-1} is assigned as ν_4(C=O stretch of 2-furanyloxy radical). The location of the carbonyl sretch is consistent given the structure of this allylic lactone. The C−O bond in furanyloxy has been calculated to be shorter than a typical C−O single bond and closer to a typical C=O bond [6, 119]. Other vibrational

assignments in Fig. 4.6 include ν_8, ν_{13}, and ν_{18} of this allylic lactone. There are also features at 1709 cm^{-1} and 1749 cm^{-1} (see Fig. 4.9 on page 66) that are also tentatively assigned to ν_4 of 2-furanyloxy. An IR study of 2(5H)-furanone in an Ar matrix [19] reports that the carbonyl stretch is very anharmonic, exhibiting several satellite peaks in the IR, possibly due to Fermi-resonance type bands. Since the furanyloxy radical has a very similar structure to 2(5H)-furanone (see Scheme 4.4), it may behave similarly in an argon cage. The questionable features at 1169.7 cm^{-1} and 1177.1 cm^{-1} could also be satellite features of ν_8-furanyloxy or interaction bands in Ar. A full analysis of the infrared spectra and a tabulated summary of vibrational frequencies are presented in Table C.1 of Appendix C.

It should be noted that some of the bands in the IR could be associated with the radical dione (O=C=CH-CH-CHO) or the formyl vinyl (CH=CH-CHO) intermediates instead of features or fundamentals of 2-furanyloxy in an Ar matrix. However, there are no intense features in an Ar matrix to indicate that there is a ketene-type stretch for the radical dione. The calculated harmonic frequencies of this intermediate in Scheme 4.2 indicate that an intense ν_4 stretch should appear in the 2170 to 2130 cm^{-1} region in Ar. In this region of the spectrum there are only absorption features due to CO (2139 cm^{-1}) and CO-H$_2$O interaction (2149 cm^{-1}) [1] as shown in Fig. C.1 in Appendix C. Of course since it is unknown where precisely this molecule will absorb in the IR it is possible that the signal is completely masked by CO. However the lack of evidence for both of these species by examining their PIE curves at m/z 55 and 83 (Figs. 4.4 and 4.5) suggests they are not stable enough intermediates to be detected.

4.3   H/CH$_3$ Addition and Abstraction Reactions

Even though pyrolysis experiments are operated at very dilute conditions, the products resulting from reactions of the H atoms and CH$_3$ radicals produced in Scheme 4.2 with 2-methoxyfuran must also be considered. Scheme 4.2 predicts that for every molecule of 2-methoxyfuran that decomposes, one H-atom and one CH$_3$ radical are produced. Both of

these radicals are very reactive and it is possible that they might abstract a hydrogen or add to the ring of unreacted methoxyfuran [119].
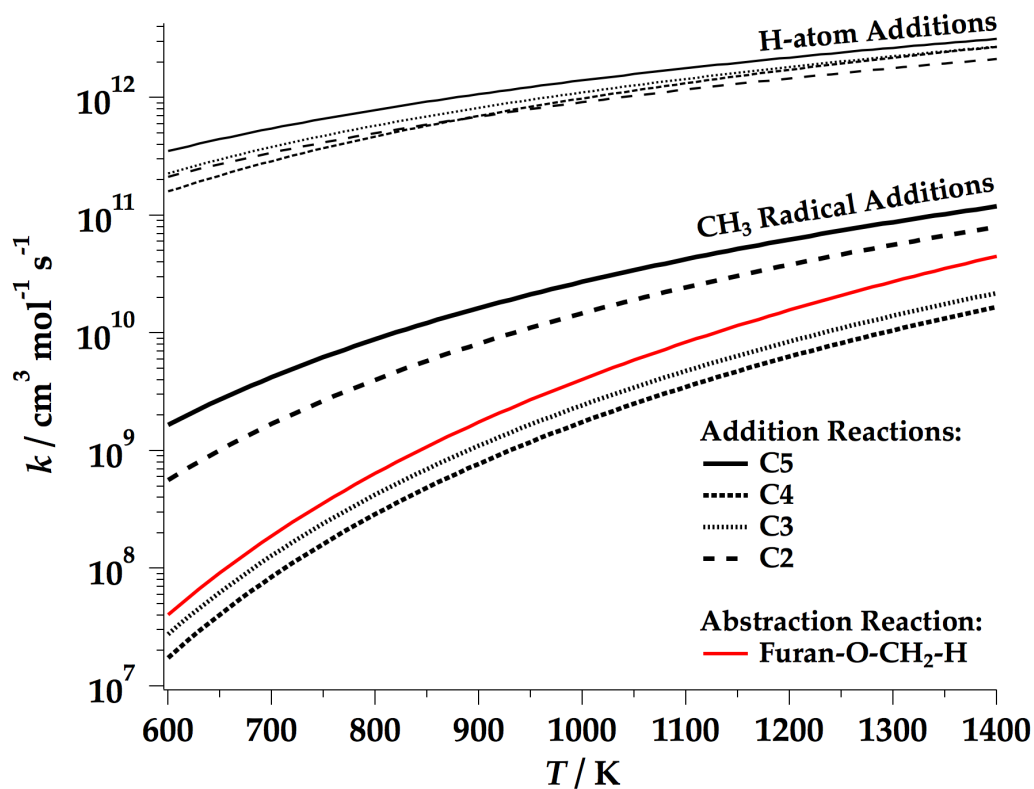
Figure 4.7: Calculated rate constants of H/CH$_3$ addition reactions to 2-methoxyfuran and hydrogen abstraction by CH$_3$ at C7 [119, 133].

Calculated [119, 133] bimolecular rate constants for addition and abstraction reactions, shown in Fig. 4.7, have been used to determine plausible bimolecular routes. The rates were calculated from 300 to 2000 K in increments of 100 or 200 K and fitted to a modified Arrhenius expression; a summary of the rate constants are also included in Table 4.2 located on page 77. A few important aspects to note about these rate constants: at 1000 K H-atom addition reactions are two orders of magnitude faster than the fastest CH$_3$ addition reaction at C5 on the methoxyfuran ring (see Scheme 4.1). Also, the rate constant for methyl addition at C3 or C4 is another order of magnitude lower than addition at C5.

As discussed for the furan dilution studies in Fig. 3.1 of Chapter 3.2, under similar

operating conditions hydrogen-atom radical addition reactions could be avoided at a dilution of 0.01% in He [131]. However when thermally cracking methoxyfuran, H-atoms and CH_3 radicals are formed at lower temperatures and at faster time scales within the reactor, so it was found that a dilution of about 0.0025% in He was required to eliminate the products resulting from secondary reactions in a reactor operated with continuous flow. As discussed in Chapter 2.1.2, the residence time in the reactor is essentially a fixed experimental parameter and decreasing the time spent in the reactor is not a viable option for reducing bimolecular reactions; instead this task must be accomplished through dilution.
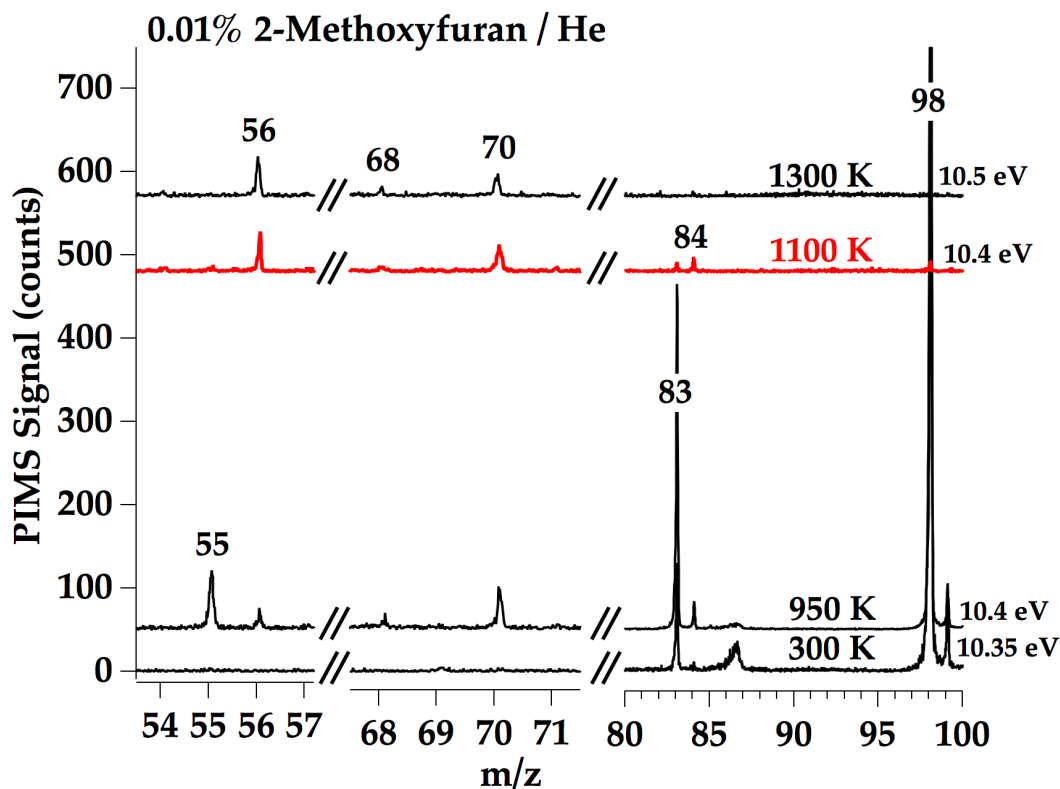
Figure 4.8: Several observed species assigned to bimolecular chemistry. Dissociative ionization of 2-methoxyfuran to m/z 83 is observed at 300 K in the 10.35 eV PIMS. The feature extending over mass 86 to 88 is also the result of dissociative ionization and an artifact of the reflectron time-of-flight operation. Scan at 950 K is scaled by 0.25 in the mass region 80 to 100. Elevated temperatures sampled 500,000 scans; 300 K sampled 100,000 scans.

In addition to the primary unimolecular products observed at 0.0025% in He, there are several species that grow in as the reactant concentration is increased. Figure 4.8 is an expanded view of the mass spectra from Fig. 4.3, including two more elevated temperatures. These spectra show that new ions at m/z 56, 68, 70 and 84 appear and persist even after all methoxyfuran has been consumed.

4.3.1   Addition Reactions

An assortment of possible products resulting from H or CH_3 additions to unreacted methoxyfuran are shown in Schemes 4.4 and 4.5, respectively. In addition to the predicted rate constants of these reactions, the combination of infrared spectroscopy and photoionization efficiency curves aid in the identification of the relevant reaction schemes.
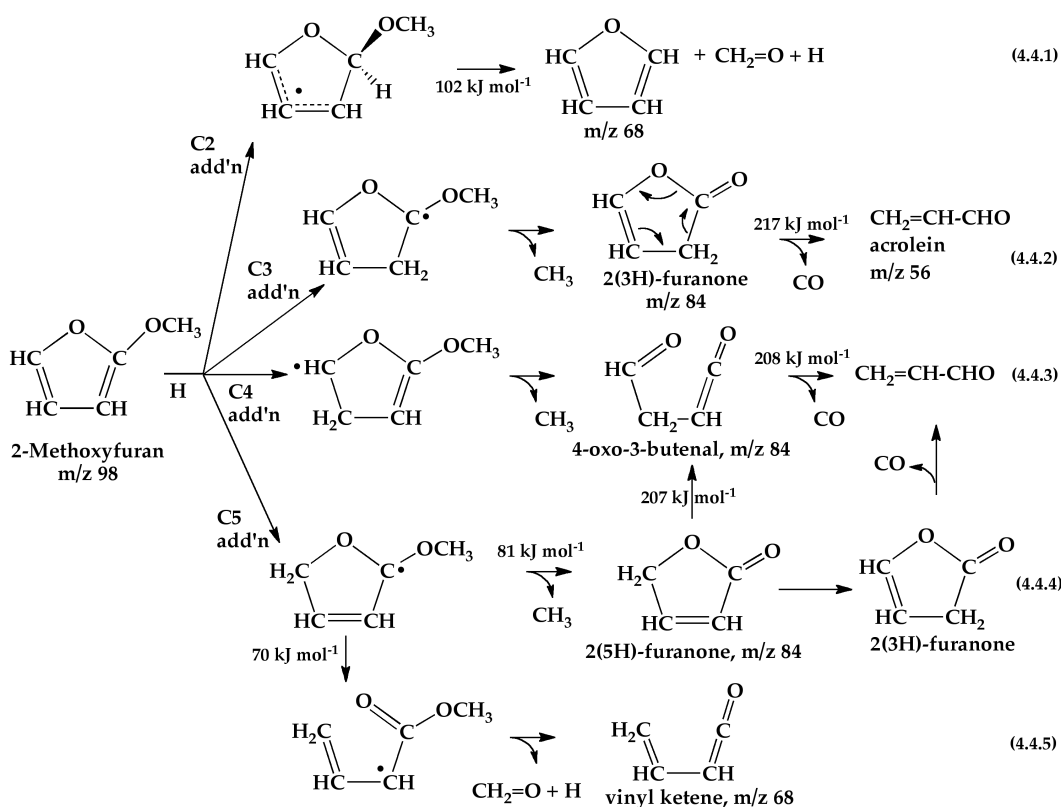
Scheme 4.4: Hydrogen-atom addition reactions to 2-methoxyfuran and possible resulting products. Barrier heights for select decomposition routes are indicated [133].
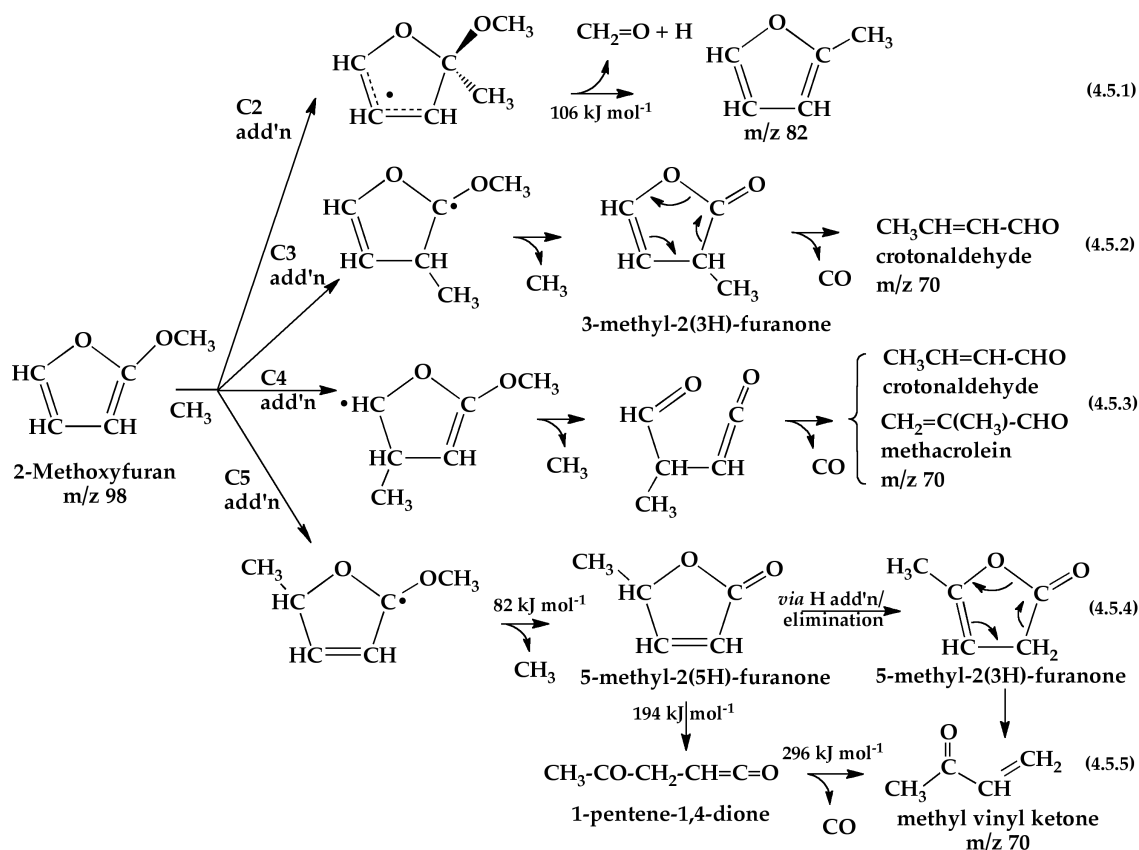
Scheme 4.5: CH_3 radical addition reactions to 2-methoxyfuran and possible resulting products. Barrier heights for select decomposition routes are indicated [133].

Figure 4.9 is a trace of the carbonyl region of the IR spectra, comparing a dilute mixture (0.04%) of methoxyfuran in Ar, thin black line, to a more concentrated mixture (0.1%), red line. Products detected from the 0.1% mixture at 1100 K include $CH_2{=}O$, methyl vinyl ketone (MVK or $CH_3CO\text{-}CH{=}CH_2$), and the unsaturated aldehydes acrolein ($CH_2{=}CH\text{-}CHO$) and crotonaldehyde ($CH_3CH{=}CH\text{-}CHO$), while only formaldehyde and acrolein are detected as secondary products for the dilute mixture at 1000 K. Figure 4.10 expands on the 1100 K spectrum in the region $1720-1695$ cm^{-1}, identifying MVK, acrolein and crotonaldehyde by comparison to authentic samples in an Ar matrix. The reactor was heated during part of the acrolein/Ar deposition in order to induce isomerization to the less thermodynamically stable *cis* conformation (similar to the approach used by Blom *et al.* [16]). The growth of split peaks
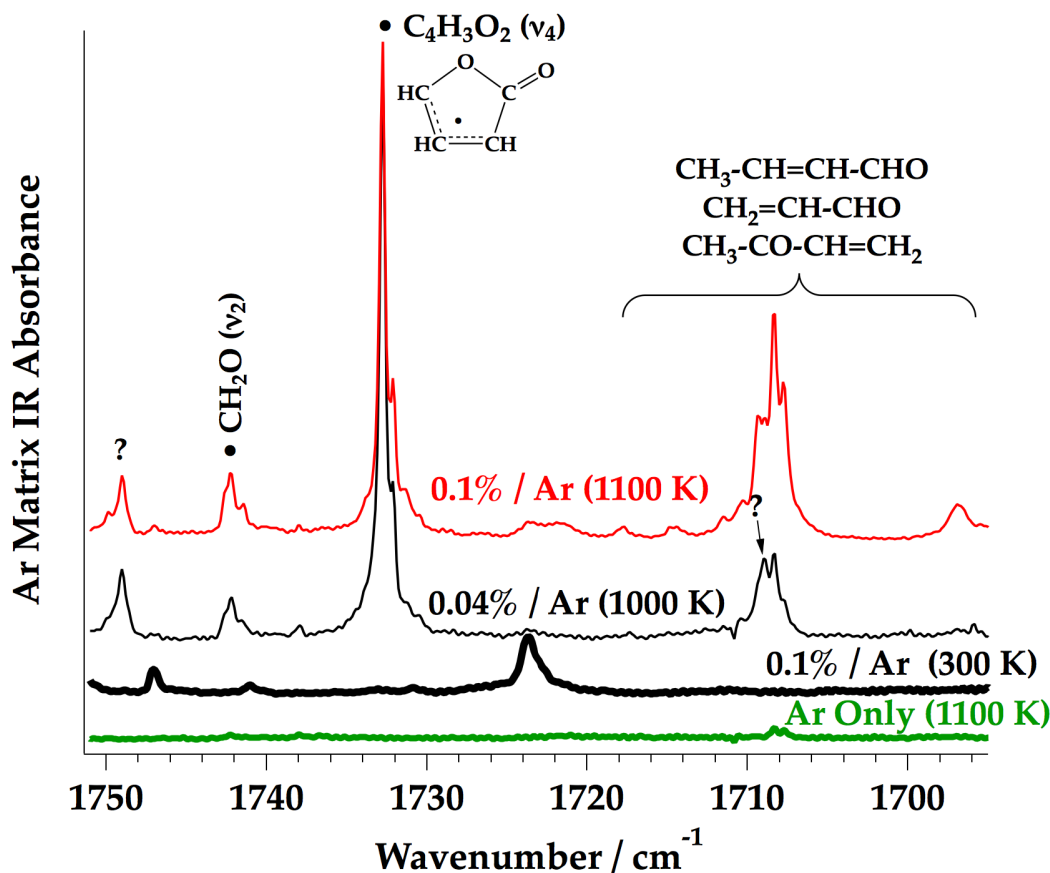
Figure 4.9: FT-IR product spectra of the carbonyl region for a concentrated mixture of methoxyfuran in Ar compared to a dilute mixture. Shown for comparison are scans of only Ar through a heated reactor and methoxyfuran in Ar through a room temperature reactor. Uncertain bands (?) at 1749 and 1709 cm^{-1} could belong to 2-furanyloxy (ν_4).

at 1714.3 and 1714.9 cm^{-1} are assigned to *cis*-CH$_2$=CH-CHO [60], while *trans*-CH$_2$=CH-CHO absorbs at 1708.3 and 1707.8 cm^{-1}. The lone unlabeled feature in Fig. 4.10 at 1709 cm^{-1} is likely the satellite peak of the furanyloxy radical (ν_4), as it is present in both the dilute and more concentrated product spectra. A tabulated summary of vibrational frequencies is presented in Tables C.1 through C.3 of Appendix C.

When compared to the concentrated mixture in Fig. 4.9, the only species detected in the dilute mixture are *trans*-CH$_2$=CH-CHO and CH$_2$=O. Both of these species can result from H-atom addition reactions to the ring, as shown in Schemes 4.4.1 and 4.4.5 for formaldehyde and Schemes 4.4.2 through 4.4.4 for acrolein. As shown in the PIMS spectra in Fig. 4.8, a trace
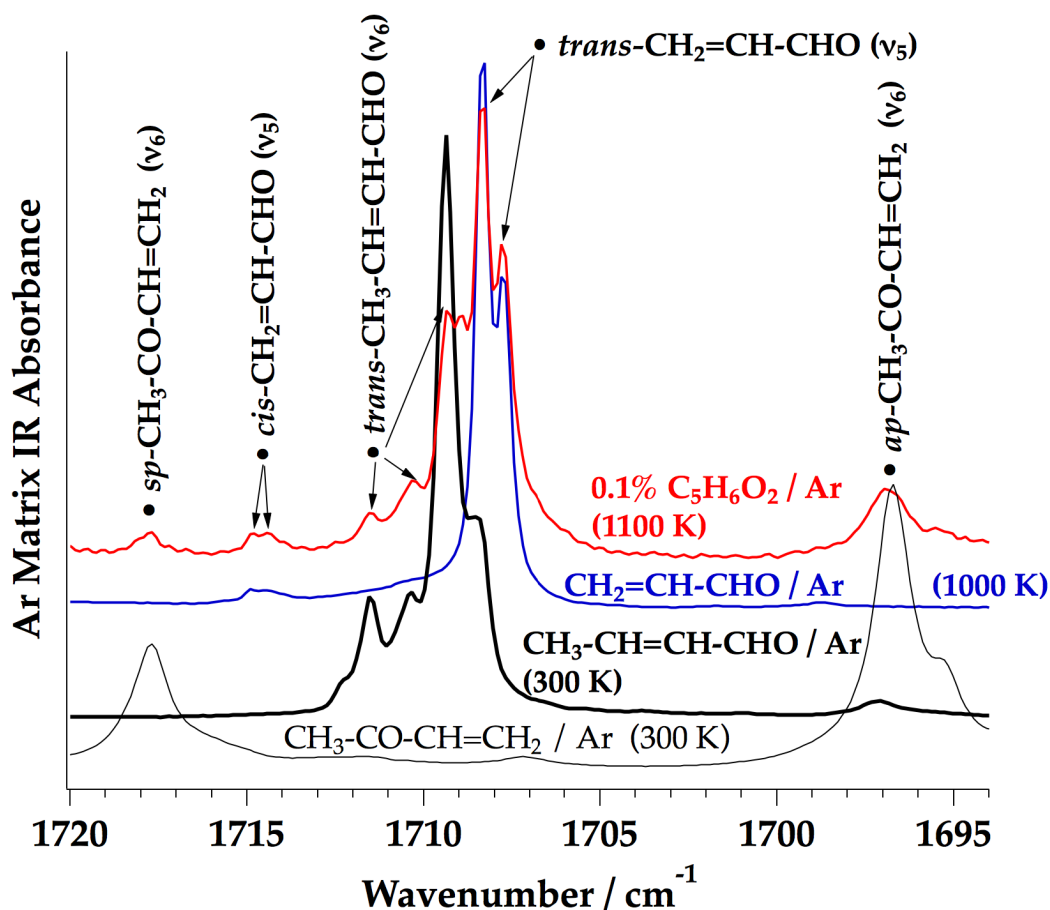
Figure 4.10: Authentic FT-IR spectra of acrolein, crotonaldehyde and methyl vinyl ketone in an Ar matrix, compared to product spectrum of a 0.1% mixture of methoxyfuran in argon heated to 1100 K (6.4 mmol deposited). Each authentic spectrum scaled relative to product spectrum as indicated; molecule(%-mixture/Ar, mmol Ar deposited, scaling factor): CH_3-CO-CH=CH_2 (0.09%, 6.4, 1:30); CH_3-CH=CH-CHO (0.06%, 4.0, 1:13); CH_2=CH-CHO (0.05%, 5.8, 1:13).

of m/z 68 is also observed. There are two possible identities for m/z 68 in Scheme 4.4: either H-atom addition to C2 (Scheme 4.4.1) to produce furan, or ring-opening of the C5 radical addition intermediate in Scheme 4.4.5, eliminating methoxy radical, to give vinylketene. The ion signal is observed to grow in near the ionization threshold of furan (IE = 8.88 eV) [144] but the signal is barely above the noise level. This indicates that formation of m/z 68 by hydrogen atom addition reactions in Schemes 4.4.1 and 4.4.5 are less likely than formation of acrolein, which could result from H-addition at all other positions.

Photoionization efficiency scans further confirm the presence of acrolein and croton-aldehyde at 950 K, 1100 K, and 1300 K for different reactant mixture concentrations in a continuous flow of helium. Figure 4.11 demonstrates that the ion signal begins to grow in at 10.1 eV, the ionization threshold of acrolein [84, 135] and the PIE(m/z 56) curve closely resembles the known photoionization cross-section for CH_2=CH-CHO [46].
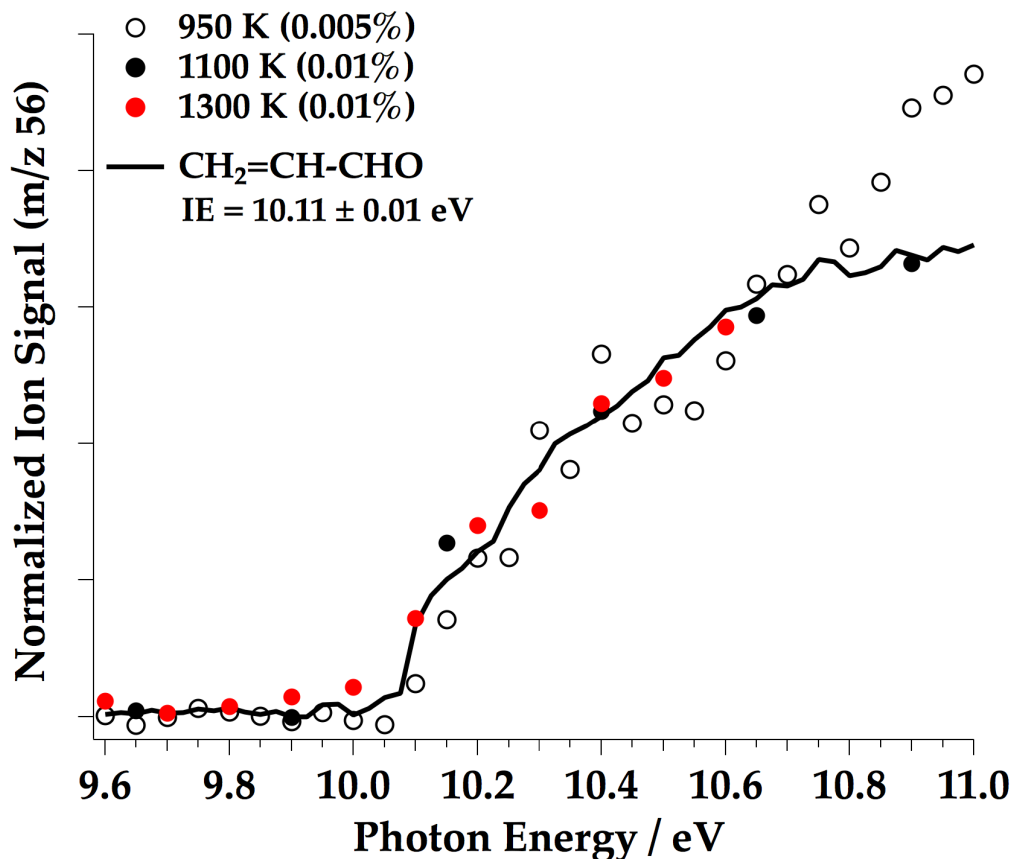
Figure 4.11: Photoionization efficiency curves of m/z 56. Absolute photoionization cross-section and ionization potential of acrolein (CH_2=CH-CHO) are included [46, 84, 135].

PIE curves also indicate the presence of crotonaldehyde as a thermal product. Figure 4.12 shows the PIE(m/z 70) curves that result from pyrolysis of 2-methoxyfuran in helium through a reactor with continuous flow. The solid lines are the measured photoionization cross-sections of methyl vinyl ketone, crotonaldehyde and methacrolein, possible product species with a mass of 70 amu. The PIE(m/z 70) curve appears to most closely resemble

the CH$_3$-CH=CH-CHO cross-section curve. Crotonaldehyde ionizes at 9.73 eV [135, 142] and the IE(methyl vinyl ketone) and IE(methacrolein) are 9.65 eV [91, 124] and 9.92 eV [84], respectively. The PIE(m/z 70) trace rises at about 9.75 eV and follows the general trend of the crotonaldehyde curve. However, based on the shape of this curve we cannot rule out trace amounts of methyl vinyl ketone or methacrolein; the earlier rise in photon energy of the data points at 1100 K and 1300 K indicate there could be trace amounts of MVK in the molecular beam. The infrared product spectra are consistent with this conclusion: the dominant secondary product at m/z 70 is crotonaldehyde but with trace amounts of methyl vinyl ketone.
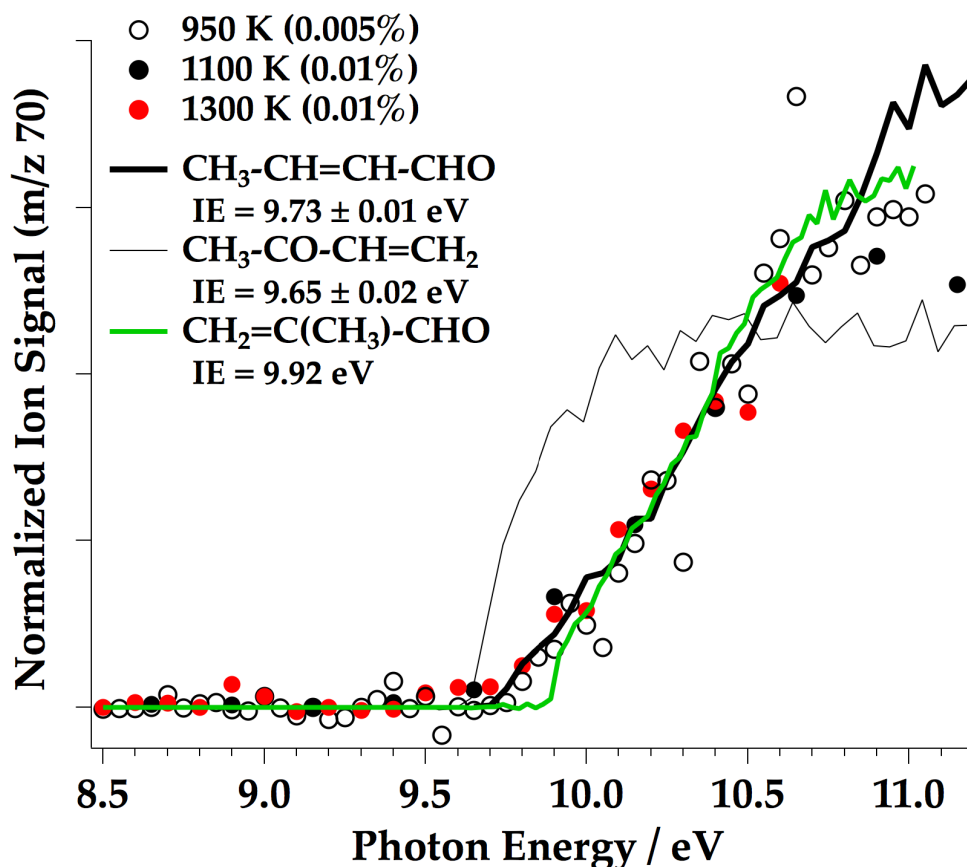
Figure 4.12: Photoionization efficiency curves of m/z 70. Absolute photoionization cross-sections and measured ionization potentials are included: CH$_3$-CH=CH-CHO [135, 142, 156], CH$_3$-CO-CH=CH$_2$ [91, 124, 156] and CH$_2$=C(CH$_3$)-CHO [45, 84].

A scan of PIE(m/z 84) is unable to definitively identify which species in Scheme 4.4 are intermediates of hydrogen atom addition reactions due to interfering signals of the ^{13}C isotope from mass 83. A PIE(m/z 84) scan at 1300 K when all m/z 83 is consumed does show that trace amounts of m/z 84 grow in between $9.5-10$ eV, which could indicate the possibility of both 2(3H)-furanone (IE $= 9.3-9.7$ eV) [140, 150] and 2(5H)-furanone (IE $= 10.2-10.65$ eV) [140, 150]. The experimentally reported ionization energy [140] of 2(5H)-furanone of 10.65 eV is likely too high; samples of 2(5H)-furanone seeded in He were pyrolyzed in the SiC microreactor and ions were observed with photons at 10.487 eV. For more details of these experimental results refer to Chapter 5.
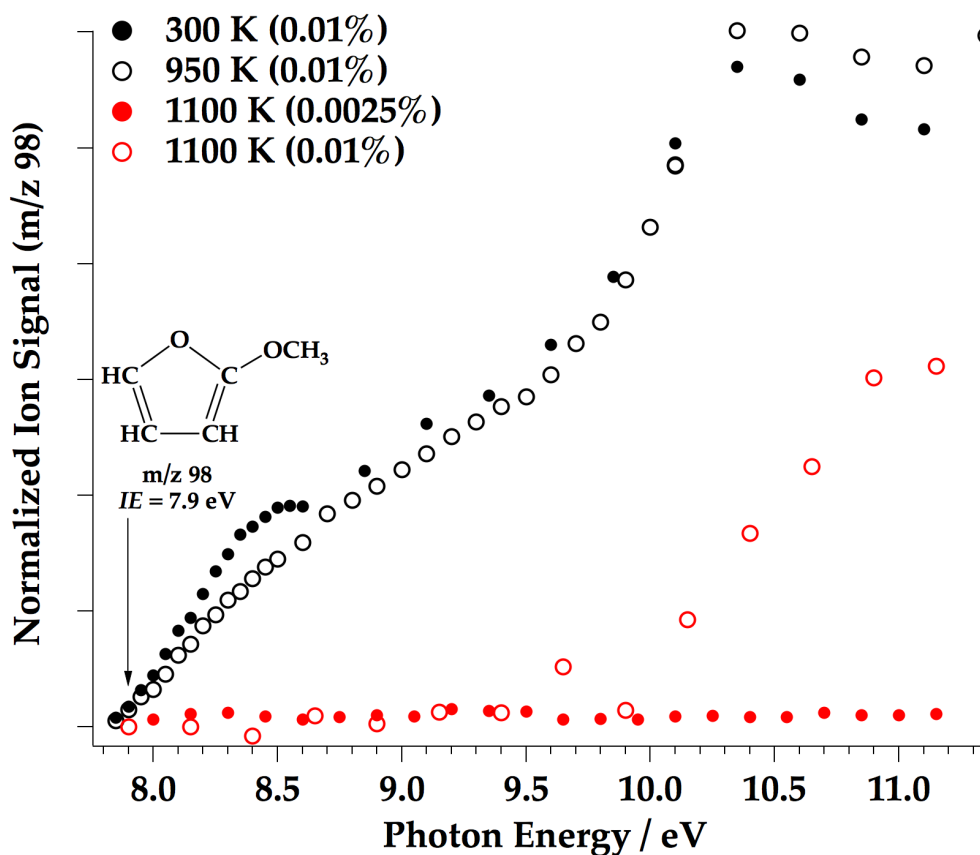
Figure 4.13: Photoionization efficiency curves of m/z 98. Mass 98 that appears at 1100 K from pyrolysis of a 0.01% mixture could be 5-methyl-2(5H)-furanone from CH$_3$ addition at C5 on 2-methoxyfuran (see Scheme 4.5).

Examination of the PIE(m/z 98) in Fig. 4.13 is also insightful into identifying which intermediate species in Scheme 4.5 is formed at the conditions in the microreactor. Samples of 2-methoxyfuran at 300 K and 950 K in a continuous flow helium reactor show an appearance energy of 7.9 eV which is compatible with the IE(2-methoxyfuran). Heating a very dilute sample (0.0025%) of 2-methoxyfuran to 1100 K produces no ions at m/z 98, indicating all methoxyfuran is consumed and no species associated with bimolecular reactions are observed. However a more concentrated mixture, 0.01%, now leads to an ion signal at m/z 98 that rises well above 7.9 eV. The CH_3 radical addition reactions in Scheme 4.5 could lead to an intermediate at m/z 98. Based on estimates of the ionization energies of these intermediate species, shown in Table 4.1, 5-methyl-2(5H)-furanone could be formed by addition of CH_3 at C5 on methoxyfuran and has an ionization threshold just above 10 eV [150]. If the intermediate was the result of CH_3 addition at C3 the predicted ionization threshold for these methylated 2(3H) furanones are 1 eV lower in energy.

The methyl vinyl ketone that appears in trace amounts in the IR spectrum of Fig. 4.10 is likely due to decomposition of a methylated furanone. The PIE(m/z 98) of a concentrated sample clearly indicates there is a stable intermediate that is not methoxyfuran, which, as mentioned above, could be 5-methyl-2(5H)-furanone. There are a few possible decomposition routes for this methylated furanone that could result in the formation of methyl vinyl ketone. Recent electronic structure calculations indicate [149] that the lowest-energy decomposition route for 5-methyl-2(5H)-furanone is ring opening to 1-pentene-1,4-dione, as shown in Scheme 4.5.5. The furanone could also decompose through an addition-elimination reaction with H-atom, converting the 2(5H) intermediate to 5-methyl-2(3H)-furanone (or α-angelica lactone), which has been shown to eliminate CO and produce MVK either through a concerted reaction or through an open-chain pentene-dione intermediate. For a more complete discussion on the decomposition patterns of the furanones and methylated furanones, see Chapter 5.

Finally, the absence of PIMS signals at m/z 82 excludes CH_3 addition to 2-methoxyfuran

at the C2 position. Indeed the rate constant for this reaction at 1000 K is two times slower than methyl addition at C5 [133]. Exclusion of reaction at the C2 position therefore excludes reactions at C3 or C4 as they are predicted to be another order of magnitude slower.

4.3.2   Radical-Radical Reactions

Both the PIE(m/z 83) and the vibrational bands in the IR demonstrate that 2-furanyloxy radical (m/z 83) is a persistent radical. Consequently, products resulting from reactions of H-atoms or CH_3 radicals with this species must also be considered. The possible chemical outcomes of these reactions are shown in Scheme 4.6.
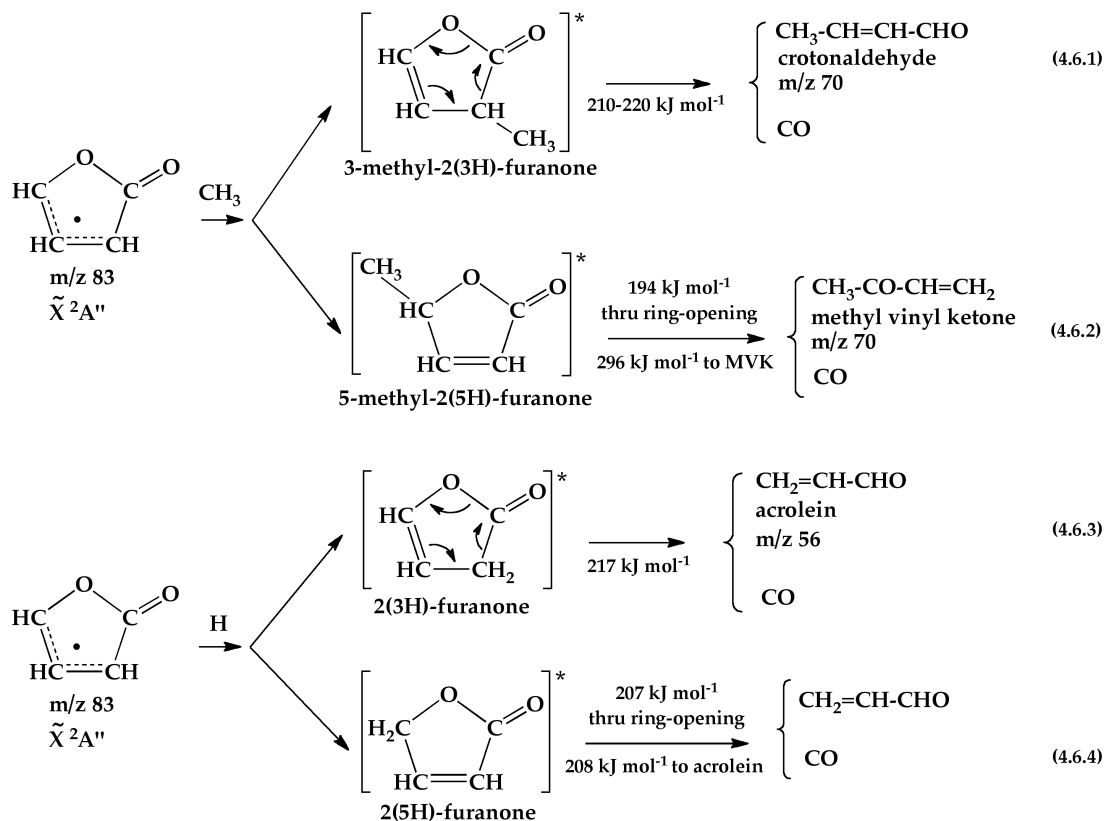
Scheme 4.6: Possible products resulting from reaction of H and CH_3 with 2-furanyloxy radical, including calculated reaction barriers [150] (see Chapter 5 for more details)

Concerted elimination of 3-methyl-2(3H)-furanone to crotonaldehyde and CO in Scheme 4.6.1, with a barrier of $210-220$ kJ mol^{-1} [150], would be thermodynamically feasible at the temper-

ature and pressure conditions in the reactor. Schemes 4.5.2 and 4.5.3 also predict formation of crotonaldehyde by CH_3 addition at C3 or C4 on 2-methoxyfuran. However, the calculated rate constants in Fig. 4.7 indicate CH_3 addition at C3 of methoxyfuran is slower than addition at C2; since no methylfuran at m/z 82 is observed in Fig. 4.8 resulting from a C2 addition, we conclude reactions slower than this should be excluded. Therefore it is likely CH_3 radical reactions with 2-furanyloxy in Scheme 4.6.1 are the source of crotonaldehyde observed in both the infrared (Fig. 4.10) and photoionization efficiency of m/z 70 (Fig. 4.12).

The products resulting from reactions of H-atom with furanyloxy are indistinguishable from hydrogen addition reactions to the parent. Reaction rates of H addition are very fast so knowledge of the pressure-dependence is necessary in order to draw any conclusions on the exact mechanistic path for the formation of acrolein at m/z 56.

4.3.3   Abstraction Reactions

The most thermodynamically favorable position for hydrogen atom abstraction by methyl or H-atom is the methyl group (or C7 as shown in Scheme 4.1). The kinetics of H-atom abstraction by methyl at the substituent group is over an order of magnitude more favorable than at any ring hydrogen [119].
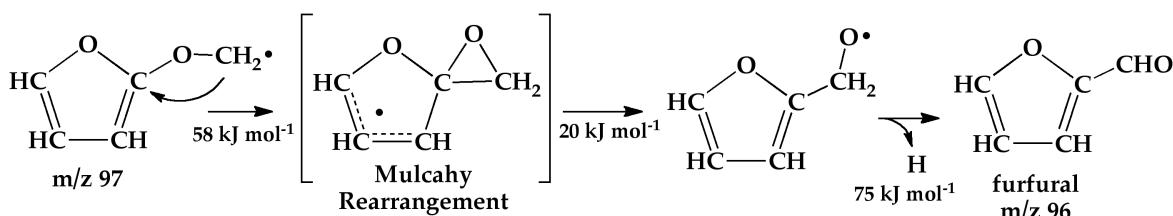
Scheme 4.7: Abstraction reaction scheme and calculated [133] reaction barriers.

Scheme 4.7 suggests that the resultant aryloxy(methyl) radical [24, 56], m/z 97, can isomerize *via* a Mulcahy rearrangement [92, 93] to furfural, m/z 96. PIMS spectra in Fig. 4.8 shows no signals at m/z 96 or 97 for methoxyfuran diluted in He, but PIE curves compared to the known photoionization cross-section of CH_4 [141] identify trace amounts of methane (IE

$= 12.618 \pm 0.004$ eV [117]). In addition, trace absorbance features at 1306.2/1305.5 cm^{-1} are observed in an Ar matrix, indicative of CH$_4$ (ν_4) splitting in Ar [98]. There are also features in the IR at 1688.4 cm^{-1} and 758.9 cm^{-1} which could be assigned to *anti*-C$_4$H$_3$O-CHO (ν_5) and (ν_{23}), respectively [89]. However, the other intense bands of furfural are not clearly distinguishable: *syn*-C$_4$H$_3$O-CHO (ν_5) which should appear at 1710.8 cm^{-1} overlaps with the more dominant bimolecular product crotonaldehyde (as shown in Fig. 4.10) while the other intense bands at 1469 and 747 cm^{-1} are obscured by unreacted methoxyfuran. In general, the amount of CH$_4$ that grows in is more proportional to the temperature of the reactor (and concentration of CH$_3$) than it is to features that correspond to furfural (see Fig. C.2 in Appendix C).

There is the possibility that methyl radicals could abstract a hydrogen from impurities on the surface of the SiC reactor, creating small amounts of CH$_4$ while there is no evidence for furfural. A description of wall reactions and potential wall-inducing chemistry within the SiC reactor was discussed at length in Vasiliou *et al.* [138]. This study found that fully deuterated samples of acetaldehyde (CD$_3$-CDO) produced only CD$_3$ radicals and no partially-deuterated methyl radicals were detected to indicate exchange with impurities on the hot reactor walls. However, in the case of methoxyfuran, there is an excess of methyl radicals flowing through the reactor at much earlier time-scales because they are produced by breaking a 190 kJ mol^{-1} bond versus DH$_{298}$(CH$_3$−CHO) $= 354.8 \pm 0.8$ kJ mol^{-1} [138]. This additional time in the reactor allows more collisions of radicals with the hot reactor walls, thus more opportunities to abstract from any impurities.

Based on the minimal evidence for furfural and only trace levels of CH$_4$ detected we conclude that abstraction reactions from methoxyfuran are not occurring under the operating conditions in the microreactor. Calculated reaction rates of hydrogen abstraction by methyl are consistent with these results indicating that abstraction reactions only become competitive with CH$_3$ addition reactions at much higher temperatures [119] than those reported here.

4.4 Kinetics of Methoxyfuran Decomposition

Similar to the conversion measurements of Bruinsma *et al.* [23], the conversion of 2-methoxyfuran in a continuous flow of He at several reactor wall temperatures and reactant concentrations was measured and is summarized in Fig 4.14. A kinetic mechanism of 24 species and 22 reactions, shown in Table 4.2, was developed including several unimolecular and bimolecular rate constants calculated by Simmie *et al.* [119, 133]. Eight reactions describe the unimolecular dissociation of methoxyfuran and its intermediates; the remaining 14 reactions are secondary reactions (H/CH$_3$ addition, abstraction and radical-radical reactions). The notations for addition reactions are the intermediates formed when CH$_3$ or H adds to the methoxyfuran ring at the specified position (*i.e.* CH$_3$-C5 is the intermediate formed when CH$_3$ adds to methoxyfuran at the C5 position, as shown in Scheme 4.5). At this time, no rate constants for the conversion of these bimolecular intermediates to final products are included in the mechanism.

4.4.1 Consumption of 2-Methoxyfuran

The Excel-based solver program Kintecus [57] was used to solve the system of equations at several gas temperatures and reactant concentrations. All rate constants included in the mechanism are high-pressure limiting (k$_\infty$) and assumed irreversible. A constant temperature profile and constant volume was also assumed for a residence time up to 200 μs. Calculations of the flow field in the reactor indicate that the temperature in the heated region is relatively constant between the approximately 1.5 cm between the electrodes (as shown in Fig. 2.3 on page 15). For these simulations the gas temperature was assumed to be the same as the reactor wall temperature.

Figure 4.14 compares the extent of methoxyfuran consumption by measurement of the photoion signal at four reactor wall temperatures compared to the observed ion signal in a room temperature scan of the same mixture. The dashed lines represent the predicted limits of
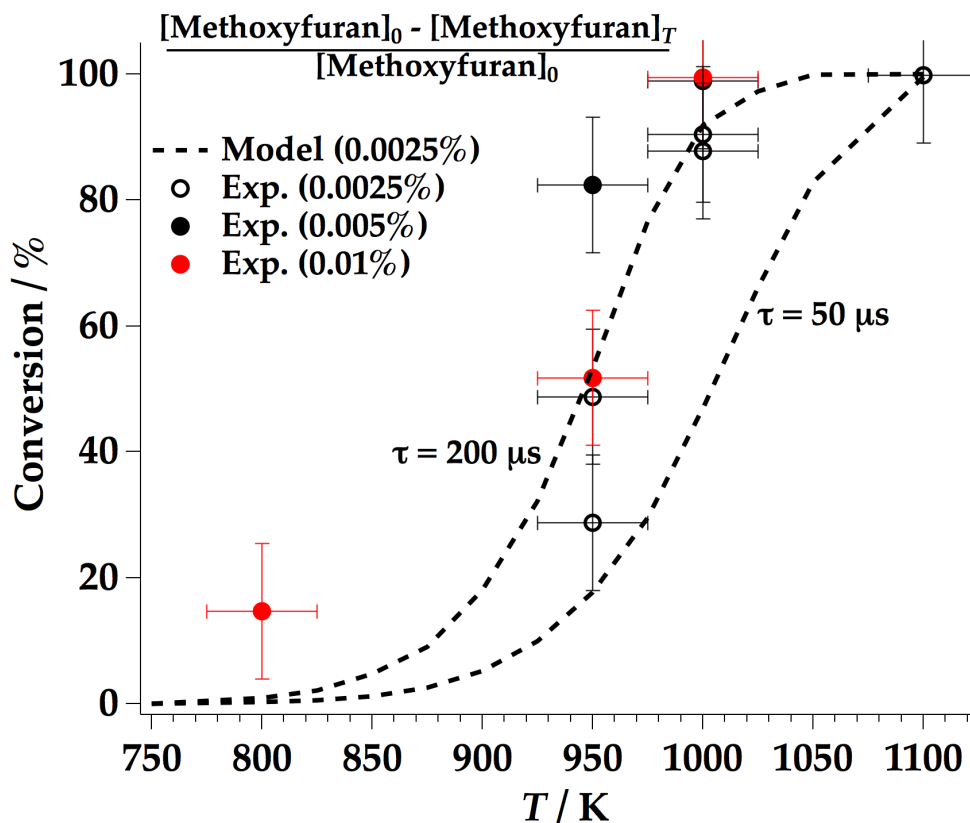
Figure 4.14: Percent conversion of 2-methoxyfuran; experimental measurements and estimated measurement uncertainties versus predictions of the first $50-200$ μs using the kinetic mechanism in Table 4.2.

methoxyfuran conversion assuming a residence time between $50-200$ μs and a concentration of 0.0025% in helium; increasing the reactant concentration increases the percent conversion at a given temperature by at most an additional 2%. The vertical uncertainty limits applied to all data points indicated in Fig. 4.14 were determined from the 2σ standard deviation of a PIE scan at m/z 98 collected at 950 K from 8.0 to 9.0 eV, averaging the observed conversion from 11 data points. The large uncertainty can in part be attributed to fluctuations of the reactor temperature throughout the length of the scan, approximately 10 minutes. The horizontal uncertainty limits are $\pm$ 25 K of the measured reactor wall temperature; this level of uncertainty may be generous, as the gas inside the reactor will be less meaning that the recorded temperature could be closer to $\pm$ 50 K from the actual gas temperature.

Table 4.2: Reaction mechanism with rate constant parameters. Notations for CH_3 or H addition reactions are the intermediates formed when CH_3 or H adds to the methoxyfuran ring at the specified position.

#	Reaction	A	n	E_a	Ref.
Unimolecular Reactions					
1	$C_4H_3O(OCH_3) \rightarrow C_4H_3O_2 + CH_3$	5.00E+13	0.00	1.84E+05	[119]
2	$C_4H_3O_2 \rightarrow$ O=C=CH-CH-CHO	2.145E+15	0.00	1.61E+05	[119]
3	O=C=CH-CH-CHO $\rightarrow$ CO + CH=CH-CHO	2.294E+15	0.00	1.37E+05	[119]
4	CH=CH-CHO $\rightarrow$ HCO + HC≡CH	1.008E+13	0.00	1.21E+05	[119]
5	CH=CH-CHO $\rightarrow$ O=C-CH=CH_2	4.56E+08	0.00	9.44E+04	[119]
6	O=C-CH=CH_2 $\rightarrow$ CO + CH_2=CH	3.194E+15	0.00	1.08E+05	[119]
7	HCO $\rightarrow$ H + CO	3.61E+13	0.00	6.42E+04	[67]
8	CH_2=CH $\rightarrow$ H + HC≡CH	2.00E+14	0.00	1.66E+05	[8]
CH_3 and H Addition/Abstraction Reactions					
9	$CH_3 + C_4H_3O(OCH_3) \rightarrow CH_4 + C_5H_5O_2$	2.80E+00	3.65	3.42E+04	[119]
10	$CH_3 + C_4H_3O(OCH_3) \rightarrow CH_3$-C2	1.15E+04	2.47	2.49E+04	[119]
11	$CH_3 + C_4H_3O(OCH_3) \rightarrow CH_3$-C3	4.06E+04	2.31	4.12E+04	[119]
12	$CH_3 + C_4H_3O(OCH_3) \rightarrow CH_3$-C4	3.04E+04	2.33	4.27E+04	[119]
13	$CH_3 + C_4H_3O(OCH_3) \rightarrow CH_3$-C5	3.38E+04	2.32	2.02E+04	[119]
14	$H + C_4H_3O(OCH_3) \rightarrow$ H-C2	3.55E+06	1.908	5.99E+03	[133]
15	$H + C_4H_3O(OCH_3) \rightarrow$ H-C3	8.55E+06	1.844	8.01E+03	[133]
16	$H + C_4H_3O(OCH_3) \rightarrow$ H-C4	4.92E+06	1.947	1.03E+04	[133]
17	$H + C_4H_3O(OCH_3) \rightarrow$ H-C5	7.18E+06	1.858	5.41E+03	[133]
Radical-Radical Reactions*					
18	$C_4H_3O_2 + CH_3 \rightarrow$ 3-CH_3-2(3H)Furanone	1.64E+13	-0.32	-5.50E+02	[133]
19	$C_4H_3O_2 + CH_3 \rightarrow$ 5-CH_3-2(5H)Furanone	1.64E+13	-0.32	-5.50E+02	[133]
20	$C_4H_3O_2 + H \rightarrow$ 2(5H)-Furanone	1.59E+14	0.18	-5.20E+02	[133]
21	$C_4H_3O_2 + H \rightarrow$ 2(3H)-Furanone	1.59E+14	0.18	-5.20E+02	[133]
22	HCO + H $\rightarrow$ H_2 + CO	9.00E+13	0.00	0.00E+00	[8]

Units: cm^3 mol s J K; $k = AT^n \exp(-E_a/RT)$; all rates k_∞

*Recombination rate constants

As shown in Fig. 4.14 most experimental data points lie within or very close to the estimated residence time limits; however, recent CFD simulations [49] indicate that the residence time in the continuous flow reactor is likely in the range of $50-100$ μs so an upper

limit of 200 μs might be excessive. One major issue that needs to be addressed with this type of measurement is accurately quantifying the ion signal when comparing over a range of temperatures. As the temperature of the fluid increases both the radial and axial velocity components of the molecular beam also increase. It is possible that some signal is lost due to a higher radial velocity component at elevated temperatures, and therefore the conversion would be overestimated when compared to the ion signal of a room temperature scan. This could explain why most of the experimental points in Fig. 4.14 lie closer to the upper estimate of the residence time, because in fact the conversion at that temperature is less than the measurement suggests. Preliminary results on this effect are discussed in Appendix A.1, indicating that a careful calibration or use of an appropriate internal standard is required for measurements of this sort in the future.

The scatter in the data in Fig. 4.14 also point to a need for tighter controls on the temperature measurement. The recorded wall temperature is likely an estimate of the wall temperature, and may not be exactly the temperature of the thermocouple readout. The temperature control has historically been monitored manually, by adjusting the current output on a power supply; however, this dataset suggests that an electronically controlled temperature measurement will be necessary for sensitive kinetic measurements in the future. In addition, temperature measurement with a 0.01 in diameter Type K thermocouple was used for these measurements in place of the standard 0.005 in diameter Type C thermocouple. Use of the larger diameter wire likely reduced the amount of contact between the thermocouple junction and the reactor wall, making the temperature measurement less reliable.

Although there is considerable scatter in the conversion data presented in Fig. 4.14, overall we can conclude that the high-pressure limiting rate constants for consumption of methoxyfuran seem appropriate to model the disappearance of methoxyfuran at the conditions in the microreactor.

4.4.2   Quantification of 2-Furanyloxy Radical

As shown in Scheme 4.2 the thermal decomposition of 2-methoxyfuran is initiated by cleavage of the $O-CH_3$ bond to form CH_3 and 2-furanyloxy radicals. Evidence in the IR and PIE(m/z 83) demonstrates the lifetime of 2-furanyloxy is long enough to survive the hot reactor and therefore it would be valuable to quantify the amount of this unreacted radical present at a given temperature. This information will be useful to interpret the likelihood of the radical-radical reactions presented in Section 4.3.2 and can also provide an estimate of the photoionization cross-section of this allylic lactone.

Since there is little evidence for the open-chain dione (O=C=CH-CH-CHO) and formyl vinyl (CH=CH-CHO) radicals, here we will assume all 2-furanyloxy decomposes to form the stable products CO and HCCH in addition to H-atom. With this assumption in mind, one way quantify the radical pool of 2-furanyloxy is to measure the loss of methoxyfuran compared to a room temperature scan while also monitoring the formation of the closed-shell products (HCCH or CO), as shown in Scheme 4.2:

$$[\text{2-furanyloxy}] = [\text{2-methoxyfuran}]_{300\text{K}} - [\text{2-methoxyfuran}]_T - [\text{HCCH or CO}]_T \qquad (4.1)$$

However, as described in Chapter 2.3.1, it is difficult to measure the absolute concentration of a species, and it is more straightforward to measure the number density ratios of two molecular species using a formulation of Beer's law for photoionization. This method was also previously implemented in the measurement of product ratios for the thermal decomposition of furan in Chapter 3. A similar method can be applied to methoxyfuran decomposition in an effort to quantify how much of the furanyloxy radical intermediate is present at a given temperature. Since the photoionization cross-section of this radical has not yet been measured, quantifying the observed ion signal must be accomplished in an indirect manner; one method is to measure the ratio of HCCH to CH_3:

$$\frac{[\text{2-furanyloxy}]}{[\text{CH}_3]} = 1 - \frac{[\text{HCCH}]}{[\text{CH}_3]} \qquad (4.2)$$

and then assume, with some obvious uncertainty due to possible secondary chemistry, that the remaining fraction is in the form of 2-furanyloxy. In order to cancel the photon-flux term, both measurements were made at the same photon energy, using Eq. (4.3) to estimate the ratio of acetylene to methyl radical:

$$\frac{[\text{HCCH}]}{[\text{CH}_3]} = \frac{S_{26}^+}{S_{15}^+} \frac{\sqrt{15}}{\sqrt{26}} \frac{\sigma_{\text{CH}_3}(\text{E})}{\sigma_{\text{HCCH}}(\text{E})} \tag{4.3}$$

where $\sigma_i(\text{E})$ is the reported photoionization cross-section, S_i^+ is the observed ion signal at a given photon energy and $\sqrt{m_i}$ is the mass discrimination factor as discussed in Chapter 2.3.1. The resulting measured ratio of HCCH to CH_3 for a 0.005% mixture of methoxyfuran in helium at 950 K is 0.88 ± 0.27 as summarized in Table 4.3. At 11.0 eV the absolute photoionization cross-section of methyl radical was reported to be σ_{CH_3} (11.0 eV) $= 6 \pm 1.8$ Mb [123]. The large uncertainty in the methyl cross-section (a relative uncertainty of 30% at 11 eV) is the dominant contributor to the uncertainty limits for the individual measurements of the methyl radical to acetylene ratio. Another measurement of the photoionization cross-section of methyl radical by Gans *et al.* [40] reports similar values and uncertainties to those measured by Taatjes *et al.* [123].

Table 4.3: Measured ratio of HCCH to CH_3; observed ion signals for 0.005% methoxyfuran in He at 950 K and photoionization cross-sections (Mb) of CH_3 [123] and HC≡CH [29].

eV[†]	m/z 15 (counts)[*]	$\sigma(\text{CH}_3)$	m/z 26 (counts)[*]	$\sigma(\text{HCCH})$	Ratio 26/15
11.40	4027	5.9	11840	15.3	0.86 ± 0.26
11.45	3906	6.8	14500	18.1	1.06 ± 0.32
11.50	3589	4.4	14630	18.3	0.74 ± 0.23
11.95	3944	5.5	24570	28.0	0.93 ± 0.28
12.00	4362	5.3	26490	28.1	0.87 ± 0.27
12.05	4642	5.8	26960	28.5	0.90 ± 0.28
					Average $= 0.88 \pm 0.27$

[†]No values of $\sigma(\text{CH}_3)$ reported between 11.5 and 11.95 eV

[*]Raw counts, baseline corrected only

The remaining fraction of 12% at 950 K is then assumed to be in the form of the radical intermediate 2-furanyloxy. An estimate of the photoionization cross-section for 2-furanyloxy

radical can be determined based on the relative fraction of furanyloxy to methyl radical:

$$\frac{[\text{2-furanyloxy}]}{[\text{CH}_3]} = \frac{S_{83}^+}{S_{15}^+} \frac{\sqrt{15}}{\sqrt{83}} \frac{\sigma_{\text{CH}_3}(\text{E})}{\sigma_{\text{2-furanyloxy}}(\text{E})} = 0.12 \pm 0.27 \qquad (4.4)$$

Since the cross-section of methyl radical also overlaps the PIE(m/z 83) curve, as shown in Fig. 4.5, the small overlap in the range $9.9-10.1$ eV can be used to estimate the photoionization cross-section of furanyloxy radical at these photon energies. Photon energies above 10.1 eV might be subject to dissociative ionization of unreacted methoxyfuran to m/z 83 (see Fig. C.3 in Appendix C for PIE(m/z 83) in a room temperature scan of methoxyfuran). Rearranging Eq. (4.4) and evaluating for the cross-section:

$$\sigma_{\text{2-furanyloxy}}(10.0 \text{ eV}) = \frac{4.6 \text{Mb}}{0.12} \left(\frac{2509}{3151} \frac{\sqrt{15}}{\sqrt{83}} \right) = 13 \pm 29 \text{ Mb} \qquad (4.5)$$

results in a photoionization cross-section measurement of 13 Mb at 10.0 eV, or about three times that of methyl radical. The large uncertainty limits are the result of uncertainty propagation in the measurement of the acetylene to methyl radical ratio (Table 4.3), which is dominated by the accuracy of the photoionization cross-section measurement of methyl radical. To the best of our knowledge the only unsaturated lactone that has an absolute photoionization cross-section measurement is α-angelica lactone (5-methyl-2(3H)-furanone, molecular structure shown in Scheme 4.5.4) [30] with a photoionization cross-section at 10.0 eV of about 18 Mb (at most $\pm$ 2.7 Mb based on an upper limit of 15% uncertainty estimated by [30]).

It should be noted that use of the high-pressure limiting rate constants shown in Table 4.2 predict only $0.1-0.7\%$ furanyloxy concentration relative to methyl radical for a 0.005% reactant mixture at 950 K (residence time $50-200$ μs), which is over a magnitude lower than the experimental measurement. However, use of the high-pressure limiting rate constant for Reaction 2 in Table 4.2 is likely not valid for the conditions in the microreactor and this difference could be accounted for if its pressure-dependence was known. When the A-factor of k_2 is arbitrarily reduced by a factor of 50 the predicted ratio of 2-furanyloxy to methyl radical is an average of 12% within the residence time limits.

4.4.3   Quantification of Bimolecular Products

Another valuable measurement to quantify and compare to predictions is the amount of bimolecular chemistry observed at different experimental conditions. The two most abundant secondary products detected by both PIMS and infrared spectroscopy are acrolein (CH_2=CH-CHO) and crotonaldehyde (CH_3-CH=CH-CHO), as described in detail in Sections 4.3.1 and 4.3.2. A summary of the measured ratio of these species relative to methyl radical are summarized in Table 4.4 and compared to predictions.

Table 4.4: Quantification of the bimolecular species acrolein (CH_2=CH-CHO) and croton-aldehyde (CH_3-CH=CH-CHO) relative to methyl radical. Experimental results compared to predictions using high-pressure rate constants and a reduced rate constant for ring opening of 2-furanyloxy (Reaction 2 in Table 4.2).

		Ratio of CH_2=CH-CHO to CH_3		
Methoxyfuran/He	T (K)	Exp.	Model (k_∞)	Model ($k_2/50$)
0.005%	950	$1.3 \pm 0.3\%$	$1-5\%$	$10-16\%$
0.01%	950	$1.5 \pm 0.7\%$	$3-9\%$	$14-22\%$
0.01%	1100	$1.8 \pm 0.4\%$	$-$	$-$

		Ratio of CH_3-CH=CH-CHO to CH_3		
Methoxyfuran/He	T (K)	Exp.	Model (k_∞)	Model ($k_2/50$)
0.005%	950	$0.7 \pm 0.3\%$	$<0.01\%$	$0.1-0.3\%$
0.01%	950	$1.9 \pm 0.7\%$	$0.01-0.02\%$	$0.2-0.4\%$
0.01%	1100	$1.5 \pm 0.3\%$	$-$	$-$

The experimental ratios were measured in the same manner as described above for the ratio of acetylene to methyl radical in Eq. (4.3). In general, the formation of secondary products observed at these conditions is small: the ratio of acrolein (m/z 56) to methyl radical is about $1-2\%$ at both temperatures and reactant concentrations. For the purpose of this calculation the ion signal at m/z 70 is assumed to be entirely crotonaldehyde and the ratios calculated using the appropriate photoionization cross-section of both species [29, 156]. Observations of crotonaldehyde relative to methyl are also about $1-2\%$ at both temperatures and reactant concentrations. A comparison to CH_3 was chosen so that measurements could

be made at a common photon energy. The cross-section for acrolein is not reported above 11.0 eV, so comparison with acetylene, a stable closed-shell species, is not straightforward. The photoionization cross-section of crotonaldehyde [156] has been measured up to 11.75 eV, so a comparison can be made between the signal of crotonaldehyde relative to acetylene at the same photon energy. For a 0.01% mixture at 1100 K (when all 2-furanyloxy has been consumed) the ratio of CH_3-CH=CH-CHO to HCCH is 0.7 ± 0.1%, within a factor of two of the measurement of CH_3-CH=CH-CHO to CH_3 (shown in Table 4.4) at the same conditions but measured at lower photon energies.

The experimental measurements are compared to kinetic predictions using the mechanism in Table 4.2. The first model column in Table 4.4 assumes the high-pressure rate constants for all reactions from Table 4.2 while the second model column reduces the A-factor of Reaction 2 (furanyloxy $\rightarrow$ O=C=CH-CH-CHO) by a factor of 50 to account for the pressure-dependence of the ring-opening, as described in Section 4.4.2. The model predictions of acrolein formation also assume that all intermediates formed in the residence time range of $50-200$ μs from Reactions 15, 16, and 21 in Table 4.2 are converted to acrolein as final product. This is clearly an overestimation, as the conversion will not be 100% and will likely have significant pressure-dependencies. It is also assumed that all intermediates formed from Reactions 11, 12 and 18 in Table 4.2 result in the formation of crotonaldehyde.

In general, the formation of secondary products observed at these conditions is small, accounting for less than 4% of total methoxyfuran decomposition. The remainder of decomposition follows the unimolecular reaction in Scheme 4.2. Predictions using the kinetic model are not fully complete at this time, but they do confirm the formation of intermediates from CH_3 or H addition reactions and reactions with 2-furanyloxy at the temperatures and residence times in the microreactor. Moreover, they offer a valid explanation for the species observed that are not included in the unimolecular reaction scheme.

4.5   Methoxyfuran Conclusions

The unimolecular thermal decomposition scheme of 2-methoxyfuran predicted computationally by Simmie *et al.* [119] is confirmed experimentally in a microreactor operated at $300-1300$ K, pressures up to 200 Torr and a residence time of $50-200$ μs. The primary products detected by photoionization time-of-flight mass spectrometry and FT-IR spectroscopy in an Ar matrix include CH_3, 2-furanyloxy, CO and $HC{\equiv}CH$. Secondary products resulting from H or CH_3 addition to 2-methoxyfuran and radical-radical reactions with 2-furanyloxy have also been detected and include $CH_2{=}CH\text{-}CHO$, $CH_3\text{-}CH{=}CH\text{-}CHO$, $CH_3\text{-}CO\text{-}CH{=}CH_2$ and furanones; quantification of the ion signal of these species indicates secondary reactions contribute to at most 4% of total methoxyfuran decomposition depending on the temperature and reactant concentration.

The 2-furanyloxy radical was also characterized by PIMS and IR spectroscopy. The carbonyl stretch (ν_4) and several other intense infrared vibrational bands of this allylic lactone were assigned in an Ar matrix in addition to the ionization threshold and photoionization efficiency curve. There is no evidence for the other radical intermediates involved in the thermal decomposition of 2-methoxyfuran, indicating their lifetimes are too short to be detected under the operating conditions in the microreactor.

Results of calculations with a kinetic mechanism indicate that the high-pressure limiting rate constant for Reaction 1 in Table 4.2 (2-methoxyfuran $\rightarrow$ CH_3 + 2-furanyloxy) is valid in the pressure regimes of the microreactor (inlet pressure $100-200$ Torr). Although there is scatter in the measurements of methoxyfuran conversion as a function of reactor temperature, the experimental measurements are in general agreement with the predictions.

Thermal Decomposition Mechanisms of the Lactones 2(5H)-Furanone,
2(3H)-Furanone and α-Angelica Lactone

Lactones, among other furanic compounds, are found in bio-oil formed from a dehydration reaction of the cellulose/hemicelluose in wood and agricultural residues during fast pyrolysis [34, 75]. Liaw *et al.* specifically report approximately 1% of the dry condensable organic matter from fast pyrolysis of these residues is in the form 2(5H)-furanone. α-Angelica lactone is a naturally occurring substance commonly used by the food industry as an aroma and flavoring additive [160]; it is also a potential oxidation product of other biofuel candidates [30, 157]. In addition, all three of the title compounds were conjectured intermediates of radical addition reactions in the thermal decomposition of 2-methoxyfuran presented in Chapter 4. For these reasons, the pyrolysis behavior of the lactones shown in Fig. 5.1 were studied experimentally in the microreactor.
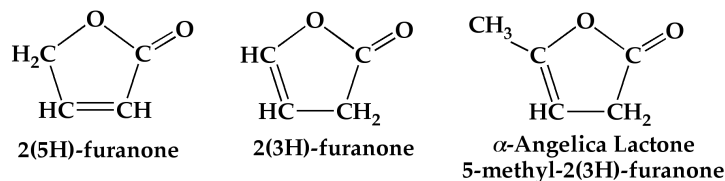
Figure 5.1: Structures of the lactones investigated; numbering begins at the ether oxygen and proceeds clockwise around the ring.

The liquid-phase interconversion of furanones has been reported [35], but there have been limited studies performed on the gas-phase behavior of these molecules. The thermal

decomposition of several furanones and their methylated derivatives was studied by Xu *et al.* [154] in a low-pressure quartz flow reactor (45 cm by 1.2 cm i.d.). The sample was introduced into the reactor with approximately 0.6−1 mbar (4.5−7.5 Torr) of neat reactant [25] and no estimate of the residence time was provided. The primary products detected from the decomposition of both 2(3H)-furanone and 2(5H)-furanone by photoelectron spectroscopy were CO and acrolein (CH_2=CH-CHO). During the pyrolysis of one isomer they also reported the appearance of the other isomer, suggesting a gas-phase interconversion of the two furanones. They concluded that 2(3H)-furanone eliminates CO by a concerted reaction, as shown in Scheme 5.1.1, to produce acrolein. They also postulated that 2(5H)-furanone does not produce acrolein directly, but rather isomerizes to 2(3H)-furanone by two consecutive 1,2-hydrogen shifts, as shown in Scheme 5.1.2, proceeding through a biradical intermediate.
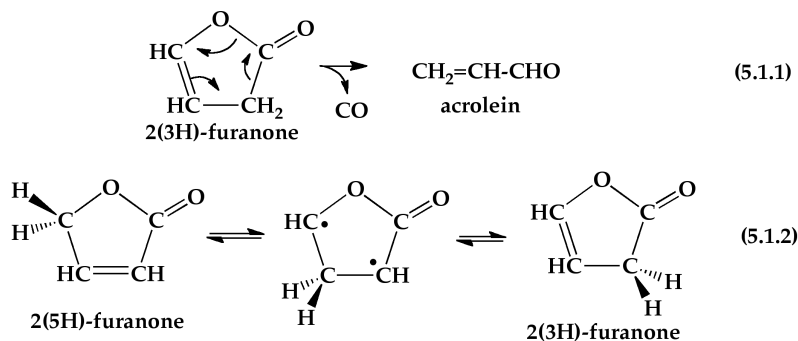
Scheme 5.1: Xu *et al.* [154] postulated that decomposition of 2(3H)-furanone proceeds through a concerted reaction to form carbon monoxide and acrolein. Their results also suggest that consecutive 1,2-hydrogen shifts interconvert the furanones.

In a similar manner to the decomposition of 2(3H)-furanone, Xu *et al.* [154] also observed that the methylated analog 5-methyl-2(3H)-furanone (or α-angelica lactone) decomposes *via* a concerted reaction, producing CO and methyl vinyl ketone (CH_3-CO-CH=CH_2), as shown in Scheme 5.2. Isomerization of 5-methyl-2(3H)-furanone to 5-methyl-2(5H)-furanone was also observed in the Xu study [154], but to a lesser extent than for the un-substituted furanones.

More recently, electronic structure calculations of the furanones by Würmel and Sim-

α-angelica lactone
(5-methyl-2(3H)-furanone)

methyl vinyl ketone

CO
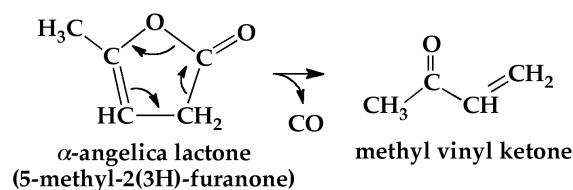
Scheme 5.2: α-Angelica lactone (5-methyl-2(3H)-furanone) was proposed by Xu *et al.* [154] to decarbonylate in a similar manner to 2(3H)-furanone.

mie [149, 150] indicate that the hydrogen-atom migration route in Scheme 5.1.2 is not the only plausible route to inverconvert the furanones. Their calculations predict that for 2(3H)-furanone the first 1→2 shift requires 240 kJ mol^{-1}, while the concerted elimination of CO from 2(3H)-furanone is more energetically favorable at 220 kJ mol^{-1}. Therefore, isomerization to 2(5H)-furanone from 2(3H)-furanone *via* this route seems unlikely given the experimental conditions tested by Xu *et al.* [154]. Instead, the computational studies [149, 150] suggest that a more likely routes to interconvert 2(3H)-furanone to 2(5H)-furanone is either a series of catalytic hydrogen atom addition/elimination reactions, as shown in Scheme 5.3.1, or through a hydrogen-shift followed by ring opening to 4-oxo-3-butenal, shown in Scheme 5.3.2. Würmel and Simmie [149] also proposed other possible decomposition routes for the lactones in Fig. 5.1, some of which will be discussed in more detail in proceeding sections.

2(5H)-furanone

2(3H)-furanone

(5.3.1)

4-oxo-3-butenal

(5.3.2)
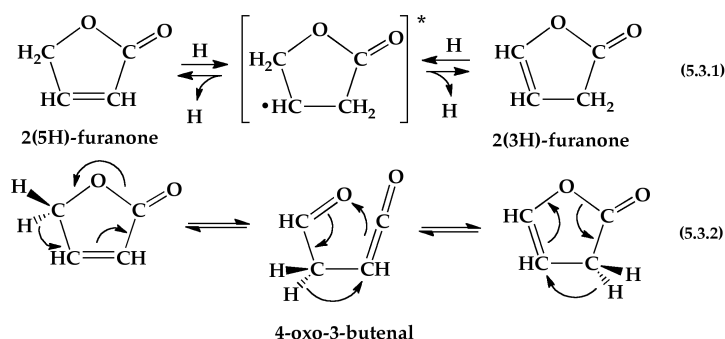
Scheme 5.3: Routes for interconversion of the furanones as proposed by Würmel and Simmie [149, 150]. Catalytic interconversion by H-atom addition has a small barrier to reaction (approximately 20 kJ mol^{-1}).

With the discrepancy between the interpretation of previous experimental results

and recent electronic structure calculations of these lactones, the goal of this work is to experimentally identify the decomposition mechanisms of these molecules relevant to furanic biofuels.

5.1   Experimental

2(3H)-furanone was synthesized using the procedure of Näsman and Pensar [94]; the sodium disulfite ($Na_2S_2O_5$) addition was not performed so unreacted furfural remains (the integrated intensities of a nuclear magnetic resonance (NMR) spectrum shows the fraction of furfural relative to 2(3H)-furanone is about 1:6). The Näsman synthesis also reports a 4:1 ratio of 2(3H)-furanone to 2(5H)-furanone after vacuum distillation; the integrated intensities in the NMR spectrum show the fraction achieved for this synthesis was closer to 3:1. The 2(5H)-furanone and α-angelica lactone samples (Aldrich, 98%) were used as received. An NMR spectrum of 2(5H)-furanone shows that less than 0.5% of the sample is in the form 2(3H)-furanone.

The most stable form of the angelica lactones is α-angelica lactone (α-AL, 5-methyl-2(3H)-furanone), however in the liquid-phase it can be found in equilibrium with two other isomers, β-AL (5-methyl-2(5H)-furanone) and γ-AL (5-methylene-dihydro-2(3H)-furanone or γ-methylene-γ-butyrolactone), as shown in Fig. 5.2 [160]. An NMR scan of the α-AL sample in CDCl$_3$ show that approximately 1.2% is in the form β-AL [5] and approximately 0.8% in the form γ-AL [2].
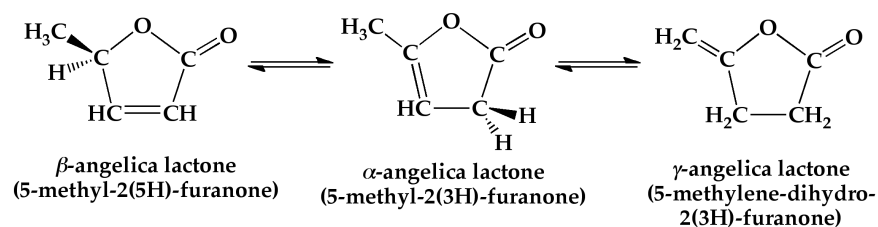
Figure 5.2: Structure of α-angelica lactone and the less stable isomers β- and γ-angelica lactone.

The microreactor used for this study consists of a resistively heated silicon carbide (SiC) tube, 2.5−3.8 cm in length, 1 mm i.d. and 2 mm o.d. with the flow through the reactor is controlled by a pulsed valve (Parker General Valve, series 9). The residence time is approximately 50−200 μs, with experiments in He on the lower end of this estimate and those in Ar towards the upper end. Products exiting the reactor are detected with fixed-frequency (118.2 nm or 10.487 eV) photoionization time-of-flight mass spectrometry (PIMS) and infrared spectroscopy in a cryogenic matrix. A more detailed description of the reactor assembly and diagnostics is included in Chapter 2.1 and also in [138, 158].

All reactants had low vapor pressures (less than 1 Torr at 300 K), so entraining the sample in a stream of helium or argon before entering the reactor required heating a few drops of a liquid sample in a small quartz sample tube (1.5 mm i.d., 15 mm long) to at most 60°C with a sample probe placed directly behind the pulsed valve. The reactant mixtures are estimated to be about 0.1% in He or Ar carrier gas, however it is quite possible that the concentration could be upwards of 0.2% in He or Ar, increasing the likelihood of secondary reactions. The reactant concentrations for these experiments are more uncertain due to lack of accurate vapor pressure measurements for many of these molecular species. In addition, due to the enclosed geometry and sample times required for the pulsed Ar experiments, the liquid sample behind the pulsed valve is in an elevated temperature environment for longer periods of time than for He experiments (on the order of minutes for PIMS scans versus 1-2 hour deposition for IR spectra). In the liquid phase 2(5H)-furanone is more stable than 2(3H)-furanone; while conducting the decomposition experiments of 2(3H)-furanone the freshly prepared sample may have interconverted to 2(5H)-furanone in the liquid phase prior to entering the heated reactor. In addition, the other angelica lactone isomers in Fig. 5.2 could be in higher concentrations at the elevated temperatures than estimated by NMR.

5.2 Pyrolysis of 2(3H)-Furanone and 2(5H)-Furanone

The primary thermal decomposition products detected by photoionization mass spectrometry (PIMS) and infrared spectroscopy for both 2(3H)- and 2(5)-furanone are acrolein (CH_2=CH-CHO) and carbon monoxide.

A recent computational study [149] predicts several decomposition routes to these final products; included in Schemes 5.4 and 5.5 are the lowest-energy decomposition pathways they reported that are potentially relevant to experimentally observed products. The energetics of the fate of the butenedial in Scheme 5.4.2 has not been evaluated, but if formed in the microreactor we postulate it could further fragment to acetylene, carbon monoxide and hydrogen atoms. In addition, the lowest-energy decomposition pathway of the aldehydic ketene (4-oxo-3-butenal) in Scheme 5.5.1 was calculated to be direct elimination of CO to give acrolein [149].
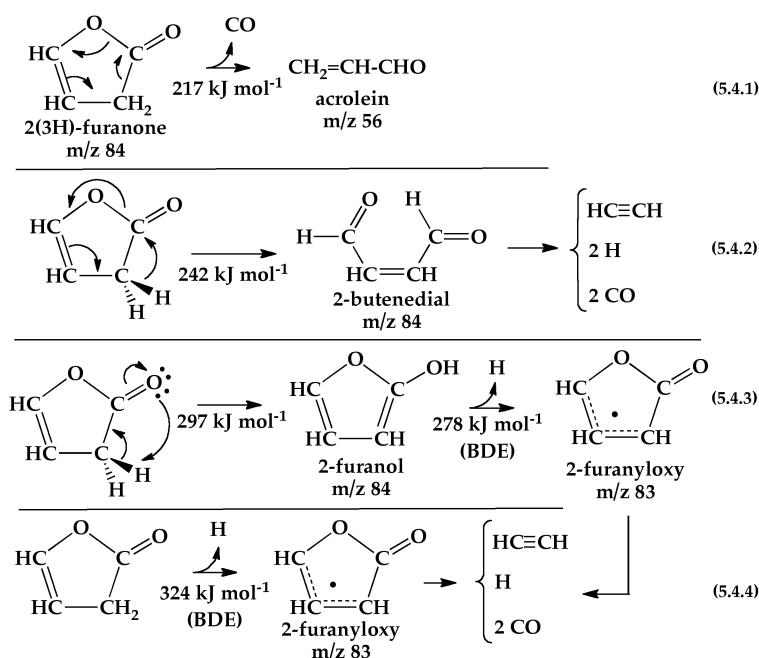
Scheme 5.4: Predicted lowest-energy decomposition pathways of 2(3H)-furanone as calculated by Würmel and Simmie [149]; select bond dissociation energies (BDE) or reaction barriers included.
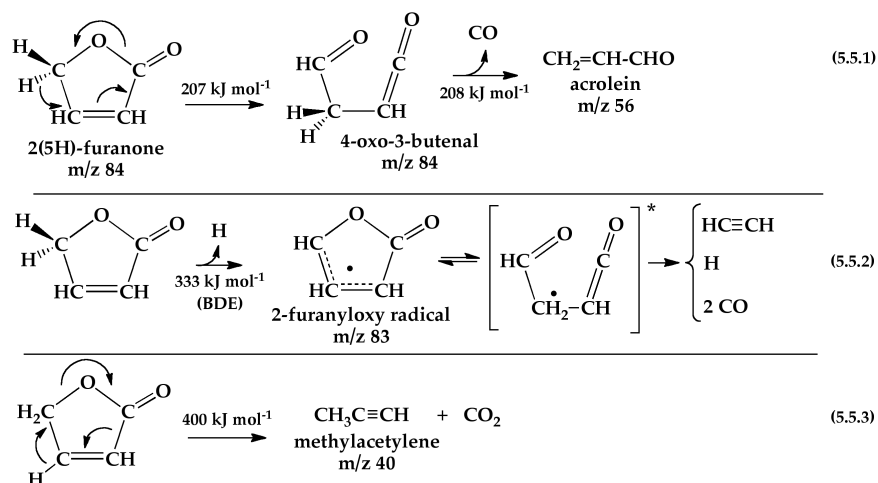
Scheme 5.5: Predicted lowest-energy decomposition pathways of 2(5H)-furanone as calculated by Würmel and Simmie [149]; select bond dissociation energies (BDE) or reaction barriers included.

Figure 5.3 shows the photoionization mass spectra (PIMS) recorded at several reactor temperatures for 0.1% mixtures 2(3H)-furanone (left) and 2(5H)-furanone (right) in helium. With the reactor held at 400 K, only the parent ion and the ^{13}C isotope are observed at m/z 84 and 85, respectively. The onset for decomposition of 2(3H)-furanone is observed at about 1000 K with the appearance of m/z 56, assigned to acrolein (CH_2=CH-CHO), as predicted in Scheme 5.4.1. The mass spectra from the decomposition of 2(5H)-furanone show that m/z 56 also appears when the reactor is between $1100-1200$ K, about $150-200$ K higher than for 2(3H)-furanone. The intense feature at m/z 55 in the right-panel of Fig. 5.3 is assigned to dissociative photoionization[1] of either the furanone or the possible open-chain intermediate at m/z 84, and is not a thermal product. The ions at m/z 28 could arise from one two possible channels, neither of which is a unimolecular thermal product: (1) ethylene (CH_2=CH_2) could be the result of secondary reactions that are accessible at elevated temperatures, or (2) m/z 28 could be an artifact of the ionization of acrolein (see Section 5.4.1 for a more thorough discussion on this species). The feature at m/z 40 is assigned to CH_3C≡CH and can be produced unimolecularly by decarboxylation, as in Scheme 5.5.3, or could also be the result

---

[1] $C_4H_4O_2$ + 118.2nm → $[C_4H_4O_2^+]^*$ → $C_3H_3O^+$ + HCO
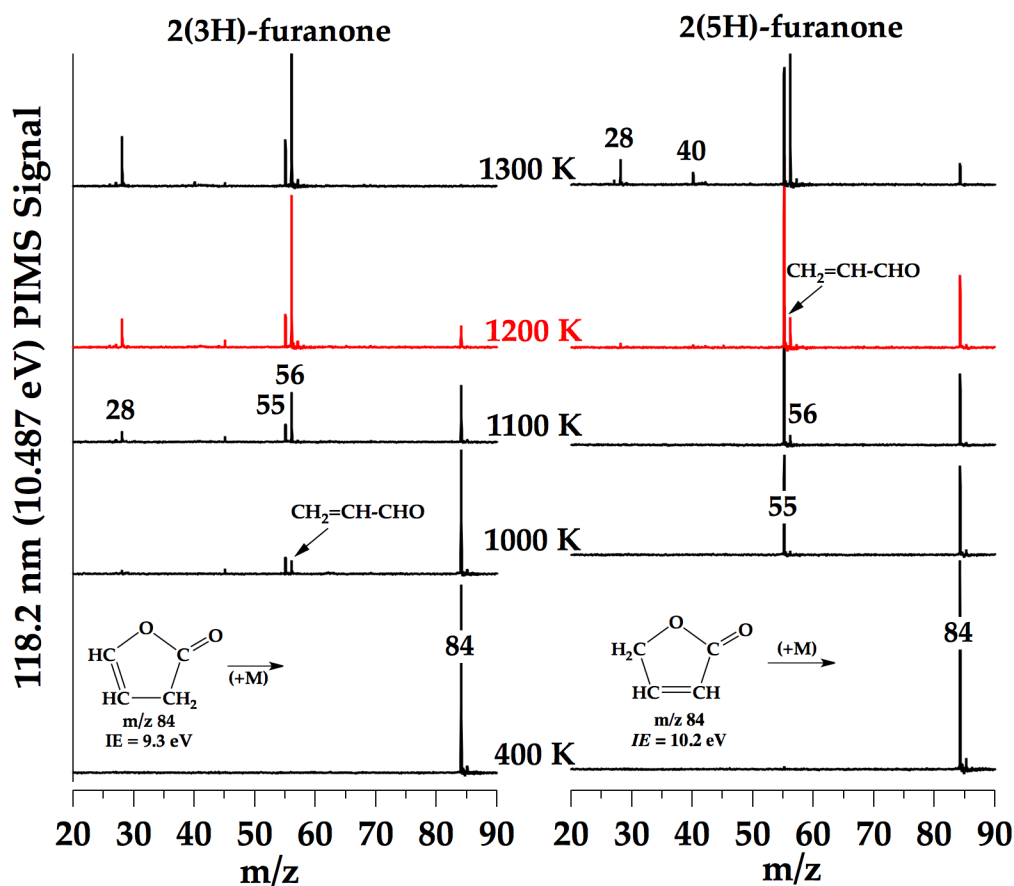
Figure 5.3: Product mass spectra of 2(3H)-furanone (left) and 2(5H)-furanone (right) in a pulsed reactor at several reactor temperatures. Concentration of reactant approximately 0.1% in He. The ionization energies of the two species are calculated values by Würmel *et al.* [150].

of secondary reactions.

The identity of acrolein (CH_2=CH-CHO) as a thermal product of both furanones is confirmed by infrared spectroscopy in an Ar matrix, as shown in Figs. 5.4 and 5.5. Assignment of both *cis* and *trans* conformers of acrolein were accomplished by a combination of previous studies in an Ar matrix [16, 60] and by authentic samples; Table C.2 in Appendix C includes a summary of these assignments. The IR also confirms that interconversion occurs, with the growth of the concomitant isomer (see Fig. C.4 in Appendix C): absorption features show that 2(3H)-furanone grows in as 2(5H)-furanone is heated, and vice versa.
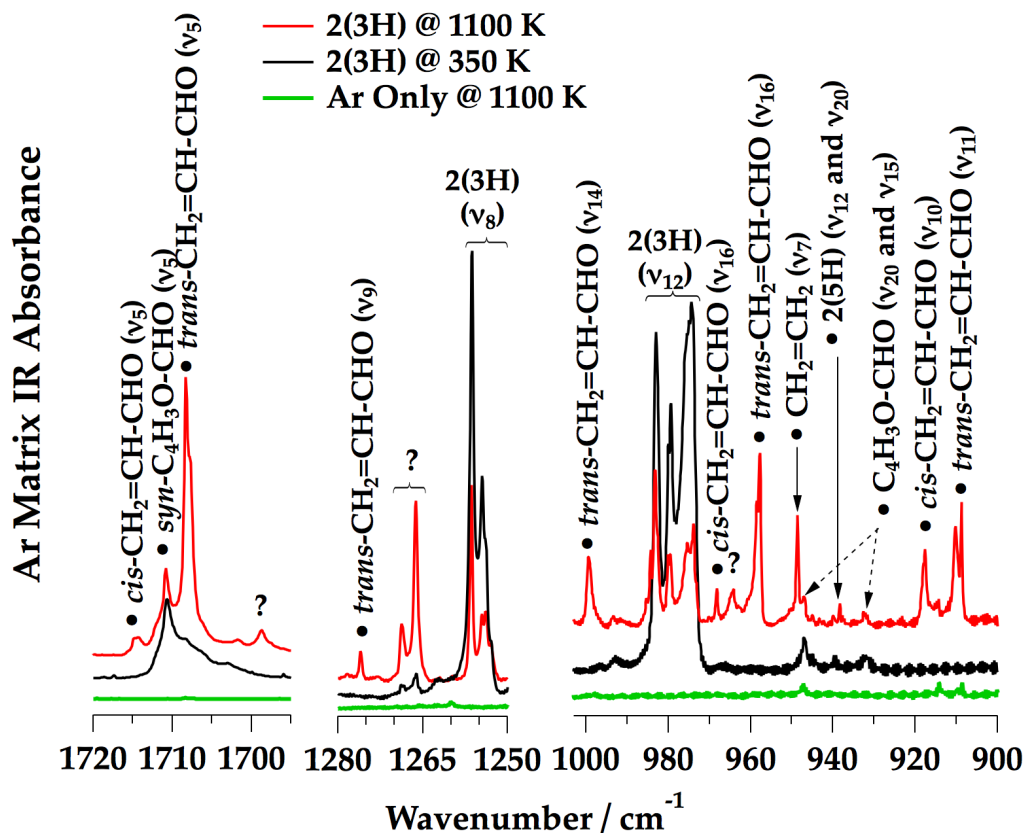
Figure 5.4: IR spectra identify acrolein (CH_2=CH-CHO) as a thermal product in the pyrolysis of 0.1% 2(3H)-furanone at 1100 K (3.5 mmol Ar deposited). Shown for comparison are reference scans with only Ar passed through a 1100 K reactor (3.5 mmol deposited) and 2(3H)-furanone through a 350 K reactor (2.6 mmol Ar deposited). Trace amounts of furfural from synthesis identified; unassigned absorption features (?) could result from impurities in the reactant sample or products formed from a minor reaction pathway.

In order to interconvert the furanones by the addition/elimination reactions proposed by Würmel *et al*. [150], a source of hydrogen atoms is necessary. In the pyrolysis of 2(5H)-furanone, one possible hydrogen atom source is rupture of the weakest C−H bond in 2(5H)-furanone, C5−H, at 333 kJ mol^{-1} [150], as shown in Scheme 5.5.2. Loss of the hydrogen atom from this position produces 2-furanyloxy radical, an allylic radical discussed in Chapter 4. Further decomposition of 2-furanyloxy was shown to produce acetylene, carbon monoxide and hydrogen atom (see Chapter 4.2). As shown in the PIMS spectra of Fig. 5.3 there is no signal observed at m/z 83 to suggest evidence for 2-furanyloxy radical. However, as shown
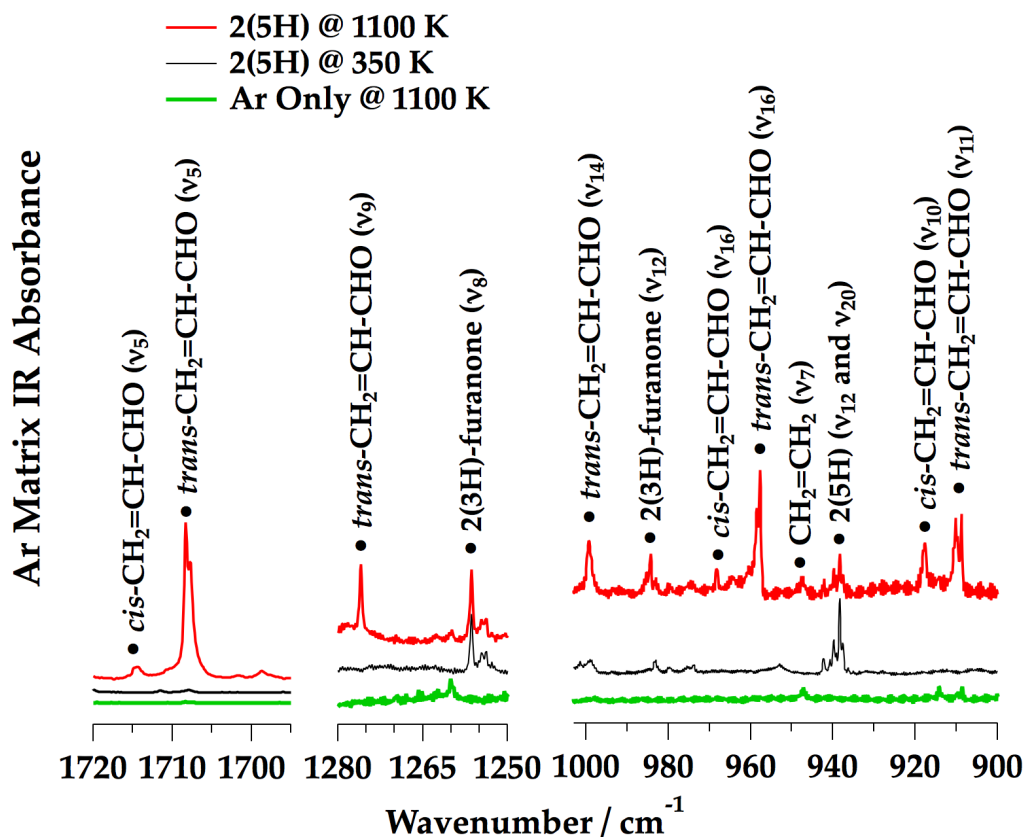
Figure 5.5: IR spectra also identifies acrolein (CH$_2$=CH-CHO) as a thermal product in the pyrolysis of approximately 0.1% 2(5H)-furanone at 1100 K (5.1 mmol Ar deposited). Shown for comparison are reference scans with only Ar passed through a 1100 K SiC reactor (3.5 mmol deposited) and 2(5H)-furanone through at 350 K reactor (3.2 mmol Ar deposited).

in the IR spectra in the right-panel of Fig. 5.6, a feature at 1732.8 cm^{-1} is observed and is assigned to the carbonyl stretch (ν_4) of 2-furanyloxy radical in Ar (see Fig. 4.6 in Chapter 4.2 and Table C.1 in Appendix C). The lifetime of 2-furanyloxy is likely to be much shorter in the decomposition of 2(5H)-furanone than in the decomposition of 2-methoxyfuran because in the case of the furanone, 2-furanyloxy radical is formed at much higher temperatures. The bond energy to form the allylic radical from 2(5H)-furanone is 333 kJ mol^{-1} [150] versus the 190 kJ mol^{-1} O$-$CH$_3$ bond in 2-methoxyfuran [119].

Another predicted low-energy [149] decomposition pathway of 2(5H)-furanone is by a H-shift from C5 to C4 followed by simultaneous cleavage of the C2$-$O1 bond to yield
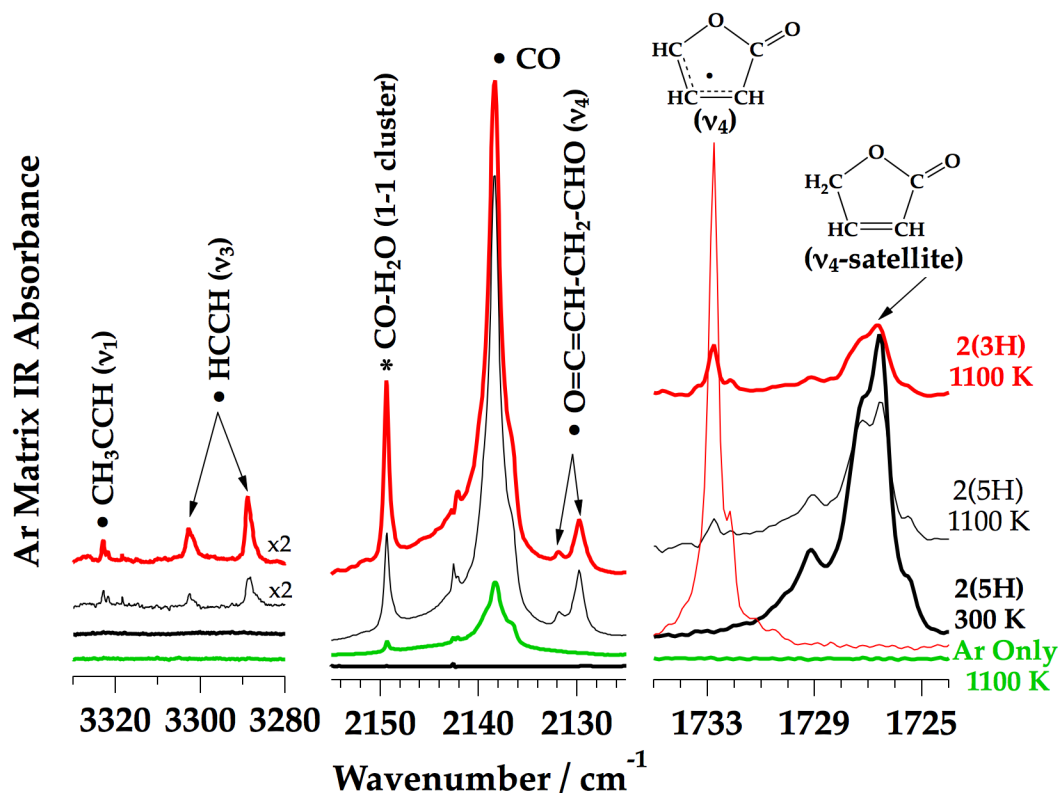
Figure 5.6: Minor decomposition products identified by IR. Thin red trace in far-right spectrum is the observed trace from pyrolysis of 0.04% 2-methoxyfuran in Ar, showing C=O stretch of 2-furanyloxy radical. In addition to identification of CO (center-panel), a ketene-like vibrational mode observed in an Ar matrix, assigned to 4-oxo-3-butenal (O=C=CH-CH$_2$-CHO). Spectra in far left and far right panels are scaled similarly.

an aldehydic ketene, 4-oxo-3-butenal (O=C=CH-CH$_2$-CHO), also with a mass of 84, as shown in Scheme 5.5.1. The only experimental evidence for the possibility of this species is a doublet at 2129.8 and 2131.8 cm^{-1} in the IR which is assigned to O=C=CH-CH$_2$-CHO(ν_4) based on calculations of the harmonic frequencies of this species [149]; authentic samples of this intermediate are needed to confirm this assignment. As shown in Scheme 5.5.1, a 1,4-hydrogen shift followed by elimination of CO can also form acrolein.

Although the reaction barrier for ring opening of the furanone to O=C=CH-CH$_2$-CHO (Scheme 5.5.1) was calculated [149] to be about 125 kJ mol^{-1} lower than the cleavage of the C5−H bond, the mass spectra show that signals at m/z 84 (and the associated dissociative

ionization peak at m/z 55) persist at higher temperatures for 2(5H)-furanone than for 2(3H)-furanone. The persistence of m/z 55 and 84 demonstrate the stability of either 2(5H)-furanone or the butenal compared to 2(3H)-furanone. The butenal could also be semi-stable and result in re-formation to the ring form, as depicted in Scheme 5.3.2.

The pyrolysis experiments of 2(3H)-furanone are somewhat complicated by the remaining fraction of 2(5H)-furanone (ratio of 2(3H)-furanone to 2(5H)-furanone approximately 3:1), however, the results of experiments indicate the primary mode for decomposition of 2(3H)-furanone is through Scheme 5.4.1: the formation of acrolein and carbon monoxide. The source of furanyloxy radical in the pyrolysis of 2(3H)-furanone, as observed in Fig. 5.6 could be from decomposition of the 2(5H) impurity, as in Scheme 5.5.3, or could be formed from 2(3H)-furanone as in Schemes 5.4.3 and 5.4.4. There is no evidence for the 2-butendial intermediate in Scheme 5.4.2.

Finally, because there is evidence for the production of hydrogen atoms in the flow tube, it is possible some of the features observed in both the mass and IR spectra can be assigned to additional bimolecular reactions beyond the hydrogen atom addition/elimination reactions that interconvert the furanones. As previously mentioned, at least some of the observed ion signal at m/z 28 can be assigned to ethylene and further confirmation of this assignment is the intense feature at 948.4 cm^{-1} in Fig. 5.4 and to a lesser extent in Fig. 5.5, assigned to $CH_2{=}CH_2(\nu_7)$ in Ar. Several pyrolysis studies have observed ethylene from heating acrolein to high temperatures [25]; one route to formation is by catalytic reaction [64] with H-atoms.[2] A more thorough discussion of acrolein decomposition is presented in Section 5.4.1.

The ions at m/z 40 in the right-panel of Fig. 5.3 at 1300 K are assigned to methylacetylene ($CH_3C{\equiv}CH$) at low temperatures and to allene ($CH_2{=}C{=}CH_2$) at even higher temperatures; however the source of these species remains a bit more elusive. The assignment of methylacetylene is confirmed by infrared spectroscopy at 1100 K, as shown in the left-hand panel of Fig. 5.6; allene is not detected until the reactor is at 1300 K (not shown). Direct

---

[2] $CH_2{=}CH\text{-}CHO + H \rightarrow [CH_2CH_2\text{-}CHO]^* \rightarrow CH_2{=}CH_2 + HCO \rightarrow CH_2{=}CH_2 + H + CO$

decarboxylation of 2(5H)-furanone to produce methylacetylene unimolecularly (Scheme 5.5.4 was calculated [149] to have a barrier to reaction of about 400 kJ mol^{-1}; assuming this barrier is accurate to within 20 kJ mol^{-1}, this route seems energetically prohibitive for the conditions studied here. A more energetically accessible channel could be H-atom addition to the starting material or to the open-chain form (4-oxo-3-butenal); the loss of CO_2 would produce allyl radical ($CH_2=CH-CH_2$), followed by loss of hydrogen atom to give $[CH_2=C=CH_2 \rightleftharpoons CH_3C{\equiv}CH]$.

Experimental evidence for the thermal decomposition mechanism of 2(3H)-furanone clearly favors the concerted reaction in Scheme 5.4.1, as previously reported by Xu *et al.* [154] and confirms predictions of more recent electronic structure calculations [149, 150]. Analogous to the liquid-phase stability, 2(5H)-furanone was shown to be more stable in the gas-phase than 2(3H)-furanone. Experimental evidence indicates that consumption of 2(5H)-furanone proceeds through two primary routes: through interconversion to 2(3H)-furanone by H-atom addition/elimination reactions, or ring opening to 4-oxo-3-butenal ($O=C=CH-CH_2-CHO$), and also in small part due to $H{-}C$ bond-scission to form 2-furanyloxy radical.

5.3   Pyrolysis of α-Angelica Lactone (5-methyl-2(3H)-Furanone)

The primary thermal decomposition products from α-angelica lactone (α-AL) detected by photoionization mass spectrometry (PIMS) and infrared spectroscopy are methyl vinyl ketone (MVK, $CH_3-CO-CH=CH_2$) and carbon monoxide; analogous to that reported by Xu *et al.* [154]. Figure 5.7 shows the resulting photoionization mass spectra (PIMS) observed at several reactor temperatures for a mixture of approximately 0.1% α-AL in helium. With the reactor held at 350 K, only the parent ion and the ^{13}C isotope are observed at m/z 98 and 99, respectively. The onset for decomposition is observed at about 1000 K with the appearance of m/z 70, assigned to methyl vinyl ketone. The small features at m/z 43 and 55 in the spectrum at 1000 K are assigned to dissociative photoionization of m/z 98 or MVK[3]

0.1% α–Angelica Lactone / He
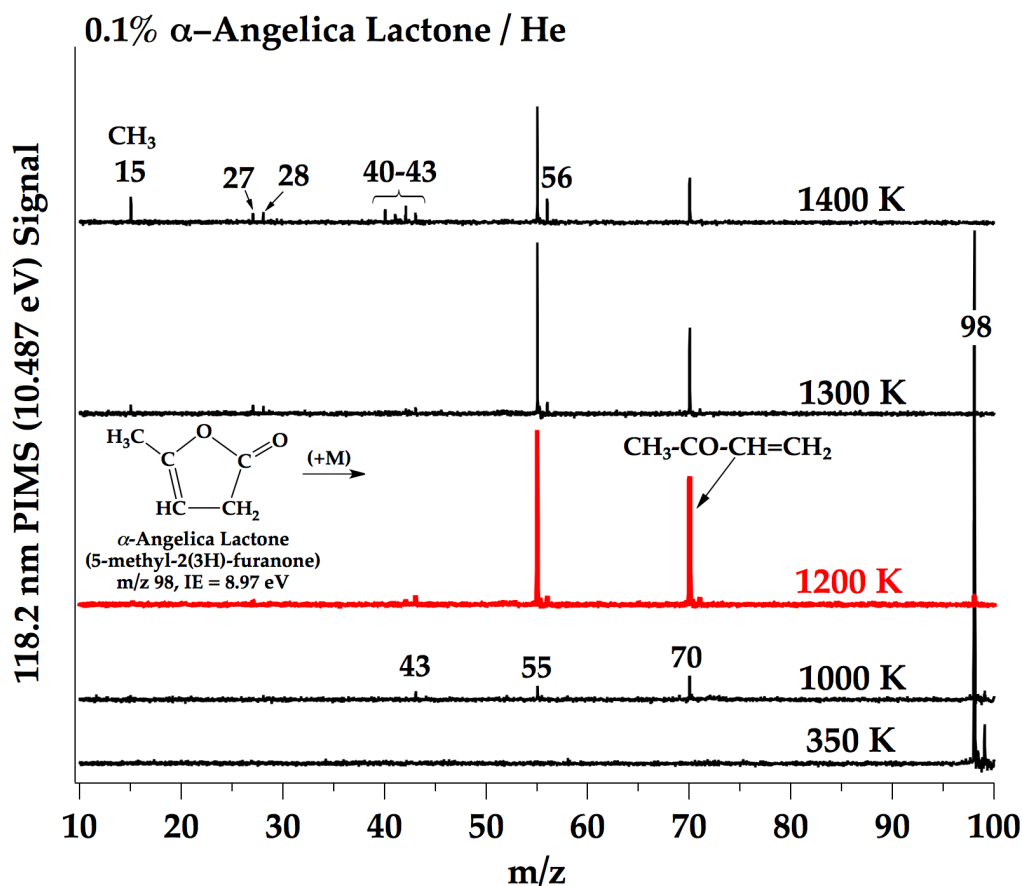
Figure 5.7: Product mass spectra of α-angelica lactone in a pulsed reactor at several reactor wall temperatures. Experimentally reported ionization energy by Czekner *et al.* [30]

(see Fig. 5.11 in Section 5.4.2).

By 1300 K, methyl vinyl ketone becomes thermally unstable and begins to decompose, breaking the weakest bond ($CH_3-C(O)CHCH_2$), producing CH_3 (m/z 15) and acryloyl (O=C-CH=CH$_2$) radicals.[4] Acryloyl radical further fragments to CO, H and HC≡CH within the hot reactor (see Chapter 4.2). Other possible decomposition routes for MVK are described in more detail in Section 5.4.2; in general, there are several observed products in the mass spectrum at 1400 K for α-AL that are consistent with the observed products in the decomposition of MVK up to 1500 K (see Fig. 5.11).

---

[3] ex. $C_5H_6O_2 + 118.2nm \rightarrow [C_5H_6O_2^+]^* \rightarrow (C_3H_3O^+ + CH_3CO)$ and $(C_3H_3O + CH_3CO^+)$

[4] $DH_{298}(CH_3-C(O)CHCH_2) = \Delta_f H_{298}(CH_3) + \Delta_f H_{298}(OCCHCH_2) - \Delta_f H_{298}(MVK) \approx 360$ kJ mol^{-1}

Recent electronic structure calculations of α-angelica lactone [149] report another plausible decomposition route is a hydrogen-shift from C3 to C2 followed by ring opening to 2-pentene-1,4-dione, as shown in Scheme 5.6.2.
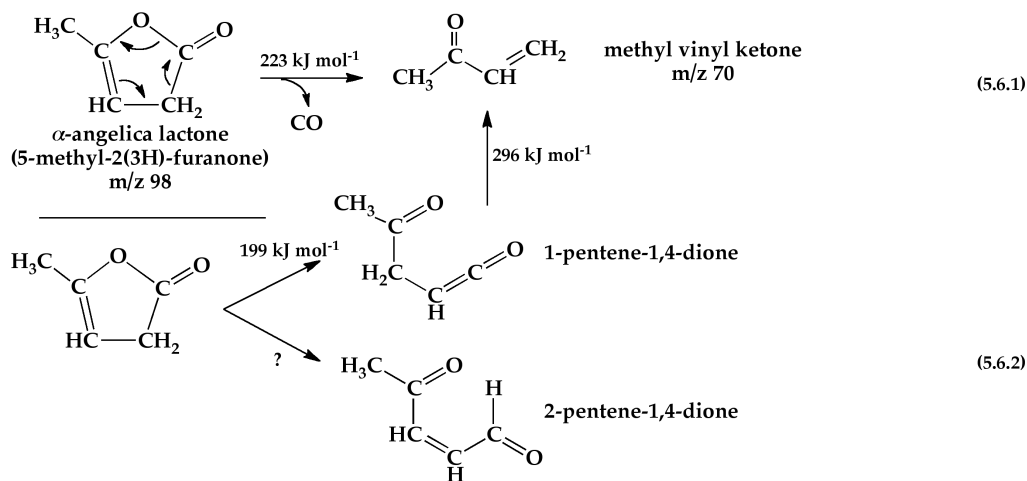
Scheme 5.6: Predicted lowest-energy decomposition pathways of α-angelica lactone (5-methyl-2(3H)-furanone) as calculated by Würmel and Simmie [149]; select reaction barriers included.

The evidence in the IR overwhelmingly points to methyl vinyl ketone as the dominant thermal product, as shown in Figs 5.8 and 5.9, and also Figs. C.5 through C.7 in Appendix C. Assignment of the infrared bands of the *syn*-periplanar and *anti*-periplanar conformers of MVK are based on a previous study in an Ar matrix [108]; a comparative table of frequencies are included in Table C.3 in Appendix C. Based on authentic samples of MVK in Ar, several combination bands and other features were also identified and are indicated in the spectra throughout. There is no evidence to suggest the pentene-dione intermediates in Schemes 5.6.2 and 5.6.3; they are either unable to survive the heated reactor, potentially decomposing as indicated, or this reaction pathway is not thermodynamically favorable at the conditions in the microreactor and instead most of the reaction proceeds through the concerted process in Scheme 5.6.1. It is possible α-AL could also interconvert to 5-methyl-2(5H)-furanone through this open-chain intermediate, similar to the interconversion mechanism proposed [149] between the unsubstituted compounds, as indicated in Scheme 5.7. Elimination of CO from
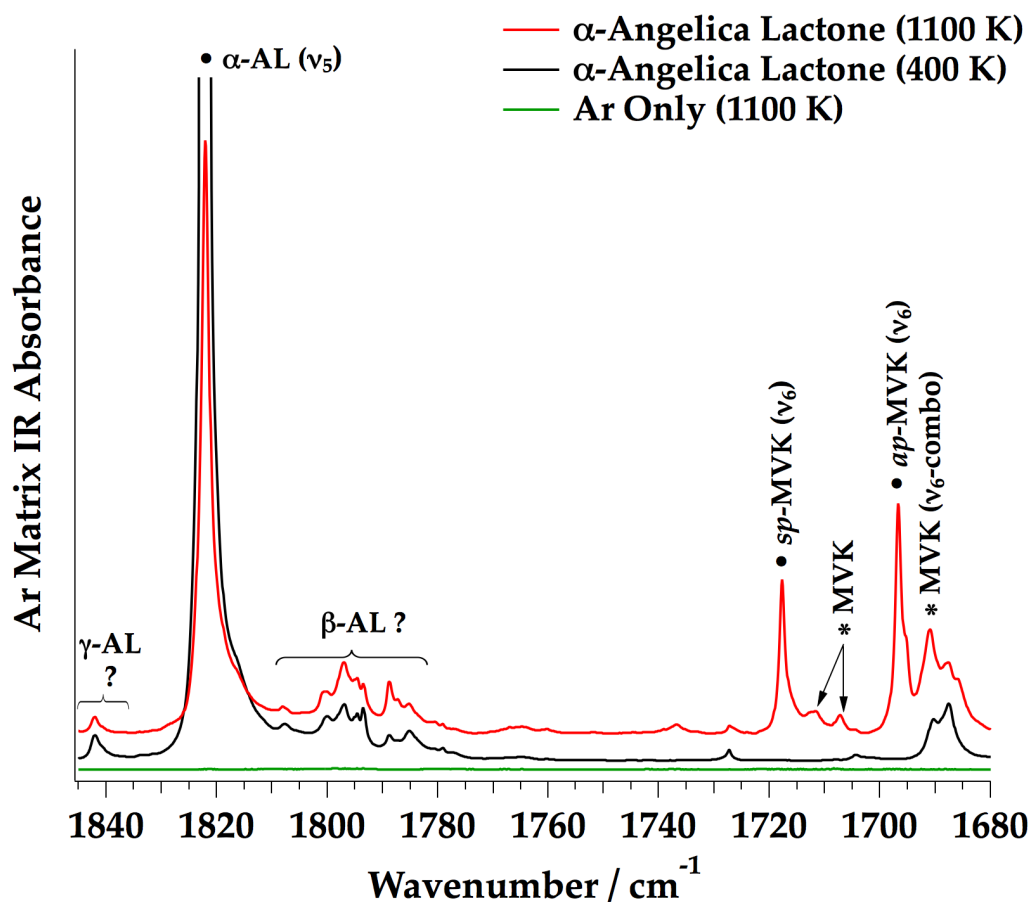
Figure 5.8: Infrared product spectrum of α-angelica lactone (α-AL) compared with α-AL deposited through reactor at 350 K. Methyl vinyl ketone (MVK) identified in an Ar matrix; features marked with (*) are not fundamentals of MVK, but are observed from authentic samples. Approximately 0.1% α-AL in Ar (3.5 mmol Ar deposited).

this species could also be a source of MVK.

Aside from methyl vinyl ketone, there are several features between 1785 and 1850 cm^{-1}, as shown in Fig. 5.8, which can be attributed to either the anharmonicity of α-AL (ν_5), similar to that observed for 2(5H)-furanone [19], or the other isomers of α-AL found in solution (as described in the experimental section). The ν(C=O) frequency for β-AL will likely less than α-AL [97], while ν(C=O) for γ-AL will be larger [53]; suggested assignments of these features are indicated in Fig. 5.8. Calculated harmonic frequencies [150] and vibrational assignments of α-angelica lactone in an argon matrix are included in Table C.6 of Appendix C.
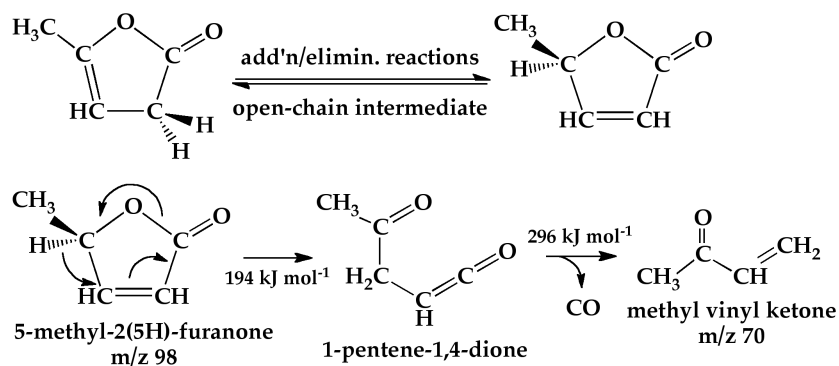
Scheme 5.7: Interconversion to β-angelica lactone (5-methyl-2(5H)-furanone) observed in Xu study [154]; this isomer could also be a potential source of methyl vinyl ketone [149].
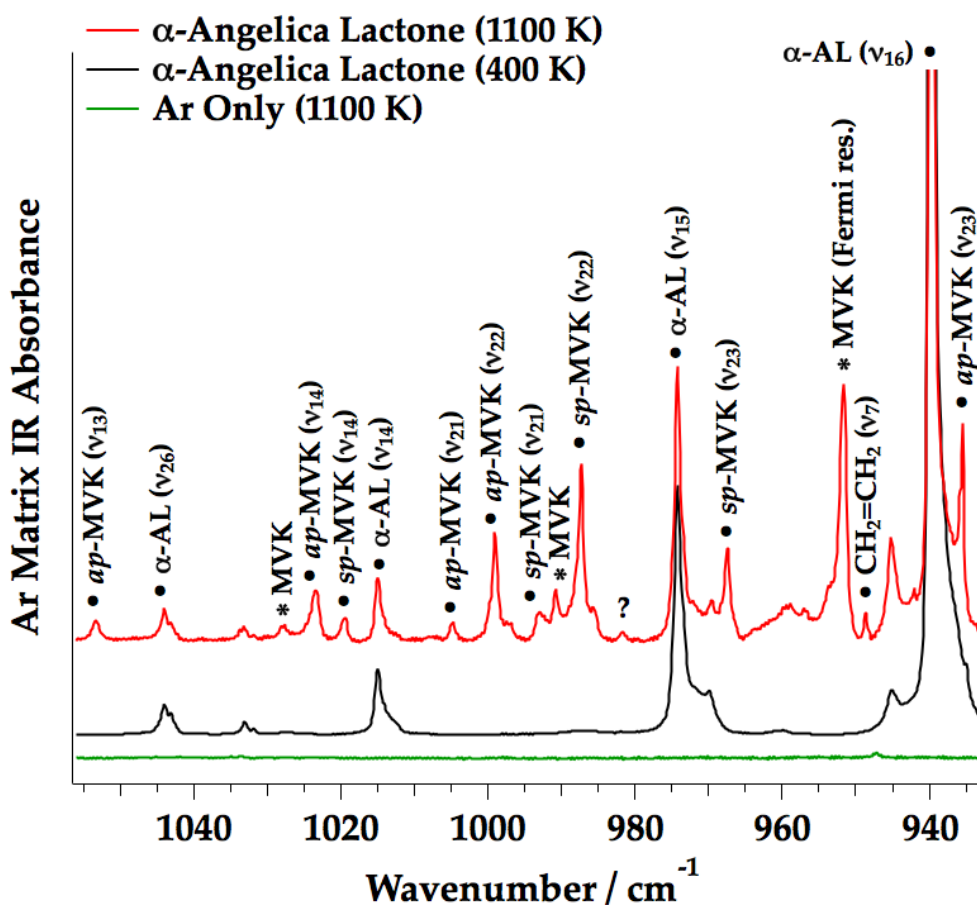
Figure 5.9: Infrared product spectrum of α-angelica lactone (α-AL); MVK identified in an Ar matrix; features marked with (*) are not fundamentals of MVK, but are observed from authentic samples. Approximately 0.1% α-AL in Ar.

5.4   Supporting Mechanisms

5.4.1   Pyrolysis of Acrolein (CH_2=CH-CHO) in the Microreactor

As described in Section 5.2, acrolein (2-propenal) is a dominant product in the pyrolysis of the furanones; for this reason, heating authentic samples of this species in the microreactor is important to identify any possible thermal products. Acrolein, the simplest α,β-unsaturated carbonyl, has also been detected in the atmosphere as a product of incomplete combustion [129]; one demonstrated method to its formation is CH radical reaction with acetaldehyde (CH_3-CHO) [46].
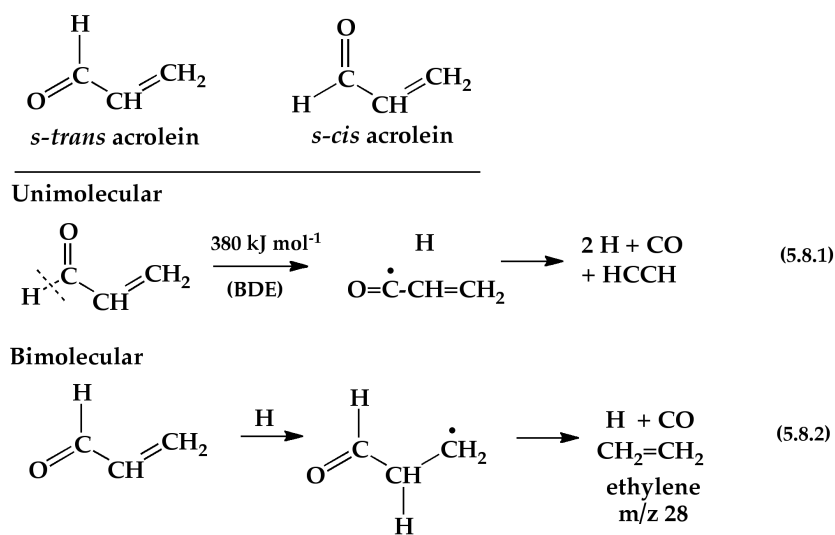
Scheme 5.8: Acrolein (CH_2=CH-CHO) has two possible conformers: *s-trans* and *s-cis*; the *s-trans* conformer is the most stable. Possible unimolecular and bimolecular decomposition pathways of acrolein.

Acrolein exists in two forms: *s-trans* or *s-cis*, as shown in Scheme 5.8, with the *s-trans* conformer being the most stable [16]. The weakest bond in acrolein is the aldehyde H−C bond; this was estimated by the bond homolysis reaction,[5] calculating the difference in enthalpies of formation between the product and reactants [15, 43]. Most kinetic mechanisms that include reactions of acrolein (for example [122] and [126]) do not include any unimolecular

---

[5] $DH_{298}(H-C(O)CHCH_2) = \Delta_f H_{298}(H) + \Delta_f H_{298}(OCCHCH_2) - \Delta_f H_{298}(acrolein) \approx 380$ kJ mol^{-1}
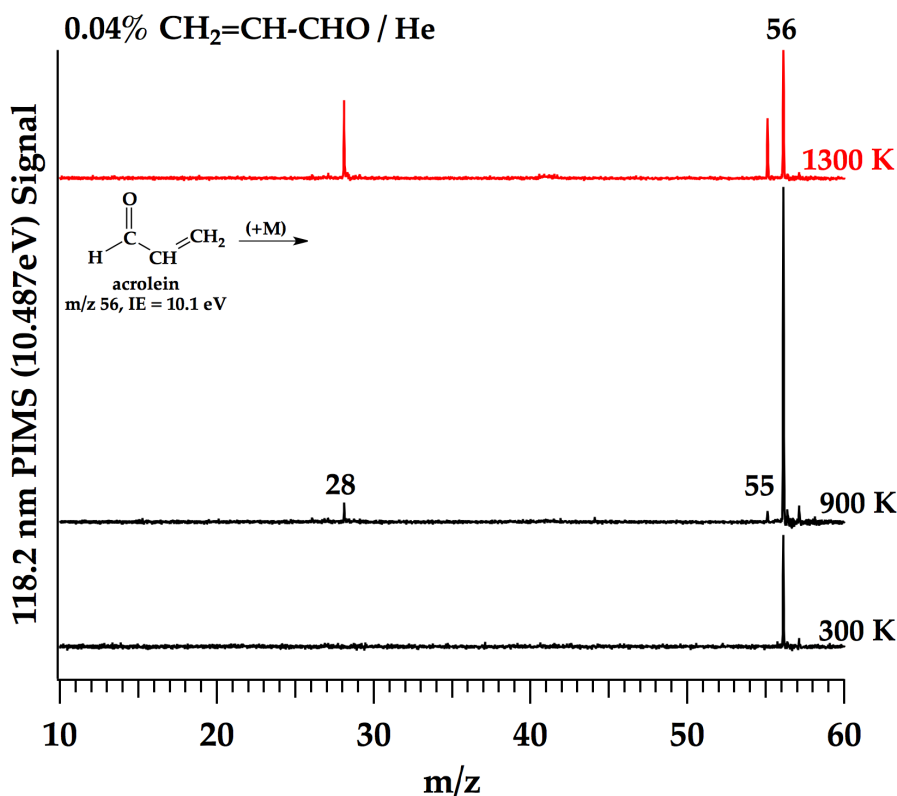
Figure 5.10: Reference mass spectra of dilute samples of acrolein in helium heated in the pulsed flow reactor up to 1300 K. Ions at m/z 28 and 55 assigned to ion fragments and are not thermal products.

decomposition schemes, simply because they will not be competitive reactions; instead they include radical addition or abstraction reactions of this species.

Since the weakest bond in acrolein is very large, at approximately 380 kJ mol^{-1}, one would guess the PIMS would show very little decomposition until much higher reactor temperatures. However, the mass spectra in Fig. 5.10 show that acrolein produces an ions at m/z 28 and m/z 55[6] at a very low temperature, approximately 900 K. Thermal formation of ethylene (m/z 28) at such a low temperature does not seem likely. It is possible that a $C_2H_4^+$ cation is formed by dissociative photoionization of acrolein (similar to formation of m/z 55), however this is also not intuitive given the ionizing photons are 0.023 eV *below* the ionization threshold for ethylene (10.487 eV for 9th harmonic of Nd:YAG vs. IE(CH_2CH_2)

---

[6] C_2H_3-CHO + 118.2nm $\rightarrow$ [C_2H_3-CHO$^+$]* $\rightarrow$ $C_3H_3O^+$ + H

= 10.51 eV [153]). One possibility for the formation of m/z 28 from vibrationally excited acrolein is a multi-photon process of the photoionization event. Acrolein readily absorbs in the 240−400 nm region [83] and absorption of a photon at 355 nm (3.5 eV) could excite acrolein to one of three low-lying excited-states [104]. Two-photon absorption processes are normally assumed to be rare contributors to the distribution of observed product ions in our photoionization mass spectrometer, however for acrolein this assumption may not be valid. Improved separation in the ionization region of the spectrometer of the 355 nm fundamental from the resulting 118.2 nm light may reduce these effects [82].

In addition to the possibility of dissociative ionization forming a cation at m/z 28, another potential source of ethylene is from reaction of acrolein with H-atoms, as shown in Scheme 5.8.2. Hydrogen atoms can add to the double bond of the precursor [64], forming an adduct which can then eliminate CO to give ethylene. Ethylene has been detected in other pyrolysis studies [25, 64] of acrolein, possibly due to hydrogen atom addition reactions.

When a 0.05% mixture of acrolein in argon was heated and deposited for IR detection, with the exception of several features in the IR that belong to the *s-cis* conformer of acrolein (see Table C.2 in Appendix C.3), little else grows in at temperatures up to 1300 K, indicating that the ions at m/z 28 do not correspond to a thermal source of ethylene, but rather are an artifact of the experiment. However, if acrolein is formed in the presence of a thermal source of hydrogen atoms (as in the decomposition of 2(3H)-furanone in Fig. 5.4), ethylene is observed in the IR.

5.4.2   Thermal Decomposition of Methyl Vinyl Ketone

Since methyl vinyl ketone (MVK, CH_3-CO-CH=CH_2) is the dominant product observed in the thermal cracking of α-angelica lactone, understanding the possible decomposition pathways of this species is necessary to interpret the high-temperature spectra. Cleavage of the CH_3−CO bond in MVK produces CH_3 and acryloyl (O=C-CH=CH_2) radicals; the lifetime of the acryloyl radical is too short to be detected, and by the reactor exit this species fragments

Bond Scission

$$CH_3-C(=O)-CH=CH_2 \longrightarrow O=\overset{\bullet}{C}-CH=CH_2 \longrightarrow CH=CH_2 \longrightarrow HC\equiv CH \quad (5.9.1)$$

methyl vinyl ketone
m/z 70 · CH₃ m/z 15 · acryloyl radical · CO · H acetylene

Tautomerization

$$CH_3-C(=O)-CH=CH_2 \longleftrightarrow CH_2=C(OH)-CH=CH_2 \longrightarrow CH_2=\overset{\bullet}{C}-OH \longrightarrow O=C=CH_2 \quad (5.9.2)$$

2-hydroxybutadiene · CH=CH₂ → HC≡CH · H · ketene m/z 42 · H
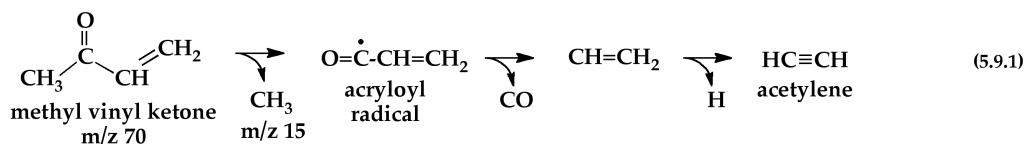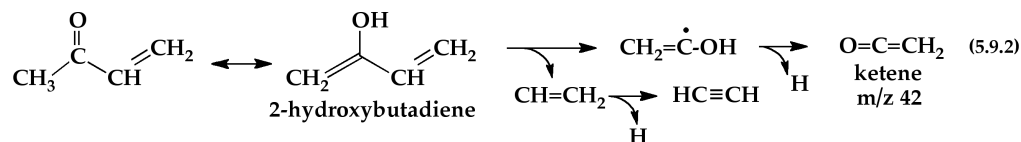
Scheme 5.9: Possible observed unimolecular decomposition pathways of methyl vinyl ketone.

to acetylene, hydrogen atom and carbon monoxide, as shown in Scheme 5.9.1. Another possible decomposition route of MVK is tautomerization to the enol, 2-hydroxybutadiene, as shown in Scheme 5.9.2. Tautomerization could produce acetylene, ketene and hydrogen atom. Product mass spectra of a heated 0.06% mixture of methyl vinyl ketone in helium, Fig. 5.11, show that the first sign of methyl radical (m/z 15) and ketene (m/z 42) is at about 1300 K. Ions at m/z 27, 43 and 55 are assigned to dissociative ionization of MVK and are not the result of thermal processes.

Decomposition through both channels produce H-atoms, which can then react with the starting material and produce additional species, as shown in Scheme 5.10. Infrared spectroscopy in an Ar matrix confirms the identity of m/z 52 as vinylacetylene (CH_2=CH-C≡CH), m/z 56 as a combination of acrolein and methylketene and m/z 40 as combination of methylacetylene and allene. Analogous to the pyrolysis experiments of α-angelica lactone, the source of m/z 40 as both methylacetylene and allene is not straightforward. A potential source is methyl radical addition to vinylacetylene, with loss of vinyl radical, producing a species at m/z 40.

In general, the pyrolysis products for methyl vinyl ketone observed at high temperatures are consistent with those observed in the high-temperature (> 1300 K) pyrolysis of α-angelica lactone.
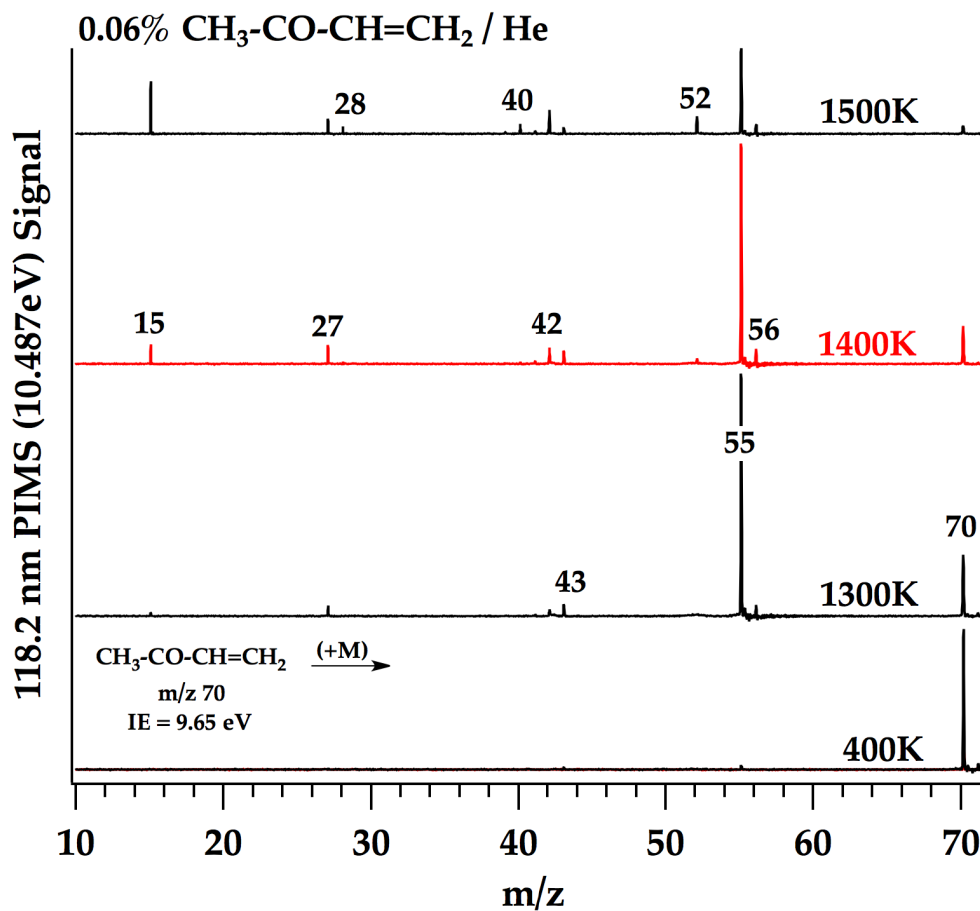
Figure 5.11: Product mass spectra of methyl vinyl ketone in a pulsed reactor at several reactor temperatures.
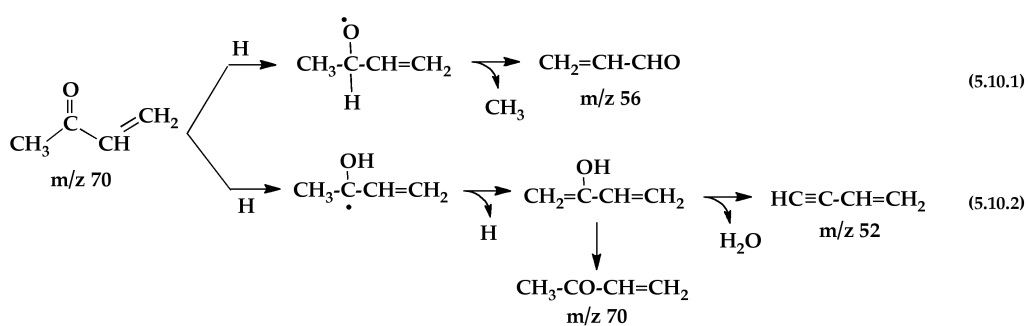
Scheme 5.10: Possible hydrogen-atom addition reactions to methyl vinyl ketone.

Bibliography

[1] H. Abe and K.M.T. Yamada. Spectroscopic identification of the CO-H_2O 2-1 cluster trapped in an argon matrix. Journal of Chemical Physics, 121(16):7803–7812, 22 October 2004.

[2] J. Alemán, V. del Solar, L. Cubo, A.G. Quiroga, and C.N. Ranninger. New reactions of anticancer-plantinum complexes and their intriguing behaviour under various experimental conditions. Dalton Transactions, 39:10601–10607, 2010.

[3] D.M. Alonso, S.G. Wettstein, and J.A. Dumesic. Gamma-valerolactone, a sustainable platform molecule derived from lignocellulosic biomass. Green Chemistry, 15(3):584–595, 2013.

[4] J.H. Arps, C.H. Chen, M.P. McCann, and I. Datskou. Ionization of organic molecules using coherent vacuum ultraviolet light. Applied Spectroscopy, 43(7):1211–1214, 1989.

[5] G.B. Bajracharya, P.S. Koranne, R.N. Nadaf, R.K.M. Gabr, K. Takenaka, S. Takizawa, and H. Sasai. Pd-catalyzed 5-*endo-trig*-type cyclization of β,γ-unsaturated carbonyl compounds: an efficient ring closing reaction to give γ-butenolides and 3-pyrrolin-2-ones. Chemical Communications, 46:9064–9066, 2010.

[6] C. Barckholtz, M.J. Fadden, and C.M. Hadad. Computational study of the mechanisms for the reaction of $O_2(^3\Sigma_g)$ with aromatic radicals. Journal of Physical Chemistry A, 103(40):8108–8117, 1999.

[7] J.R. Barker, N.F. Ortiz, J.M. Preses, L.L Lohr, A. Maranzana, P.J. Stimac, T.L. Nguyen, and T.J.D. Kumar. MultiWell-2011.1 Software. http://aoss.engin.umich.edu/multiwell/.

[8] D.L. Baulch, C.J. Cobos, R.A. Cox, C. Esser, P. Frank, Th. Just, J.A. Kerr, M.J. Pilling, J. Troe, R.W. Walker, and J. Warnatz. Evaluated kinetic data for combustion modelling. Journal of Physical and Chemical Reference Data, 21(3):411–734, 1992.

[9] J.A. Beukes, K.-M. Marstokk, and H. Møllendal. The structural and conformational properties of 2-methoxyfuran as studied by microwave spectroscopy and quantum chemical calculations. Journal of Molecular Structure, 567-568:19–27, 2001.

[10] G. Bieri, F. Burger, E. Heilbronner, and J.P. Maier. Valence ionization energies of hydrocarbons. Helvetica Chimica Acta, 60(7):2213–2233, 1977.

[11] J.B. Binder, J.J. Blank, A.V. Cefali, and R.T. Raines. Synthesis of furfural from xylose and xylan. ChemSusChem, 3(11):1268–1272, 2010.

[12] J.B. Binder, A.V. Cefali, J.J. Blank, and R.T. Raines. Mechanistic insights on the conversion of sugars into 5-hydroxymethylfurfural. Energy and Environmental Science, 3(6):765–771, 2010.

[13] J.B. Binder and R.T. Raines. Simple chemical transformation of lignocellulosic biomass into furans for fuels and chemicals. Journal of the American Chemical Society, 131(5):1979–1985, 2009.

[14] J.B. Binder and R.T. Raines. Fermentable sugars by chemical hydrolysis of biomass. Proceedings of the National Academy of Sciences, 107(10):4516–4521, March 2010.

[15] S.J. Blanksby and G.B. Ellison. Bond dissociation energies of organic molecules. Accounts of Chemical Research, 36(4):255–263, 2003.

[16] C.E. Blom, R.P. Müller, and Hs.H. Günthard. s-*trans* and s-*cis* acrolein: Trapping from thermal molecular beams and UV-induced isomerization in argon matrices. Chemical Physics Letters, 73(3):483–486, August 1980.

[17] J.A. Blush, P. Chen, R.T. Wiedmann, and M.G. White. Rotationally resolved threshold photoelectron spectrum of the methyl radical. Journal of Chemical Physics, 98(4):3557–3559, February 1993.

[18] C.W. Bock, Y.N. Panchenko, and S.V. Krasnoshchiokov. An *ab initio* prediction of structures and vibrational frequencies of high-energy rotamers of glyoxal and acrolein. Chemical Physics, 125:63–75, 1988.

[19] S. Breda, I. Reva, and R. Fausto. Molecular structure and vibrational spectra of 2(5H)-furanone and 2(5H)-thiophenone isolated in low temperature inert matrix. Journal of Molecular Structure, 887:75–86, 2008.

[20] A.L. Brown, D.C. Dayton, M.R. Nimlos, and J.W. Daily. Characterization of biomass pyrolysis vapors with molecular beam, single photon ionization time-of-flight mass spectrometry. Chemosphere, 42:663–669, 2001.

[21] R.C. Brown. Biorenewable Resources: Engineering New Products from Agriculture, chapter 3, pages 59–73. Iowa State Press, Ames, IA, 2003.

[22] H.J. Brownlee and C.S. Miner. Industrial development of furfural. Industrial and Engineering Chemistry, 40(2):201–204, February 1948.

[23] O.S.L. Bruinsma, P.J.J. Tromp, H.J.J. de Sauvage Nolting, and J.A. Moulijn. Gas phase pyrolysis of coal-related aromatic compounds in a coiled tube flow reactor 2. Heterocyclic compounds, their benzo and dibenzo derivatives. Fuel, 67(3):334–340, March 1988.

[24] D. Casarini, L. Lunazzi, G. Placucci, and A. Venturini. ESR detection and *ab initio* computation of the two rotational barriers in (aryloxy)methyl radicals. Journal of Organic Chemistry, 56(1):414–417, 1991.

[25] W.S. Chin, C.Y. Mok, and H.H. Huang. Thermal decomposition of isomeric nitropropenes: A photoelectron spectroscopic study. Journal of the American Chemical Society, 112(6):2053–2056, March 1990.

[26] E. Christensen, J. Yanowitz, M. Ratcliff, and R.L. McCormick. Renewable oxygenate blending effects on gasoline properties. Energy and Fuels, 25:4723–4733, 2011.

[27] T.A. Cool, K. Nakajima, T.A. Mostefaoui, F. Qi, A. McIlroy, P.R. Westmoreland, M.E. Law, L. Poisson, D.S. Peterka, and M. Ahmed. Selective detection of isomers with photoionization mass spectrometry for studies of hydrocarbon flame chemistry. Journal of Chemical Physics, 119(16):8356–8365, October 2003.

[28] T.A. Cool, K. Nakajima, C.A. Taatjes, A. McIlroy, P.R. Westmoreland, M.E. Law, and A. Morel. Studies of a fuel-rich propane flame with photoionization mass spectrometry. Proceedings of the Combustion Institute, 30:1681–1688, 2005.

[29] T.A. Cool, J. Wang, K. Nakajima, C.A. Taatjes, and A. McIlroy. Photoionization cross sections for reaction intermediates in hydrocarbon combustion. International Journal of Mass Spectrometry, 247:18–27, 2005.

[30] J. Czekner, C.A. Taatjes, D.L. Osborn, and G. Meloni. Absolute photoionization cross-sections of selected furanic and lactonic potential biofuels. International Journal of Mass Spectrometry, 348:39–46, 2013.

[31] J.W. Daily. Uncertainty and statistical data analysis. Personal communication, November 2012.

[32] J. Dannacher, J.-P. Flamme, J.-P. Stadelmann, and J. Vogt. Unimolecular fragmentations of internal energy selected 1,3-butadiene cations. Chemical Physics, 51(2):189–195, 1980.

[33] E. de Jong, T. Vijlbrief, R. Hijkoop, G.-J.M Gruter, and J.C. van der Waal. Promising results with YXY Diesel components in an ESC test cycle using a PACCAR Diesel engine. Biomass and Bioenergy, 36:151–159, 2012.

[34] C. Di Blasi, C. Branca, and A. Galgano. Biomass screening for the production of furfural via thermal decomposition. Industrial and Engineering Chemistry Research, 49(6):2658–2671, 2010.

[35] W. Dianxun, L. Sheng, W. Dong, and L. Ying. Application of an He I photoelecton spectroscopic (UPS) technique to the kinetic study of chemical reactions. Determination of the kinetic parameters of the conversion reaction of 2(3H) furanone to 2(5H) furanone. Journal of Electron Spectroscopy and Related Phenomena, 70:173–178, 1994.

[36] J.R. Durig and T.S. Little. Conformational barriers to internal rotation and vibrational assignment of methyl vinyl ketone. Journal of Chemical Physics, 75(8):3660–3668, October 1981.

[37] S. Dutta, S. De, B. Saha, and Md.I. Alam. Advances in conversion of hemicellulosic biomass to furfural and upgrading to biofuels. Catalysis Science and Technology, 2:2025–2036, 2012.

[38] M. Evans and C.Y. Ng. Rotationally resolved pulsed field ionization photoelectron study of CO^+ ($X^2\Sigma^+$, $v^+ = 0-42$) in the energy range of 13.98–21.92 eV. Journal of Chemical Physics, 111(19):8879–8891, November 1999.

[39] D. Fulle, A. Dib, J.H. Kiefer, Q. Zhang, J. Yao, and R.D. Kern. Pyrolysis of furan at low pressures: Vibrational relaxation, unimolecular dissociation, and incubation times. Journal of Physical Chemistry A, 102(38):7480–7486, 1998.

[40] B. Gans, L.A. Vieira Mendes, S. Boyé-Péronne, S. Douin, G. Garcia, H. Soldi-Lose, B.K. Cunha de Miranda, C. Alcaraz, N. Carrasco, P. Pernot, and D. Gauyacq. Determination of the absolute photionization cross sections of CH_3 and I produced from a pyrolysis source, by combined synchrotron and vacuum ultraviolet laser studies. Journal of Physical Chemistry A, 114(9):3237–3246, November 2010.

[41] H. Gao, Y.T. Xu, L. Yang, C.-S. Lam, H.L. Wang, J.A. Zhou, and C.Y. Ng. High-resolution threshold photoelectron study of the propargyl radical by the vacuum ultraviolet laser velocity-map imaging method. Journal of Chemical Physics, 135(22):224304, 2011.

[42] F.M.A. Geilen, B. Engendahl, A. Harwardt, W. Marquardt, J. Klankermayer, and W. Leitner. Selective and flexible transformation of biomass-derived platform chemicals by a multifunctional catalytic system. Agnewandte Chemie International Edition, 49:5510–5514, 2010.

[43] C.F. Goldsmith, G.R. Magoon, and W.H. Green. Database of small molecule thermochemistry for combustion. Journal of Physical Chemistry A, 116:9033–9057, 2012.

[44] L.D. Gomez, C.G. Steele-King, and S.J. McQueen-Mason. Sustainable liquid biofuels from biomass: the writing's on the walls. New Phytologist, 178:473–485, 2008.

[45] F. Goulay, A. Derakhshan, E. Maher, A.J. Trevitt, J.D. Savee, A.M. Scheer, D.L. Osborn, and C.A. Taatjes. Formation of dimethylketene and methacrolein by reaction of the CH radical with acetone. Physical Chemistry Chemical Physics, 15:4049–4058, 2013.

[46] F. Goulay, A.J. Trevitt, J.D. Savee, J. Bouwman, D.L. Osborn, C.A. Taatjes, K.R. Wilson, and S.R. Leone. Product detection of the CH radical reaction with acetaldehyde. Journal of Physical Chemistry A, 116:6091–6106, 2012.

[47] M.A. Grela, V.T. Amorebieta, and A.J. Colussi. Very low pressure pyrolysis of furan, 2-methylfuran, and 2,5-dimethylfuran. The stability of the furan ring. Journal of Physical Chemistry, 89(1):38–41, 1985.

[48] G.-J. Gruter and E. de Jong. Furanics: novel fuel options from carbohydrates. Biofuels Technology, 1:11–17, 2009.

[49] Q. Guan, K.N. Urness, T.K. Ormond, G.B. Ellison, and J.W. Daily. The properties of a microreactor for the study of the unimolecular decomposition of large molecules. International Reviews in Physical Chemistry, to be submitted, 2014.

[50] E.I. Gürbüz, S.G. Wettstein, and J.A. Dumesic. Conversion of hemicellulose to furfural and levulinic acid using biphasic reactors with alkylphenol solvents. ChemSusChem, 5(2):383–387, 2012.

[51] Y. Hamada, Y. Nishimura, and M. Tsuboi. Infrared spectrum of *trans*-acrolein. Chemical Physics, 100(3):365–375, December 1985.

[52] P. Haro, P. Ollero, A.L. Villanueva Perales, and F. Vidal-Barrero. Potential routes for thermochemical biorefineries. Biofuels, Bioproducts and Biorefining, 7:551–572, 2013.

[53] J. Haslouin and F. Rouessac. Preparation of α, β, and γ-methylene γ-butyrolactones. Tetrahedron Letters, 17(50):4651–4654, 1976.

[54] N.R. Hore and D.K. Russell. The thermal decomposition of 5-membered rings: A laser pyrolysis study. New Journal of Chemistry, 28:606–613, 2004.

[55] I.T. Horváth, H. Mehdi, V. Fábos, L. Boda, and L.T. Mika. γ-Valerolactone−a sustainable liquid for energy and carbon-based chemicals. Green Chemistry, 10:238–242, 2008.

[56] J.M. Hudzik and J.W. Bozzelli. Structure and thermochemical properties of 2-methoxyfuran, 3-methoxyfuran, and their carbon-centered radicals using computational chemistry. Journal of Physical Chemistry A, 114(30):7984–7995, 2010.

[57] J.C. Ianni. Kintecus for Windows, Version 5.20. www.kintecus.com, accessed March 25th, 2014.

[58] M.W. Jarvis, J.W. Daily, H.-H. Carstensen, A.M. Dean, S. Sharma, D.C. Dayton, D.J. Robichaud, and M.R. Nimlos. Direct detection of products from the pyrolysis of 2-phenethyl phenyl ether. Journal of Physical Chemistry A, 115(4):428–438, 2011.

[59] E.B. Jochnowitz, X. Zhang, M.R. Nimlos, B.A. Flowers, J.F. Stanton, and G.B. Ellison. Infrared spectrum of the propargyl peroxyl radical, $HC\equiv C\text{-}CH_2OO$ $\tilde{X}$ ^2A". Journal of Physical Chemistry A, 114(3):1498–1507, 2010.

[60] D.E. Johnstone and J.R. Sodeau. Photochemistry of the matrix-isolated α, β-unsaturated aldehydes acrolein, methacrolein and crotonaldehyde at 4.2 K. Journal of the Chemical Society-Faraday Transactions, 88(3):409–415, 1992.

[61] K.V. Jovan Jose, S.R. Gadre, K. Sundararajan, and K.S. Viswanathan. Effect of matrix on IR frequencies of acetylene and acetylene-methanol complex: Infrared matrix isolation and *ab initio* study. Journal of Chemical Physics, 127:104501, 2007.

[62] J. Kim, T.K. Ormond, K.N. Urness, J.W. Daily, M.R. Nimlos, M. Ahmed, A. Golan, J.F. Stanton, J. Gazaille, T. Sammakia, and G.B. Ellison. Organic radicals in pyrolysis of furans and biomass-based fuels. To be submitted, 2013.

[63] D. Klapstein, C.D. MacPherson, and R.T. O'Brien. The photoelectron spectra and electronic structure of 2-carbonyl furans. Canadian Journal of Chemistry, 68(5):747–754, May 1990.

[64] S. Koda, K. Nakamura, T. Hoshino, and T. Hikita. Reaction of hydrogen atoms with acrylaldehyde. Bulletin of the Chemical Society of Japan, 51(4):957–962, April 1978.

[65] D.W. Kohn, H. Clauberg, and P. Chen. Flash pyrolysis nozzle for generation of radicals in a supersonic jet expansion. Review of Scientific Instruments, 63(8):4003–4005, August 1992.

[66] K. Kohse-Höinghaus, P. Oßwald, T.A. Cool, T. Kasper, N. Hansen, F. Qi, C.K. Westbrook, and P.R. Westmoreland. Biofuel combustion chemistry: From ethanol to biodiesel. Agnewandte Chemie International Edition, 49:3572–3597, 2010.

[67] L.N. Krasnoperov, E.N. Chesnokov, H. Stark, and A.R. Ravishankara. Unimolecular dissociation of formyl radical, HCO → H + CO, studied over 1−100 bar pressure range. Journal of Physical Chemistry A, 108(52):11526–11536, 2004.

[68] A.H. Kung, J.F. Young, and S.E. Harris. Generation of 1182-$\mathring{A}$ radiation in phase-matched mixtures of inert gases. Applied Physics Letters, 22(6):301–302, March 1973.

[69] A.H. Kung, J.F. Young, and S.E. Harris. Erratum: Generation of 1182-$\mathring{A}$ radiation in phase-matched mixtures of inert gases. Applied Physics Letters, 28(4):239, February 1976.

[70] J.-P. Lange, R. Price, P.M. Ayoub, J. Louis, L. Petrus, L. Clarke, and H. Gosselink. Valeric biofuels: A platform of cellulosic transportation fuels. Agnewandte Chemie, 122:4581–4585, 2010.

[71] J-P. Lange, E. van der Heide, J. van Buijtenen, and R. Price. Furfural−a promising platform for lignocellulosic biofuels. ChemSusChem, 5:150–166, 2012.

[72] K.-C. Lau, Y. Liu, and L.J. Butler. Probing the barrier for $CH_2CHCO \rightarrow CH_2CH + CO$ by the velocity map imaging method. Journal of Chemical Physics, 123(5):054322, 2005.

[73] K.-C. Lau and C.-Y. Ng. Benchmarking state-of-the-art *ab initio* thermochemical predictions with accurate pulsed-field ionization photoion-photoelectron measurements. Accounts of Chemical Research, 39(11):823–829, 2006.

[74] G. Li, N. Li, Z. Wang, C. Li, A. Wang, X. Wang, Y. Cong, and T. Zhang. Synthesis of high-quality diesel with furfural and 2-methylfuran from hemicellulose. ChemSusChem, 5:1958–1966, 2012.

[75] S.-S. Liaw, Z. Wange, P. Ndegwa, C. Frear, S. Ha, C.-Z. Li, and M. Garcia-Perez. Effect of pyrolysis temperature on the yield and properties of bio-oils obtained from the auger pyrolysis of Douglas Fir wood. Journal of Analytical and Applied Pyrolysis, 93:52–62, 2012.

[76] D.R. Lide, editor. CRC Handbook of Chemistry and Physics. CRC Press, 1992.

[77] A. Lifshitz, M. Bidani, and S. Bidani. Thermal reactions of cyclic ethers at high temperatures. 3. Pyrolysis of furan behind reflected shocks. Journal of Physical Chemistry, 90(21):5373–5377, 1986.

[78] A. Lifshitz, C. Tamburu, and R. Shashua. Decomposition of 2-methylfuran. Experimental and modeling study. Journal of Physical Chemistry A, 101(6):1018–1029, 1997.

[79] A. Lifshitz, C. Tamburu, and R. Shashua. Thermal decomposition of 2,5-dimethylfuran. Experimental results and computer modeling. Journal of Physical Chemistry A, 102(52):10655–10670, 1998.

[80] R. Liu, X. Zhou, and L. Zhai. Theoretical investigation of unimolecular decomposition channels of furan. Journal of Computational Chemistry, 19(2):240–249, 1998.

[81] R. Liu, X. Zhou, and T. Zuo. The pyrolysis mechanism of furan revisited. Chemical Physics Letters, 325(4):457–464, July 2000.

[82] N.P. Lockyer and J.C. Vickerman. Single photon ionisation mass spectrometry using laser-generated vacuum ultraviolet photons. Laser Chemistry, 17(3):139–159, 1997.

[83] I. Magneron, R. Thévenet, A. Mellouki, G. Le Bras, G.K. Moortgat, and K. Wirtz. A study of the photolysis and OH-initiated oxidation of acrolein and *trans*-crotonaldehyde. Journal of Physical Chemistry A, 106(11):2526–2537, 2002.

[84] P. Masclet and G. Mouvier. Study of conjugated ethylenic aldehydes and ketones using photoelectron spectrometry. Journal of Electron Spectroscopy and Related Phenomena, 14(2):77–97, 1978.

[85] E. Mayer and E.R. Grant. Double-resonance spectroscopy of the high Rydberg states of HCO. I. A precise determination of the adiabatic ionization potential. Journal of Chemical Physics, 103(24):10513–10519, December 1995.

[86] T.E. McKone, W.W. Nazaroff, P. Berck, M Auffhammer, T. Lipman, M.S. Torn, E. Masanet, A. Lobscheid, N. Santero, U. Mishra, A. Barrett, M. Bomberg, K. Fingerman, C. Scown, B. Strogen, and A. Horvath. Grand challenges for life-cycle assessment of biofuels. Environmental Science and Technology, 45:1751–1756, 2011.

[87] D. McNaughton and R.J. Suffolk. The production and photoelectron spectrum of propa-1,2-dien-3-one, C_3H_2O. Journal of Chemical Research, Synopses, (1):32, 1985.

[88] M.S. Mettler, D.G. Vlachos, and P.J. Dauenhauer. Top ten fundamental challenges of biomass pyrolysis for biofuels. Energy and Environmental Science, 5:7797–7809, 2012.

[89] L.A. Montero, R. Gonzáles-Jonte, L.A. Díaz, and J.R. Alvarez-Idaboy. Theoretical model of furan and 2-furancarboxaldehyde. The molecular structure and vibrational spectra, including isotopic effects. Journal of Physical Chemistry, 98(22):5607–5613, 1994.

[90] C. E. Moore. Atomic energy levels. Technical report, National Bureau of Standards, Washington, DC 20402, 1971.

[91] J.-P. Morizur, J. Mercier, and M. Sarraf. 2-Substituted-2,3-dihydro-4*H*-pyrans: Competition between 'retro Diels-Alder' fragmentation and substituent loss. Organic Mass Spectrometry, 17(7):327–330, 1982.

[92] M.F.R. Mulcahy, B.G. Tucker, D.J. Williams, and J.R. Wilmshurst. Decomposition and rearrangement of free radicals from alkyl phenyl ethers. Chemical Communications, (23):609–610, November 1965.

[93] M.F.R. Mulcahy, B.G. Tucker, D.J. Williams, and J.R. Wilmshurst. Reactions of free radicals with aromatic compounds in the gaseous phase. III. Kinetics of the reaction of methyl radicals with anisole (methoxybenzene). Australian Journal of Chemistry, 20:1155–1171, 1967.

[94] J.-A. Näsman and K.G. Pensar. An improved one-pot preparation of 2-furanones. Synthesis, 8:786–788, August 1985.

[95] NIST. Combining uncertainty components. `http://physics.nist.gov/cuu/Uncertainty/combination.html`, Last accessed 2/10/2013.

[96] B.H. Niu, Y. Bai, and D.A. Shirley. High resolution photoelectron spectroscopy and femtosecond intramolecular dynamics of H_2CCO^+ and D_2CCO^+. Journal of Chemical Physics, 99(4):2520–2532, August 1993.

[97] R.A. Nyquist, H.A. Fouchea, G.A. Hoffman, and D.L. Hasha. Infrared study of β-propiolactone in various solvent systems and other lactones. Applied Spectroscopy, 45(5):860–867, 1991.

[98] J.F. Ogilvie, S.-L. Chou, M.-Y. Lin, and B.-M. Cheng. Mid-infrared spectra of methane dispersed in solid neon and argon. Vibrational Spectroscopy, 57:196–206, 2011.

[99] P.P. Organ and J.C. Mackie. Kinetics of pyrolysis of furan. Journal of the Chemical Society-Faraday Transactions, 87(6):815–823, 1991.

[100] A.C. O'Sullivan. Cellulose: the structure slowly unravels. Cellulose, 4:173–207, 1997.

[101] S.T. Pratt, P.M. Dehmer, and J.L. Dehmer. Zero-kinetic-energy photoelectron-spectroscopy from the $\tilde{A}$ ^1A_u state of acetylene: Renner−Teller interactions in the *trans*-bending vibration of $C_2H_2^+$ $\tilde{X}$ $^2\Pi_u$. Journal of Chemical Physics, 99(9):6233–6244, Nov 1 1993.

[102] Reaction Design. *Chemkin-Pro 15113*. San Diego, CA, 2012.

[103] J.R. Regalbuto. The sea change in U.S. biofuels' funding: From cellulosic ethanol to green gasoline. Biofuels, Bioproducts and Biorefining, 5:495–504, 2011.

[104] M. Reguero, M. Olivucci, F. Bernardi, and M.A. Robb. Excited-state potential surface crossings in acrolein: A model for understanding the photochemistry and photophysics of α,β-enones. Journal of the American Chemical Society, 116(5):2103–2114, 1994.

[105] H.W. Rohrs, C.T. Wickham-Jones, G.B. Ellison, D. Berry, and B.M. Argrow. Fourier transform infrared absorption spectroscopy of jet-cooled radicals. Review of Scientific Instruments, 66(3):2430–2441, March 1995.

[106] Y. Román-Leshkov, C.J. Barrett, Z.Y. Liu, and J.A. Dumesic. Production of dimethyl-furan for liquid fuels from biomass-derived carbohydrates. Nature, 447:982–985, June 2007.

[107] J.A.R. Samson and J.L. Gardner. Partial photoionization cross-sections and branching ratios of CO from 750 to 304 $\mathring{A}$. Journal of Electron Spectroscopy and Related Phenomena, 8:35–44, 1976.

[108] K. Sankaran and Y.-P. Lee. Theoretical calculations and infrared absorption spectra of *ap*- and *sp*-methyl vinyl ketone in solid Ar. Journal of Physical Chemistry A, 106(7):1190–1195, 2002.

[109] N. Savage. The ideal biofuel. Nature, 474:S9–S11, June 2011.

[110] J.D. Savee, S. Soorkia, O. Welz, T.M. Selby, C.A. Taatjes, and D.L. Osborn. Absolute photoionization cross-section of the propargyl radical. Journal of Chemical Physics, 136:134307, 2012.

[111] A.M. Scheer, C. Mukarakate, D.J. Robichaud, G.B. Ellison, and M.R. Nimlos. Radical chemistry in the thermal decomposition of anisole and deuterated anisoles: An investigation of aromatic growth. Journal of Physical Chemistry A, 114(34):9043–9056, 2010.

[112] A.M. Scheer, C. Mukarakate, D.J. Robichaud, M.R. Nimlos, H.-H. Carstensen, and G.B. Ellison. Unimolecular thermal decomposition of phenol and d_5-phenol: Direct observation of cyclopentadiene formation via cyclohexadienone. Journal of Chemical Physics, 136:044309, 2012.

[113] A.M. Scheer, C. Mukarakate, D.J. Robichaud, M.R. Nimlos, and G.B. Ellison. Thermal decomposition mechanisms of the methoxyphenols: Formation of phenol, cyclopenta-dienone, vinylacetylene and acetylene. Journal of Physical Chemistry A, 115:13381–13389, 2011.

[114] A.M. Schulenburg, M. Meisinger, P.P. Radi, and F. Merkt. The formaldehyde cation: Rovibrational energy level structure and Coriolis interaction near the adiabatic ionization threshold. Journal of Molecular Structure, 250(1):44–50, July 2008.

[115] S.M. Sen, J.B. Binder, R.T. Raines, and C.T. Maravelias. Conversion of biomass to sugars via ionic liquid hydrolysis: Process synthesis and economic evaluation. Biofuels, Bioproducts and Biorefining, 6:444–452, 2012.

[116] K. Sendt, G.B. Bacskay, and J.C. Mackie. Pyrolysis of furan: ab Initio quantum chemical and kinetic modeling studies. Journal of Physical Chemistry A, 104(9):1861–1875, 2000.

[117] R. Signorell and F. Merkt. The first rotationally resolved spectrum of CH_4^+. Journal of Chemical Physics, 110(5):2309–2311, February 1999.

[118] J.M. Simmie and W.K. Metcalfe. *ab initio* study of the decomposition of 2,5-dimethylfuran. Journal of Physical Chemistry A, 115:8877–8888, 2011.

[119] J.M. Simmie, K.P. Somers, K. Yasunaga, and H.J. Curran. A quantum chemical study of the abnormal reactivity of 2-methoxyfuran. International Journal of Chemical Kinetics, 45:531–541, 2013.

[120] J.M. Simmie and J. Würmel. Harmonising production, properties and environmental consequences of liquid transport fuels from biomass - 2,5-dimethylfuran as a case study. ChemSusChem, 6(1):36–41, January 2013.

[121] K.P. Somers, J.M. Simmie, F. Gillespie, U. Burke, J. Connolly, W.K. Metcalfe, F. Battin-Leclerc, P. Dirrenberger, O. Herbinet, P.-A. Glaude, and H.J. Curran. A high temperature and atmospheric pressure experimental and detailed chemical kinetic modeling study of 2-methyl furan oxidation. Proceedings of the Combustion Institute, 34:225–232, 2013.

[122] K.P. Somers, J.M. Simmie, F. Gillespie, C. Conroy, G. Black, W.K. Metcalfe, F. Battin-Leclerc, P. Dirrenberger, O. Herbinet, P.-A. Glaude, P. Dagaut, C. Togbé, K. Yasunaga, R.X. Fernandes, C. Lee, R. Tripathi, and H.J. Curran. A comprehensive experimental and detailed chemical kinetic modelling study of 2,5-dimethylfuran pyrolysis and oxidation. Combustion and Flame, 160:2291–2318, 2013.

[123] C.A. Taatjes, D.L. Osborn, T.M. Selby, G. Meloni, H.Y. Fan, and S.T. Pratt. Absolute photoionization cross-section of the methyl radical. Journal of Physical Chemistry A, 112(39):9336–9343, 2008.

[124] J.K. Terlouw, W. Heerma, J.L. Holmes, and P.C. Burgers. Structure and formation of gaseous $[C_4H_6O]^{+\cdot}$ ions. 1—The enolic ions $[CH_2=C(OH)-CH=CH_2]^{+\cdot}$ and $[CH_2=CH-CH=CH(OH)]^{+\cdot}$ and their relationship with their keto counterparts. Organic Mass Spectrometry, 15(11):582–586, November 1980.

[125] O. Thorstad, K. Undheim, B. Cederlund, and A.-B. Hörnfeldt. Ionisation potentials in tautomeric analysis of 2-hydroxy derivatives of thiophenes, selenophenes, and furans. Acta Chemica Scandinavica B, 29:647–651, 1975.

[126] Z. Tian, T. Yuan, R. Fournet, P.-A. Glaude, B. Sirjean, F. Battin-Leclerc, K. Zhang, and F. Qi. An experimental and kinetic investigation of premixed furan/oxygen/argon flames. Combustion and Flame, 158:756–773, 2011.

[127] I.V. Tokmakov, G.-S. Kim, V.V. Kislov, A.M. Mebel, and M.C. Lin. The reaction of phenyl radical with molecular oxygen: A G2M study of the potential energy surface. Journal of Physical Chemistry A, 109(27):6114–6127, 2005.

[128] R. S. Tranter, R. Sivaramakrishnan, N. Srinivasan, and K. Brezinsky. Calibration of reaction temperatures in a very high pressure shock tube using chemical thermometers. International Journal of Chemical Kinetics, 33:722–731, 2001.

[129] E.C. Tuazon, S.M. Aschmann, N. Nishino, J. Arey, and R. Atkinson. Kinetics and products of the OH radical-initiated reation of 3-methyl-2-butenal. Physical Chemistry Chemical Physics, 7:2298–2304, 2005.

[130] C.O. Tuck, E. Perez, I.T. Horváth, R.A. Sheldon, and M. Poliakoff. Valorization of biomass: Deteriving more value from waste. Science, 337:695–699, August 2012.

[131] K.N. Urness, Q. Guan, A. Golan, J.W. Daily, M.R. Nimlos, J.F. Stanton, M. Ahmed, and G.B. Ellison. Pyrolysis of furan in a microreactor. Journal of Chemical Physics, 139:124305, 2013.

[132] K.N. Urness, Q. Guan, A.K. Vasiliou, A. Golan, M. Ahmed, D.L. Osborn, J.F. Stanton, J.W. Daily, and G.B. Ellison. Temperature measurement in a microtubular flow reactor. In Symposium on Gas Kinetics, Boulder, CO, June 2012. Royal Society of Chemistry.

[133] K.N. Urness, T.P. Troy, M. Ahmed, J.W. Daily, G.B. Ellison, and J.M. Simmie. Pyrolysis of 2-methoxyfuran. Journal of Physical Chemistry A, to be submitted, 2014.

[134] U.S. Energy Information Agency. International energy statistics. www.eia.gov/cfapps/ipdbproject, accessed May 13th, 2014.

[135] H. Van Dam and A. Oskam. He(I) and He(II) photoelectron-spectra of some substituted ethylenes. Journal of Electron Spectroscopy and Related Phenomena, 13(4):273–290, 1978.

[136] A.K. Vasiliou, J. Kim, T.K. Ormond, K.M. Piech, K.N. Urness, A.M. Scheer, D.J. Robichaud, C. Mukarakate, M.R. Nimlos, J.W. Daily, H.-H. Carstensen, and G.B. Ellison. Biomass pyrolysis: Thermal decomposition mechanisms of furfural and benzaldehyde. Journal of Chemical Physics, 139:104310, 2013.

[137] A.K. Vasiliou, M.R. Nimlos, J.W. Daily, and G.B. Ellison. Thermal decomposition of furan generates propargyl radicals. Journal of Physical Chemistry A, 113:8540–8547, 2009.

[138] A.K. Vasiliou, K.M. Piech, B.E. Reed, X. Zhang, M.R. Nimlos, M. Ahmed, A. Golan, O. Kostko, D.L. Osborn, D.E. David, K.N. Urness, J.W. Daily, J.F. Stanton, and G.B. Ellison. Thermal decomposition of CH_3CHO studied by matrix infrared spectroscopy and photoionization mass spectroscopy. Journal of Chemical Physics, 137:164308, 2012.

[139] C. Wang, H. Xu, R. Daniel, A. Ghafourian, J.M. Herreros, S. Shuai, and X. Ma. Combustion characteristics and emissions of 2-methylfuran compared to 2,5-dimethylfuran, gasoline and ethanol in a DISI engine. Fuel, 103:200–211, 2013.

[140] D. Wang, D. Wang, S. Li, and Y. Li. He I photoelectron spectroscopic studies of the electronic structure of 2(3H) furanone and 2(5H) furanone. Journal of Electron Spectroscopy and Related Phenomena, 70(2):167–172, December 1994.

[141] J. Wang, B. Yang, T.A. Cool, N. Hansen, and T. Kasper. Near-threshold absolute photoionization cross-sections of some reaction intermediates in combustion. International Journal of Mass Spectrometry, 269:210–220, 2008.

[142] K. Watanabe. Ionization potential of some molecules. Journal of Chemical Physics, 26(3):542–547, March 1957.

[143] L. Wei, C. Tang, X. Man, X. Jiang, and Z. Huang. High-temperature ignition delay times and kinetc study of furan. Energy and Fuels, 26:2075–2081, April 2012.

[144] G. D. Willett and T. Baer. Thermochemistry and dissociation dynamics of state-selected C_4H_4X ions. 2. Furan and 3-butyn-2-one. Journal of the American Chemical Society, 102:6769–6773, 1980.

[145] J.L. Wiza. Microchannel plate detectors. Nuclear Instruments and Methods, 162:587–601, 1979.

[146] X.S. Wu, R. Daniel, G.H. Tian, H.M. Xu, Z.H. Huang, and D. Richardson. Dual-injection: The flexible, bi-fuel concept for spark-ignition engines fueled with various gasoline and biofuel blends. Applied Energy, 88:2305–2314, 2011.

[147] X.S. Wu, Z.H. Huang, X.G. Wang, C. Jin, C.L. Tang, L.X. Wei, and C.K. Law. Laminar burning velocities and flame instabilities of 2,5-dimethylfuran-air mixtures at elevated pressures. Combustion and Flame, 158(3):539–546, 2011.

[148] X.S. Wu, Z.H. Huang, T. Yuan, K.W. Zhang, and L.X. Wei. Identification of combustion intermediates in a low-pressure premixed laminar 2,5-dimethylfuran/oxygen/argon flame with tunable synchrotron photoionization. Combustion and Flame, 156:1365–1376, 2009.

[149] J. Würmel and J.M. Simmie. Decomposition of lactones. To be submitted, 2014.

[150] J. Würmel and J.M. Simmie. Thermochemistry and kinetics of angelica and cognate lactones. Journal of Physical Chemistry A, 118(23):4172–4183, 2014.

[151] R. Xing, W. Qi, and G.W. Huber. Production of furfural and carboxylic acids from waste aqueous hemicellulose solutions from the pulp and paper and cellulosic ethanol industries. Energy and Environmental Science, 4:2193–2205, 2011.

[152] X. Xing, M.-K. Bahng, B. Reed, C.S. Lam, K.-C. Lau, and C.Y. Ng. Rovibrationally selected and resolved pulsed field ionization-photoelectron study of propyne: Ionization energy and spin-orbit interaction in propyne cation. Journal of Chemical Physics, 128:094311, 2008.

[153] X. Xing, B. Reed, M.-K. Bahng, and C.Y. Ng. Infrared-vacuum ultraviolet pulsed field ionization-photoelectron study of $C_2H_4^+$ using a high-resolution infrared laser. Journal of Physical Chemistry A, 112(12):2572–2578, 2008.

[154] Z.P. Xu, C.Y. Mok, W.S. Chin, H.H. Huang, S. Li, and W. Huang. Interconversion and decomposition of furanones. Journal of the Chemical Society, Perkin Transactions 2, (4):725–729, 1999.

[155] Y. Yamamoto, M. Ohno, and S. Eguchi. Study of 5-*endo* cyclization of 5-oxapenta-2,4-dienoyl radical and related radicals by *ab initio* calculations. Unusual nonradical cyclization mechanism. Journal of Organic Chemistry, 61(26):9264–9271, 1996.

[156] B. Yang, J. Wang, T.A. Cool, N. Hansen, S. Skeen, and D.L. Osborn. Absolute photoionization cross-sections of some combustion intermediates. International Journal of Mass Spectrometry, 309:118–128, 2012.

[157] J. Zádor, C.A. Taatjes, and R.X. Fernandes. Kinetics of elementary reactions in low-temperature autoignition chemistry. Progress in Energy and Combustion Science, 37:371–421, 2011.

[158] X. Zhang, A.V. Friderichsen, S. Nandi, G.B. Ellison, D.E. David, J.T. McKinnon, T.G. Lindeman, D.C. Dayton, and M.R. Nimlos. Intense, hyperthermal source of organic radicals for matrix-isolation spectroscopy. Review of Scientific Instruments, 74(6):3077–3086, June 2003.

[159] S. Zheng, X. Wang, L. Meng, X. Cao, and D. Wang. HeI photoelectron spectroscopic (PES) and quantum chemistry study on the dimeric compound of 2(5H) furanone. Science in China (Series B), 40(6):657–662, December 1997.

[160] M. Zviely, R. Gier, E. Abushkara, A. Kern, H. Sommer, H.-J. Bertram, G.E. Krammer, C.O. Schmidt, W. Stumpe, and P. Werkhoff. Application of chromatographic and spectroscopic methods for solving quality problems in several flavour aroma chemicals. In K. Swift, editor, Advances in Flavours and Fragrances: From the senstation to the synthesis, pages 39–53, Cambridge, UK, 2001. Royal Society of Chemistry.

Appendix A

Appendix A - Calibration of the Continuous Flow Microreactor

A.1   Measurement of the Mass Discrimination Factors

An estimate of the mass discrimination factors have been determined for flow through a room temperature reactor, as shown in Fig. A.1. Under operating conditions of 100 sccm it was found using a calibrated gas mixture containing known quantities of H_2, Ar, Kr, and Xe that D_i is roughly proportional to $\sqrt{m_i/z}$. A similar approach to estimating mass discrimination factors was reported earlier [28].

The calibration mixture sampled by 19.0 eV PIMS was a mixture of rare gases and hydrogen: 9.92% H_2 + 0.505% Ar + 0.1014% Kr + 0.1012% Xe in He prepared by Matheson TRIGAS. The measured ratios in Figs. A.1 and A.2 have also been corrected for the natural abundance of each isotope: ^{40}Ar = 99.6%, ^{84}Kr = 57.0% and ^{132}Xe = 26.9%. The 1σ uncertainty limits in the exponent is primarily due to the measurement of H_2 at m/z 2. If another species was included in the calibration mix with a mass between 2 and 40 this would improve the fit. As shown in Fig. A.1, the experimental data points between 40 and 132 lie within 10% of the curve fit.

The temperature of the reactant gases will also affect the molecular motion of the supersonic expansion, impacting the mass discrimination factors. The calibrant mixture was sampled at five elevated reactor temperatures the the ratios calculated assuming a constant number density of each species, as shown in Fig. A.2. As the temperature increases this number density will change, however one would expect this to be constant throughout all
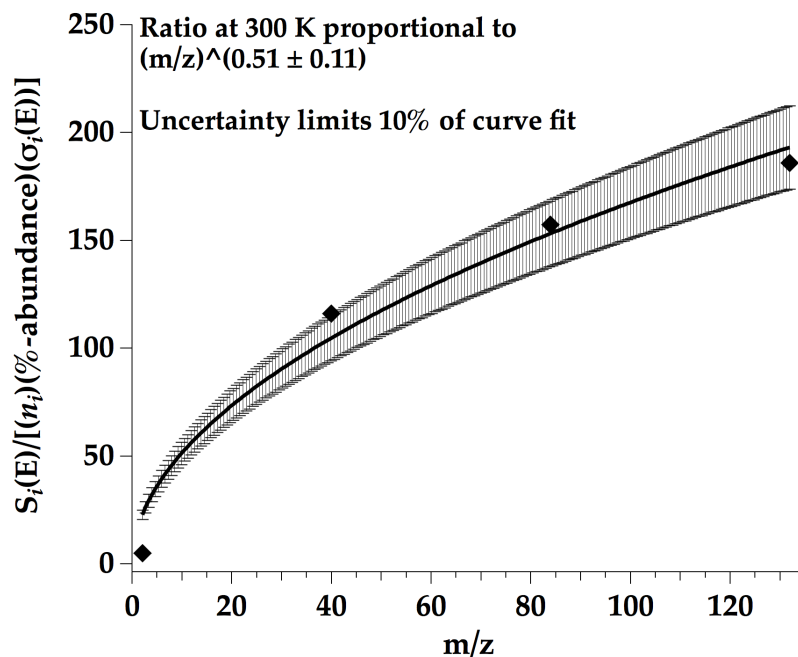
Figure A.1: Calibrated gas mixture of H_2, Ar, Kr and Xe in He sampled by 19.0 eV PIMS. Flow rate 100 sccm through a 1 mm i.d. by 3.8 cm long reactor at 300 K.
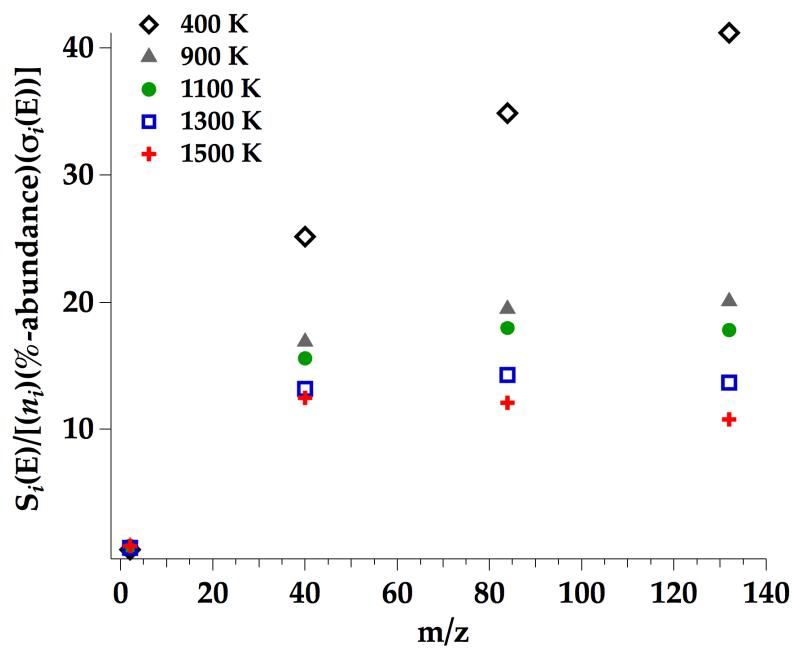
Figure A.2: The same calibrated gas mixture and the ratio measured at five elevated temperatures.

mass species. The decrease in the ratio at higher masses and elevated temperatures in Fig. A.2 indicates there may be something more complicated going on in the expansion requiring a careful calibration or use of an appropriate internal standard for measurements taken over a range of temperatures.

A.2   Pyrolysis of Cyclohexene as a Chemical Thermometer

Cyclohexene was pyrolyzed as a chemical thermometer to characterize the thermodynamic conditions and to validate simulations of the fluid dynamics in the μtubular reactor. The reaction kinetics of the retro-Diels-Alder fragmentation of cyclohexene to ethylene and 1,3-butadiene, shown below, has been used for calibration purposes in shock tube studies [128]:
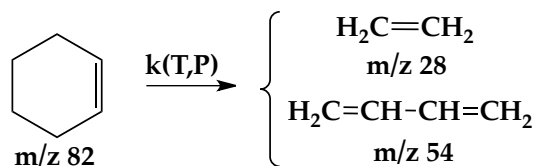
For this set of experiments cyclohexene was decomposed in a heated 1 mm x 3.8 cm silicon carbide (SiC) reactor under continuous flow conditions at 25 sccm He with a reactor wall temperature between $300-1500$ K. A 1:1 gas mixture of cyclohexene:xenon in helium emerges from the reactor as a skimmed molecular beam at a pressure of approximately 1 μTorr. Tunable VUV photoionization mass spectrometry with synchrotron radiation is used to detect cyclohexene and its decomposition products relative to the internal standard, Xe. Fig. A.3 shows thermal decomposition products at 11.0 eV, in addition to products resulting from dissociative ionization of both reactant and product molecules.

Due to the complications associated with dissociative ionization, only ethylene (m/z 28) was used to determine the extent of reaction. Dissociative ionization of cyclohexene to m/z 67 and 54 makes it difficult to distinguish between butadiene (m/z 54) produced *via* reaction and dissociative ionization of the reactant. Butadiene is also known to fragment to ethylene
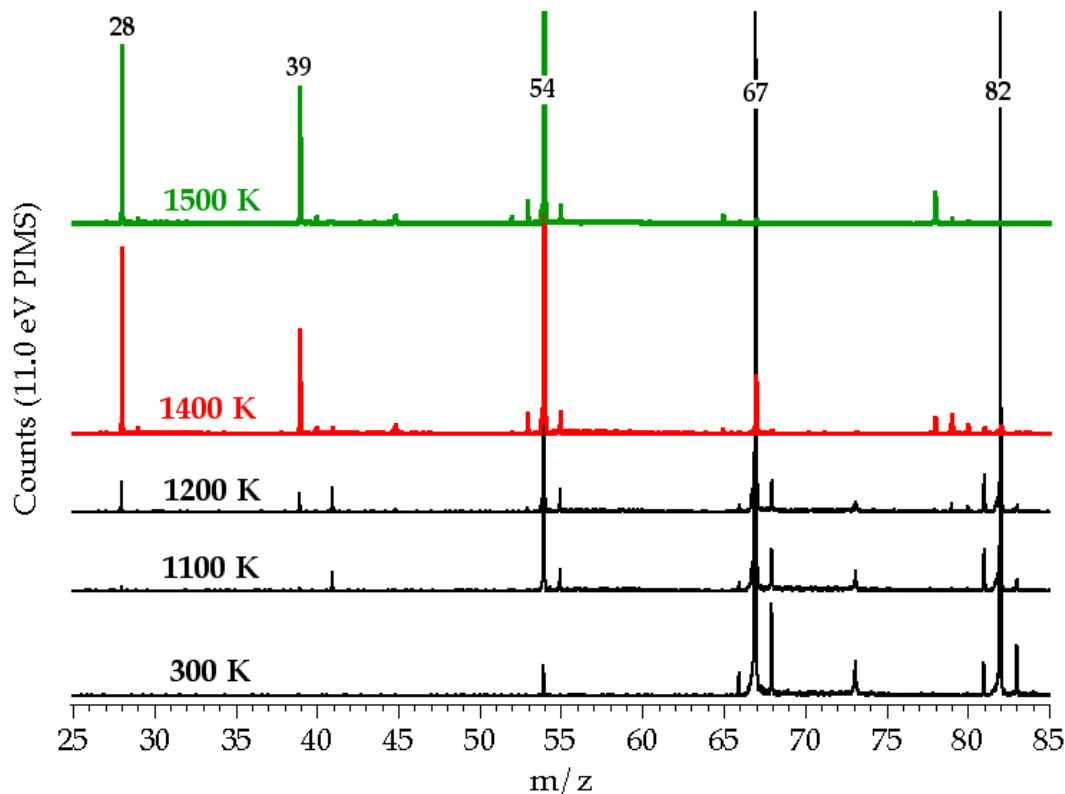
Figure A.3: Mass spectra at 11.0 eV show that cyclohexene thermally decomposes to ethylene (m/z 28) and 1,3-butadiene (m/z 54) in addition to products resulting from dissociative ionization. Reactant mixture 0.65% cyclohexene + 0.65% Xe in helium.

(m/z 28) [32] at higher photon energies, and this dissociation was enhanced with increasing reactor temperature. The level of dissociative ionization as a function of reactor temperature was estimated in a calibration of only 1,3-butadiene and xenon in He, as shown in Fig. A.4.

Fig. A.5 shows the results of ethylene produced from the thermal decomposition of cyclohexene in the μtubular reactor at several measured wall temperatures. The raw data (♦) shows that ethylene grows in with increasing temperature. The raw data has also been corrected (•) for the level of dissociative ionization to ethylene observed in the butadiene/Xe calibration. However, the 1,3-butadiene produced by thermal dissociation of cyclohexene at a given temperature is likely to be more vibrationally excited than a molecule of butadiene in the calibration gas mixture heated to the same temperature, and thus the amount of
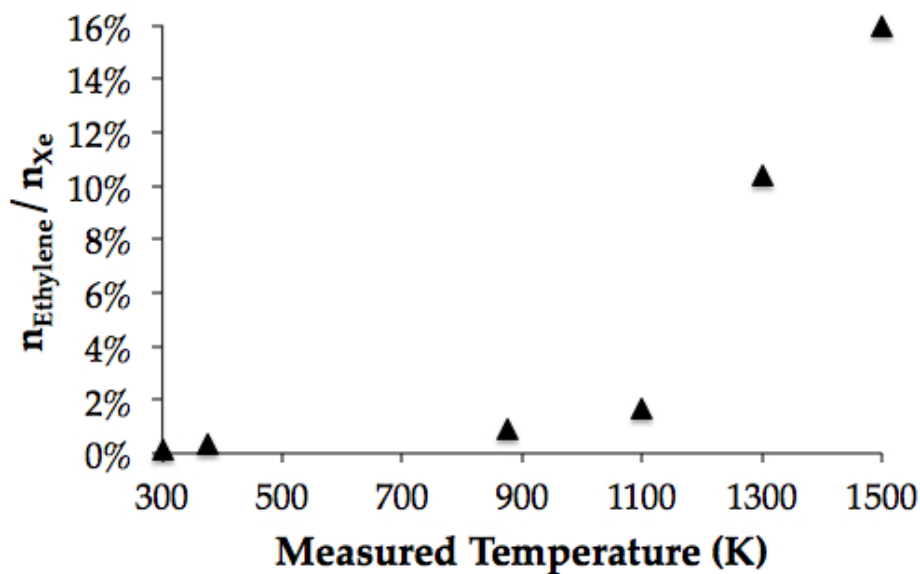
Figure A.4: Dissociative ionization of 1,3-butadiene to ethylene at 11 eV. Signal recorded as ethylene produced relative to the internal standard, Xe. Calibration mixture of 0.49% 1,3-butadiene + 0.49% Xe in helium.
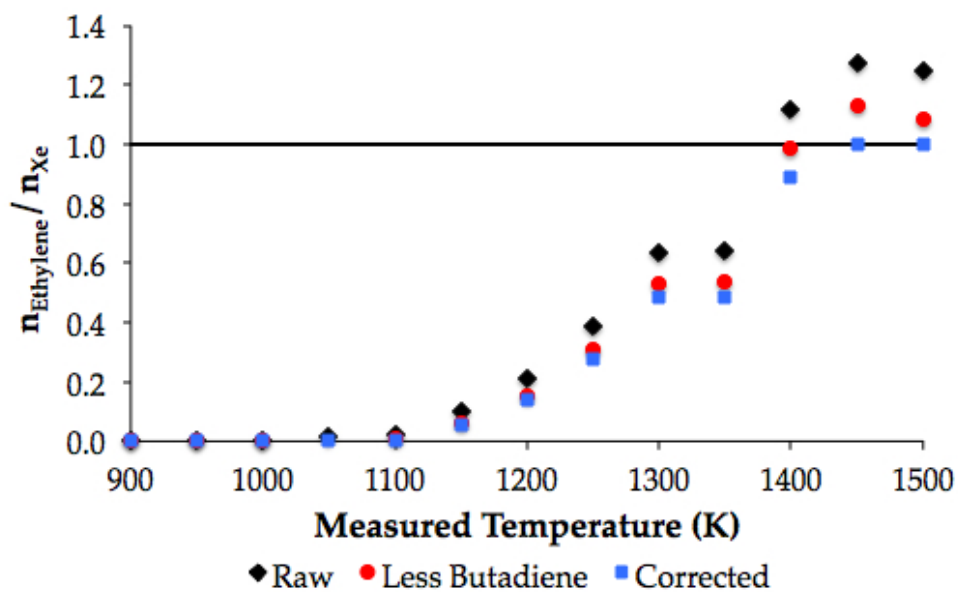
Figure A.5: Formation of ethylene with respect to Xe from 900−1500 K, including uncorrected data (♦), data corrected for additional ethylene due to dissociative ionization of product 1,3-butadiene (•), and normalized data (•). Reactant mixture was 0.65% cyclohexene and 0.65% Xe in helium.

dissociative ionization of product butadiene to ethylene is likely to be greater than in the calibration, as indicated by observed ratio greater than 1 at the upper temperatures. For this reason, the data plotted as (●) is normalized to 1 at upper temperatures when all reactant cyclohexene has been consumed.
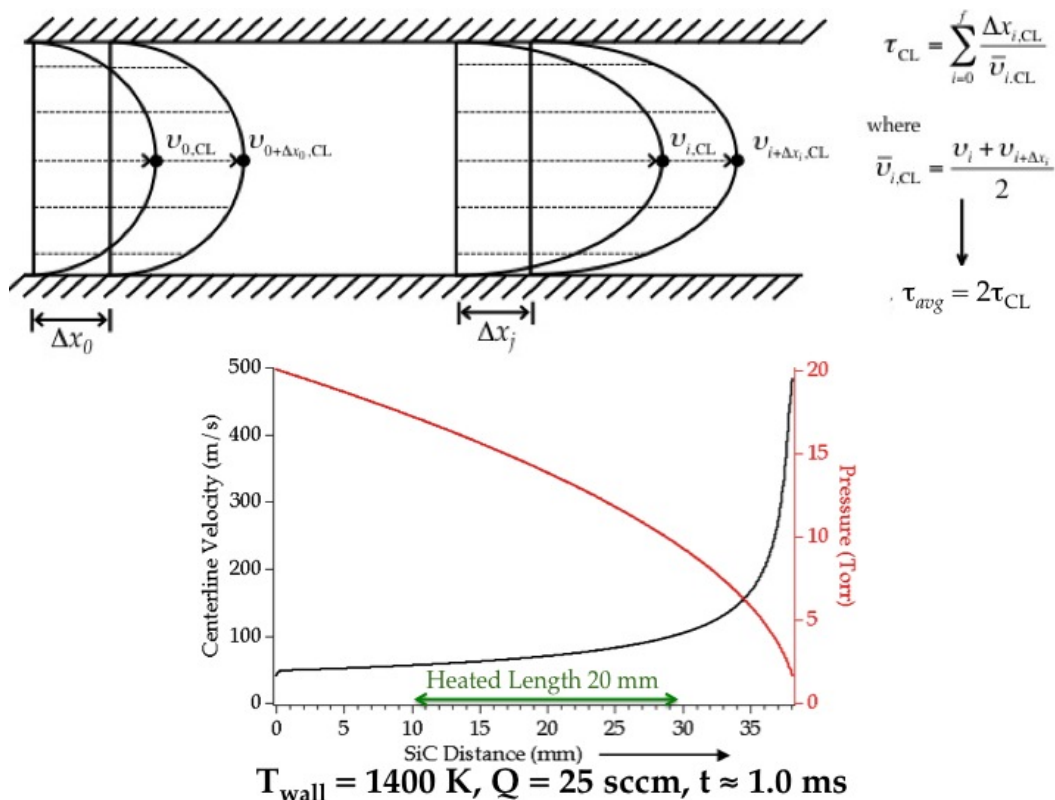
Figure A.6: Centerline pressure and velocity distribution estimates within the μtubular reactor as determined by CFD [49]. The centerline residence time was determined by calculating an average velocity at each segment of the mesh and summing the individual residence times for each grid point along the length of the reactor.

Computational fluid dynamics (CFD) was used to simulate the flow conditions in the SiC reactor because we are unable to directly measure the conditions [49]. The measured inlet pressure to the reactor was 20 Torr and an estimate of the centerline pressure and velocity distribution along the length of the reactor is shown in Fig. A.6. The information obtained by CFD provides an estimate of the residence time along the centerline under these operating conditions of 0.8 to 1.0 ms, which is about a factor of 10 longer than operation of

the reactor with a flow of 280 sccm He, as is presently done [49].

MultiWell [7] (an RRKM program) was used to calculate $k(T,P)$ for the cyclohexene reaction in the fall-off region, as shown in Fig. A.7. Quantification of the thermal dissociation is determined by the ethylene signal (C_2H_4) relative to the starting concentration of cyclohexene, resulting in a value for the rate constant, k of:

$$k = -\frac{1}{\tau} \ln\left(\frac{[C_6H_{10}]_t}{[C_6H_{10}]_0}\right) = -\frac{1}{\tau}\ln\left(\frac{1-[C_2H_4]_t}{[C_6H_{10}]_0}\right) \tag{A.1}$$

Based on the simulation of the residence time and pressure in the reactor, it is possible to extrapolate an effective temperature based on the estimated rate constant at these conditions, calculated as:

$$k(\text{T,P}) = -\frac{1}{0.001\text{s}}\ln\left(\frac{1-0.89}{1}\right) \approx 2,200\text{s}^{-1} \tag{A.2}$$

From the temperature and pressure dependence of the rate constant, the effective chemical temperature in the μtubular reactor can be deduced, as shown in Fig A.7. These experimental results show that the chemical temperature of the molecules along the centerline in the reactor is about 150 K lower than the measure wall temperature [132].

These early experimental results are promising, however the uncertainties associated with the simplification of this preliminary analysis are large and there is a need to improve these estimates. Recent simulations of the flow through the microreactor show that the low flow rate used for this set of characterization experiments resulted in non-continuum flow conditions where use of the Navier-Stokes equations do not apply. At these low flow rate conditions, the flow transitions from continuum to rarefied flow *within* the reactor, significantly increasing the difficulty to create an accurate model. For this reason the flow rate for subsequent experiments has been increased to ensure a large enough pressure-drop is achieved to choke the flow at the reactor exit and that the fluid can be modeled in the continuum region throughout the length of the reactor.

Additional studies with chemical thermometers (cyclohexene, norbornene, etc.) using GC with FID to quantify products are planned in order to reduce the uncertainty associated
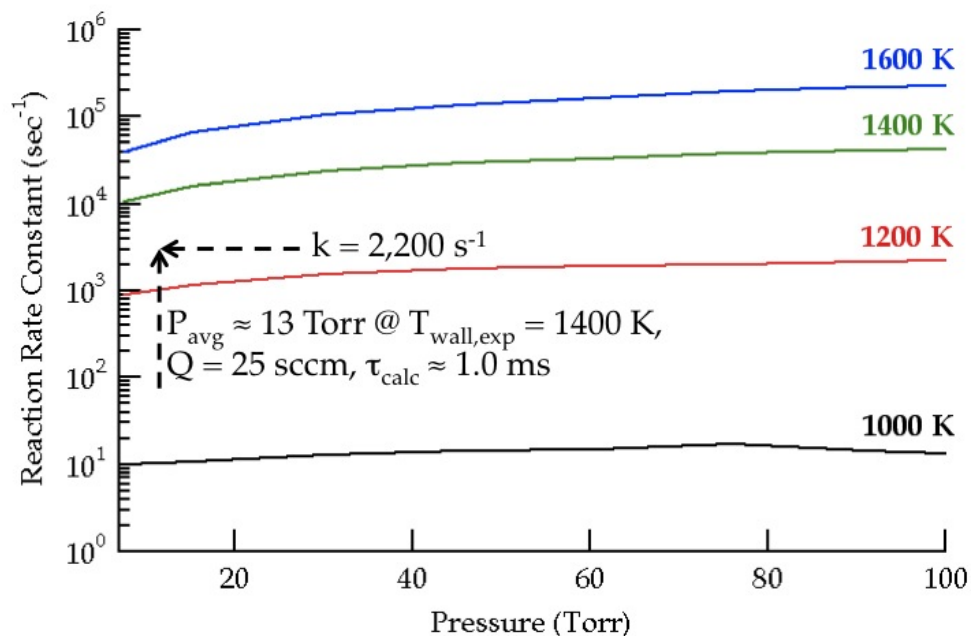
Figure A.7: A sample of MultiWell [7] calculations of $k(T,P)$ under relevant thermodynamic conditions

with using PIMS as a diagnostic technique. The ultimate goal is to integrate the variable flow conditions in the reactor with a temperature and pressure dependent rate constant $k(T,P)$ to create a fully reactive CFD simulation.

Appendix B

Appendix B - Uncertainty Analysis

There is some level of uncertainty in every laboratory measurement due to a combination of systematic and statistical errors. It is important to have a grasp on the level of uncertainty associated with a particular measurement and how that uncertainty propagates when a reported value is not a single measurement, but rather a function of several variables. The limits of uncertainty discussed in the dynamics of furan pyrolysis (Chapter 3) is further detailed here. In general, the combined relative standard uncertainty associated with the calculated number density ratio of two species can be estimated based on the relative uncertainty associated with each component in the calculation [31, 95].

Consider an equation of the form

$$y = Ax_1^a x_2^b ... x_n^p \tag{B.1}$$

where y is calculated as the product of A (a constant) and any number of variables x_n^p. The combined relative standard uncertainty can then be written as:

$$u_r(y) = \sqrt{u_r^2(x_1) + u_r^2(x_2) + \cdots + u_r^2(x_n)} = \sqrt{\sum_{i=1}^{n} u_r(x_i)} = \sqrt{\sum_{i=1}^{n} \left(\frac{u(x_i)}{|x_i|} \right)} \tag{B.2}$$

where $u_r(x_i) = u(x_i)/|x_i|$ is the relative uncertainty associated with each component x_i in Eq. (B.1).

Considering the number density for a given species n_i is of the form

$$n_i = \frac{S_i^+}{CD_i \Phi(E) \sigma_i(E)} \tag{B.3}$$

and only ratios of two species i and j are considered

$$\frac{n_i}{n_j} = \frac{S_i^+}{S_j^+} \frac{D_j \Phi_j \sigma_j}{D_i \Phi_i \sigma_i} \tag{B.4}$$

it is the relative uncertainty associated with Eq. (B.4) that must be determined.

Since the term in Eq. B.2 is squared, it becomes irrelevant to the uncertainty propagation if a term is in the numerator or denominator and therefore the combined relative uncertainty of the calculated n_i/n_j ratio, assuming the same value of $\Phi(E)$ was used, becomes

$$u_r(n_i/n_j) = \sqrt{u_r^2(\sigma_i) + u_r^2(\sigma_j) + u_r^2(S_i^+) + u_r^2(S_j^+) + u_r^2(D_j/D_i)} \tag{B.5}$$

Uncertainty estimates for the photoionization cross-section $\sigma_i(E)$ are available in literature for each species with a reported cross-section. The measured signal S_i^+ is calculated by a summation of the ion counts over a selected mass range. This summation of counts follows a Poisson process resulting in random variations in the signal. The relative uncertainty associated with this random variation is estimated as $\sqrt{S_i}/S_i$, where S_i is the observed ion signal. The larger the signal-to-noise ratio for a given ion peak, the less uncertainty there is with the signal as measured.

As described in Section 2.3.1, the fit for the mass discrimination factors D_i has been approximated as the $\sqrt{m_i/z}$, however the curve fit of the data reported the value of $D_i = (m_i/z)^{0.51 \pm 0.11}$. The value of $u_r^2(D_j/D_i)$ is determined by expanding the limits of the exponent to its upper and lower limits and calculating how this exponent affects the ratio with different masses. When comparing similar masses the relative uncertainty of this correction is minimal, as shown by the values of the relative uncertainty of D_i/D_j in Tables B.1 through B.4.

The uncertainty in the responsivity of the photodiode (measured in A W^{-1}) is reported by the manufacturer (IRD-inc.) to be $\pm$ 2% at wavelengths relevant to this work. Although as described in length in Chapter 3.3, there is an unknown systematic uncertainty with the photodiode measurements that will require further studies to quantify.

The following tables document the uncertainty in the measurement of the ratios

indicated for the furan pyrolysis experiments. Note that the temperature in these tables is reported as the measured wall temperature of the SiC reactor.

Table B.1: Uncertainty in the α-carbene channel measurement: ketene to acetylene ratio

Ratio Calculated	Relative Uncertainty							Combined Uncertainty	
	Cross Section			Signal Summation (Poisson Statistics)				@ 11.6 eV	
α-carbene	$\sigma_{CH2CO}(10.4eV)$	$\sigma_{HCCH}(11.6eV)$		1600/1500K	1400 K	1300 K	1200 K	1600 K	11.1%
$[CH_2CO]/[HCCH]$	0.039	0.052		CH$_2$CO				@ 11.7 eV	
	$\sigma_{CH2CO}(10.5eV)$	$\sigma_{HCCH}(11.7eV)$	10.4 eV	0.024	0.060	0.14	0.11	1600 K	9.3%
	0.040	0.040	10.5 eV	0.025	0.058	0.13	0.33	@ 10.4 / 11.7 eV	
	$\sigma_{CH2CO}(11.6eV)$		11.6 eV	0.027	0.059	0.10	0.10	1600/1500 K	9%
	0.059		11.7 eV	0.026	0.053	0.09	0.10	1400 K	12%
	$\sigma_{CH2CO}(11.7eV)$			HCCH				1300 K	21%
	0.037		11.6 eV	0.026	0.06	0.16	0.25	@ 10.5 / 11.7 eV	
			11.7 eV	0.022	0.05	0.13	0.22	1600/1500 K	9%
			Mass Discrimination					1400 K	12%
			D_{CH2CO}/D_{HCCH}	0.07				1300 K	20%

Table B.2: Uncertainty in the α-carbene to β-carbene channel measurements: low ionization energies

Ratio Calculated	Relative Uncertainty		Combined Uncertainty	
$[\alpha\text{-carbene}]/[\beta\text{-carbene}]$	**Cross Section**	**Signal Summation (Poisson Statistics)**	**w/ Ketene @ 10.4 eV**	
	$\sigma_{CH2CO}(10.4eV)$ $\sigma_{CH2CO}(10.5eV)$	1600 K & 1500 K	1600/1500 K	16.7%
$\dfrac{[CH_2CO]}{[HCCCH_2]+[CH_3CCH]}$	0.039 0.040		1400 K	9.3%
	$\sigma_{HCCCH2}(10.4eV)$ $\sigma_{HCCCH2}(10.5eV)$		1300 K	17.0%
	0.146 0.153		**w/ Ketene @ 10.5 eV**	
	$\sigma_{CH3CCH}(10.4eV)$ $\sigma_{CH3CCH}(10.5eV)$		1600/1500 K	17.5%
	0.057 0.065		1400 K	9.8%
	Mass Discrimination		1300 K	16.1%
	D_{alpha}/D_{beta} 0.003			

Signal Summation (Poisson Statistics):

	10.4 eV	10.5 eV
1600 K & 1500 K		
CH_2CO	0.024	0.025
$HCCCH_2$	0.031	0.028
CH_3CCH	0.014	0.013
1400 K		
CH_2CO	0.060	0.058
CH_3CCH	0.017	0.023
1300 K		
CH_2CO	0.144	0.134
CH_3CCH	0.058	0.048

Ratio Calculated	Cross Section	Combined Uncertainty
$[\alpha\text{-carbene}]/[\beta\text{-carbene}]$	$\sigma_{HCCH}(11.7eV)$	**10.4 eV / 11.7 eV**
$\dfrac{[HCCH]}{[HCCCH_2]+[CH_3CCH]}$	0.040	1600/1500 K 17.1%
	Mass Discrimination	1400 K 8.9%
	D_{alpha}/D_{beta} 0.038	1300 K 15.5%

Table B.3: Uncertainty in the α-carbene to β-carbene channel measurement: acetylene to carbon monoxide

Ratio Calculated	Relative Uncertainty			Combined Uncertainty	
$[\alpha\text{-carbene}]/[\beta\text{-carbene}]$	**Cross Section**	**Signal Summation (Poisson Statistics)**		1600/1500 K	11.7%
	$\sigma_{HCCH}(13.6eV)$ $\sigma_{CO}(14.0eV)$		CO @ 14eV HCCH @ 13.6eV	1400 K	12.1%
$[HCCH]/[CO]$	0.03 0.05	1600/1500 K	0.008 0.01	1300 K	14.2%
		1400 K	0.014 0.033		
		1300 K	0.020 0.079		
	Mass Discrimination	**Photon Energy Correction**			
	D_{HCCH}/D_{CO} 0.008	13.6/14.0 0.1			

Table B.4: Uncertainty in the radical to closed-shell channel measurements

Ratio Calculated	Relative Uncertainty			Combined Uncertainty	
Radical to Closed Shell	**Cross Section**	**Signal (Poisson Statistics)**		**Lower Limit**	**10.4 eV**
	$\sigma_{HCCH2}(10.4eV)$ $\sigma_{HCCH2}(10.5eV)$	1500 K	10.4 eV	1600	52.5%
$[HCCCH_2]/[CH_3CCH]$	0.146 0.153	$HCCCH_2$	0.059	1500	52.8%
	$\sigma_{CH3CCH}(10.4eV)$ $\sigma_{CH3CCH}(10.5eV)$	CH_3CCH	0.015	**Upper Limit**	**10.4 eV**
	0.057 0.065			1600	16.0%
	Mass Discrimination	**Dissoc. Ionization 10.4 eV**		1500	16.8%
	D_{39}/D_{40} 0.003	0.500			

Appendix C - Additional Spectra and Tables

C.1 Supplemental Spectra for 2-Methoxyfuran
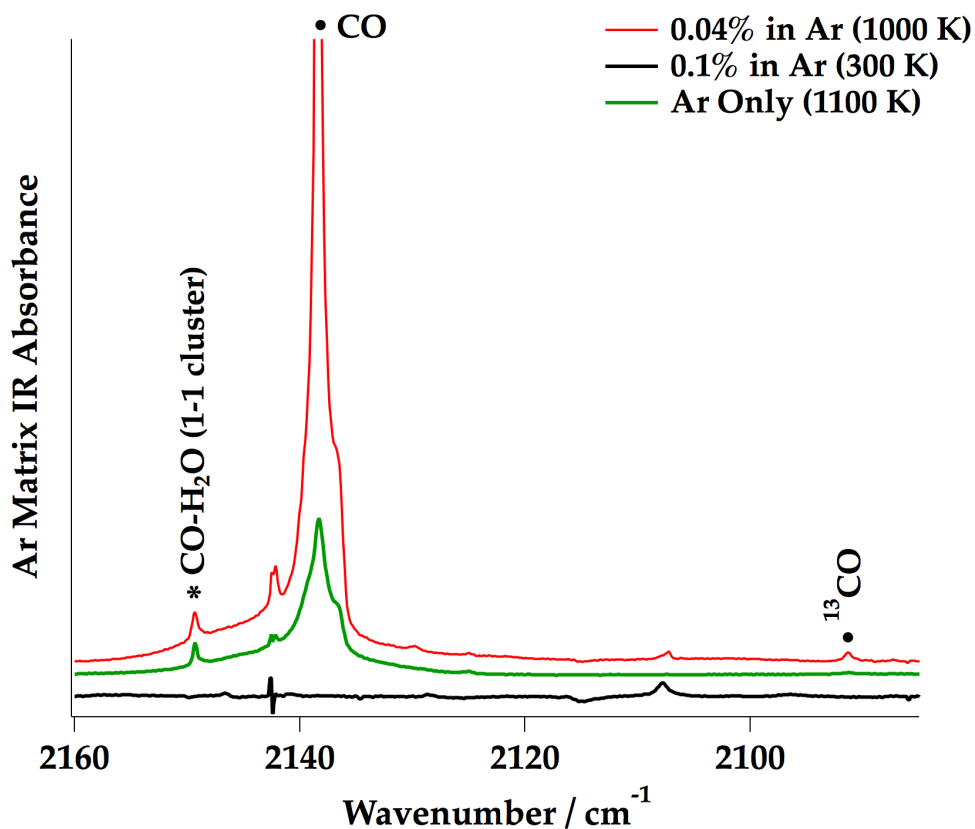
Figure C.1: FT-IR product spectrum of the CO region produced from heated methoxyfuran in Ar. Shown for comparison are scans of only Ar through a heated reactor and methoxyfuran in Ar through a room temperature reactor.
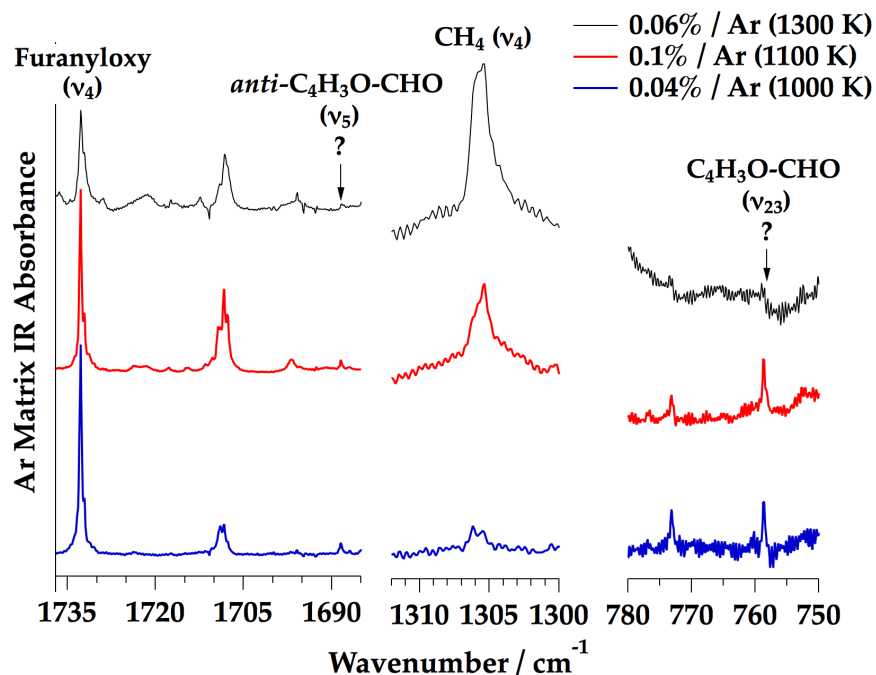
Figure C.2: FT-IR product spectra show trace absorbance features of methane and the possibility of furfural due to hydrogen abstraction reactions.
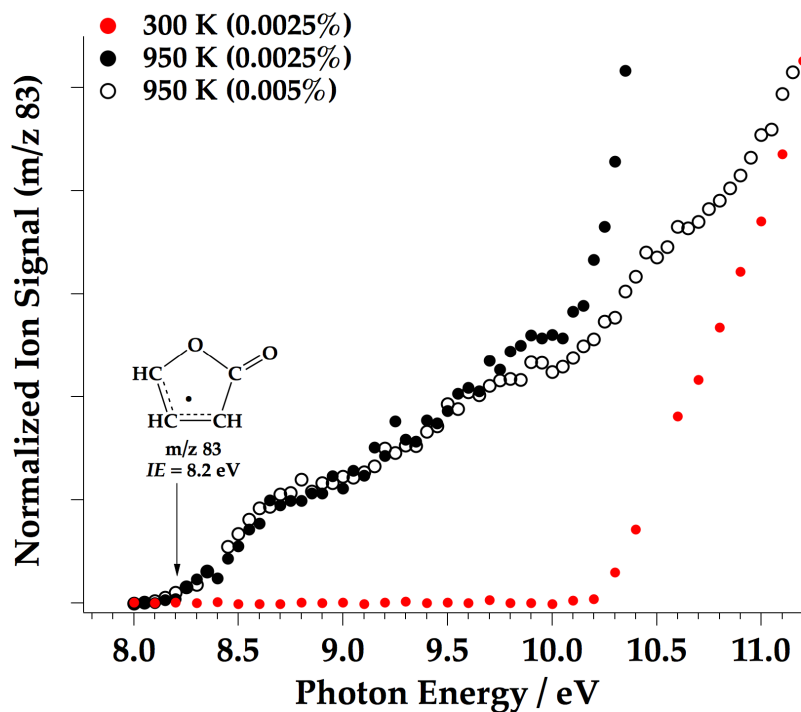
Figure C.3: Photoionization efficiency curves of m/z 83 at 300 K and 950 K deomonstrate m/z from dissociative ionization of 2-methoxyfuran. Dilute mixture pyroylzed at 950 K (solid black) also shows rise in signal at 10.2 eV, indicating unreacted methoxyfuran is present.

C.2 Supplemental Infrared Spectra for Lactones

The following several pages include supporting infrared spectra for the furanone and angelica lactone pyrolysis experiments.
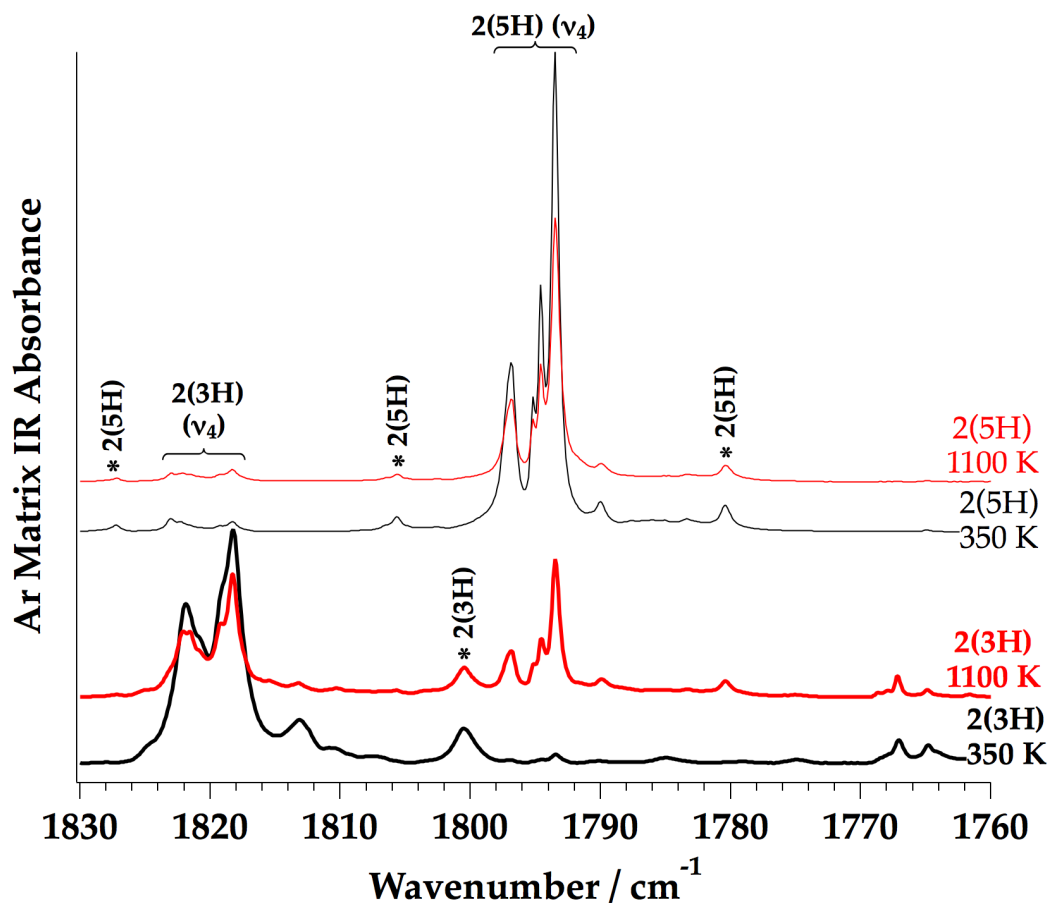
Figure C.4: Infrared spectra of the carbonyl region of both 2(3H)- and 2(5H)-furanone through a 350 K or 1100 K reactor (approximately 0.1% reactant in Ar). Assignments of 2(5H)-furanone from Breda *et al.* [19]; 2(3H)-furanone assignments guided by the harmonic frequencies of Würmel *et al.* [150]; (*) indicates possible satellite features due to the anharmonicity of the C=O stretch (see Tables C.4 and C.5 in Appendix C).
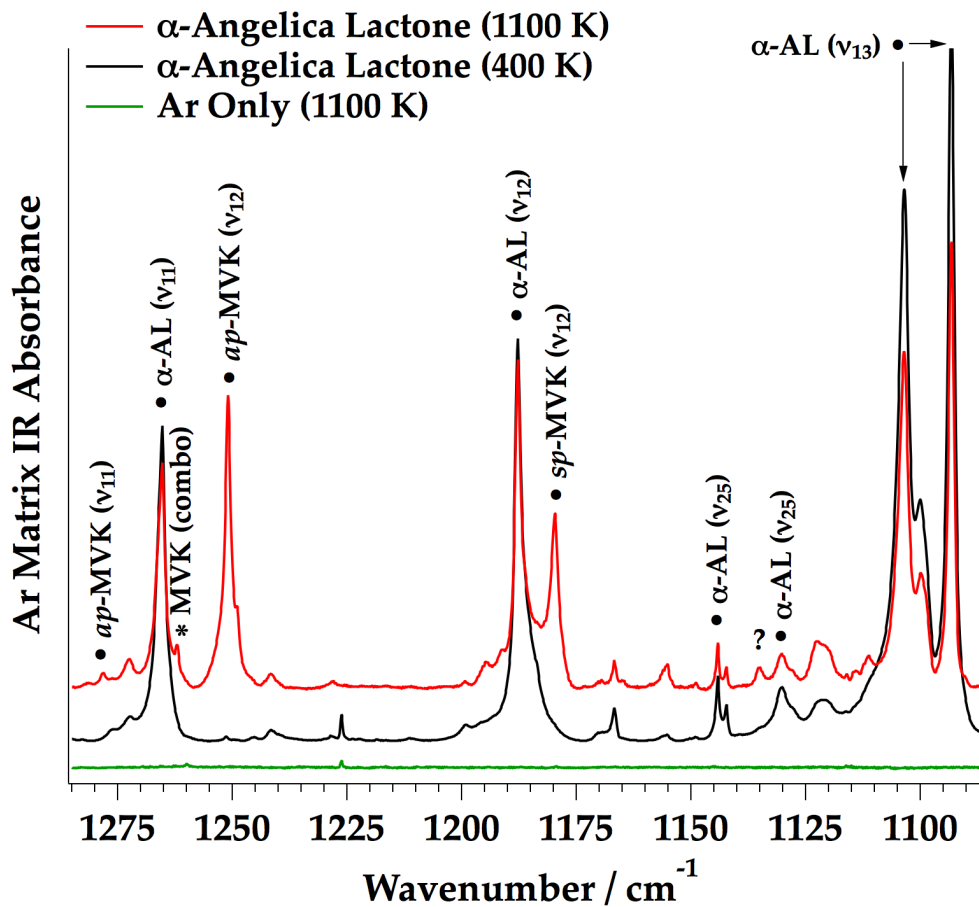
Figure C.5: Infrared product spectrum of α-angelica lactone (α-AL); MVK identified in an Ar matrix. Features marked with (*) are not fundamentals of MVK, but are observed from authentic samples. Approximately 0.1% α-AL in Ar.
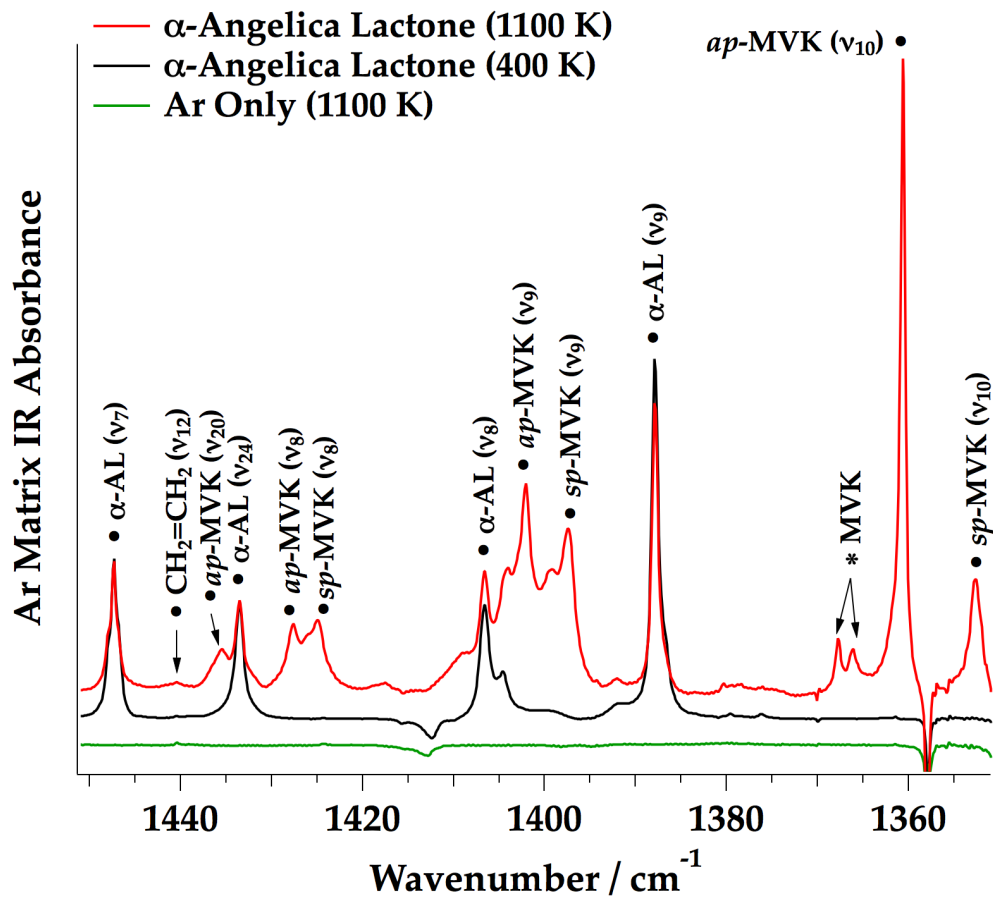
Figure C.6: Infrared product spectrum of α-angelica lactone (α-AL); MVK identified in an Ar matrix. Features marked with (*) are not fundamentals of MVK, but are observed from authentic samples. Approximately 0.1% α-AL in Ar.
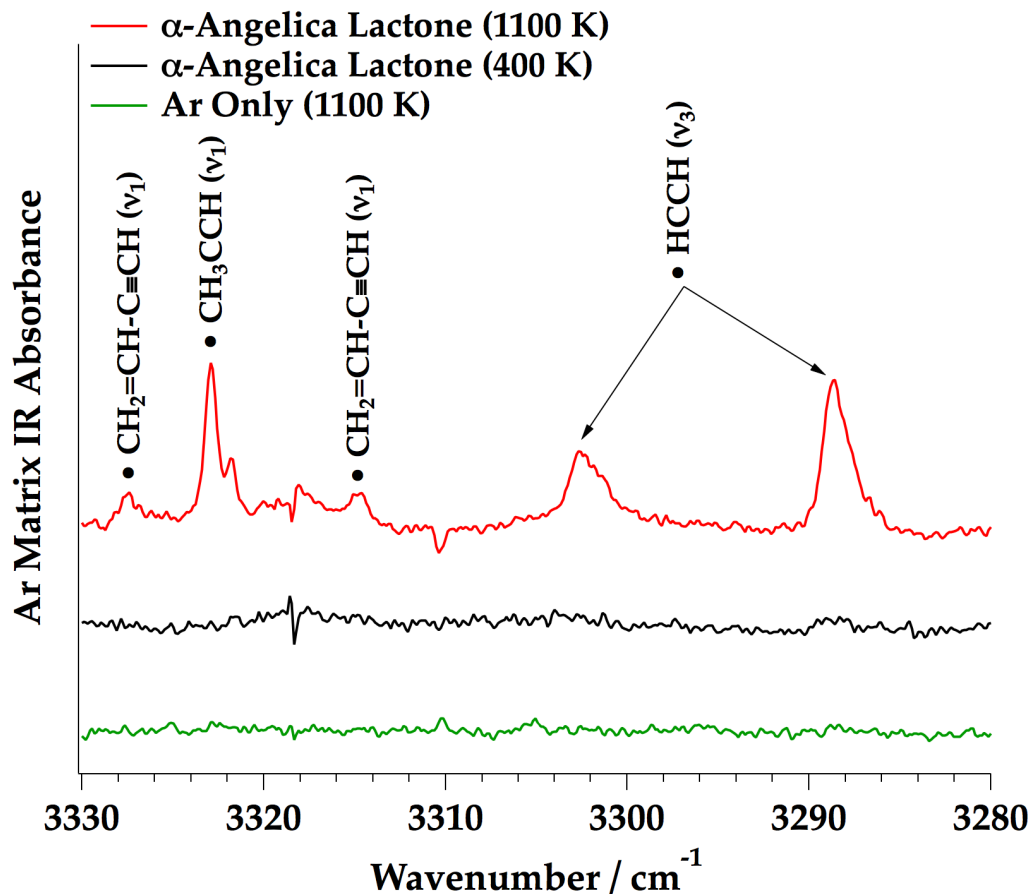
Figure C.7: Infrared product spectrum of α-angelica lactone shows acetylene (HC≡CH) and trace amounts of methylacetylene (CH$_3$CC≡H) and vinylacetylene (CH$_2$=CH-C≡H). Approximately 0.1% α-AL in Ar; assignment of vinylacetylene determined by authentic samples [113].
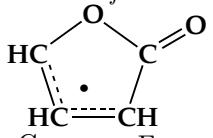
C.3   Tables of Infrared Frequencies

Included in this section are tables of vibration frequencies for 2-furanyloxy radical, acrolein, methyl vinyl ketone, 2(5H)-furanone, 2(3H)-furanone and α-angelical lactone (5-methyl-2(3H)-furanone). The column header 'IR Ar (Urness)' refers to observations from this work.

The tables of frequencies are not included for crotonaldehyde because there are no strong absorption features observed beyond the carbonyl stretch at 1709.4 cm^{-1}

Table C.1: Calculated harmonic frequencies of 2-furanyloxy radical [119] and assignments in Ar.

Calculations: Simmie, Somers, Yasunaga, Curran.
International Journal of Chemical Kinetics, 45, pp 531-541, 2013

Symmetry: C_s		Frequencies in cm^{-1}		Methoxyfuran/Ar @ 1000 K
Sym. Species	Mode	B3LYP (Simmie)*	Intensity (Simmie)	IR Ar (Urness)
a'	ν_1	3183.2	0	
	ν_2	3171.6	2	
	ν_3	3155.9	0	
	ν_4	1731.6	257	1732.8 1749, 1709**
	ν_5	1455.8	17	1462.2
	ν_6	1385.3	27	
	ν_7	1313.1	18	1314 1171, 1169.8**
	ν_8	1173.8	49	1167.6
	ν_9	1081.7	3	
	ν_{10}	1044.4	16	
	ν_{11}	1019.1	19	
	ν_{12}	849.5	10	
	ν_{13}	718.1	30	714.3
	ν_{14}	665.8	8	
	ν_{15}	477.7	1	
a''	ν_{16}	875.7	2	
	ν_{17}	770.6	19	773.0
	ν_{18}	718.9	48	714.3
	ν_{19}	661.3	7	
	ν_{20}	512.6	13	
	ν_{21}	250.4	0	

* frequencies scaled by 0.975

** additional bands

Table C.2: Vibrational frequencies of acrolein in the gas phase [51] and Ar [16, 18, 60].

Sources: Tabulated: Bock, Panchenko, Krasnoshchiokov. *Chem Phys*, 125(1), pp 63-75, 1998.
Gas Phase IR: Hamada, Nishimura, Tsuboi. *Chem Phys*, 100, pp 365-375, 1985
Ar Matrix IR: Blom, Müller, Günthard. *Chem Phys Letters*, 73(3), pp 483-486, 1980.
Ar Matrix IR: Johnstone, Sodeau. *J Chem Soc Faraday Trans*, 88(3), pp 409-415, 1992

Symmetry: C_s			trans-CH_2=CH-CHO / cm^{-1}			cis-CH_2=CH-CHO / cm^{-1}			
Sym. Species	Mode	Approximate Assignment	IR Gas (Hamada)	IR Ar* (Blom)	IR Ar (Urness)	IR Gas (Hamada)	IR Ar** (Blom)	IR Ar (Johnstone)	IR Ar (Urness)
a'	ν_1	ν(=CH_2) asym.	3103						
	ν_2	ν(C-H) vinyl	3069						
	ν_3	ν(=CH_2) sym.	2998						
	ν_4	ν(C-H) formyl	2800				2838		
	ν_5	ν(C=O)	1724	1706	1708.3		1709	1715.7	1714.9
					1707.7			1714.3	1714.3
	ν_6	ν(C=C)	1625				1612	1616.9	
	ν_7	δ(CH_2) sc.	1420	1418	1418.9		1402	1405.3	
	ν_8	δ(C-H) formyl	1360	1362	1361.5			1397.7	
					1359.5				
	ν_9	δ(C-H) vinyl	1275	1276.1	1276.1	1288	1285	1286.7	
	ν_{10}	ν(C-C)	1158	1157.2	1157.3	919	935	914.8	914.3?
								916.6	917.6?
	ν_{11}	ρ(=CH_2)	912		910.3		1056	1052.4	
					908.8				
	ν_{12}	δ(O=C-C)	564				669	672.4	
	ν_{13}	δ(C=C-C)	324				284		
a''	ν_{14}	γ(C-H) vinyl	993	1001	999.6		990	985.4	984.3
	ν_{15}	γ(C-H) formyl	972			989	-	1005.9	
	ν_{16}	γ(=CH_2)	959	965	957.7	968	978	970.0	968.2
	ν_{17}	τ(=CH_2)	593			542	550	546.3	
	ν_{18}	τ(C-C)	158						

ν = stretching γ = wag   *read from Fig 1 of Blom and inferred from text
δ = bending/deformation   ** tabulated values in Bock
ρ = rocking τ = torsion

Table C.3: Vibrational frequencies of methyl vinyl ketone in the gas phase [36] and in Ar [108]. Conformers: ap = antiperiplanar, sp = synperiplanar

Symmetry: C_s

Sym. Species	Mode	ap-CH₃-CO-CH=CH₂ (s-$trans$) / cm⁻¹ Approximate Assignment*	IR Gas (Durig)	Argon (Sankaran)	Intensity (Sankaran)	IR Ar (Urness)	sp-CH₃-CO-CH=CH₂ (s-cis) / cm⁻¹ Approximate Assignment*	IR Gas (Durig)	Argon (Sankaran)	Intensity (Sankaran)	IR Ar (Urness)
a'	ν_1	ν(=CH₂) asym.	3105	3104.5	4.5	3104.3	ν(=CH₂) asym.	(3105)	3113.9	0.2	-
	ν_2	ν(C-H)	3036	3056.3	0.3	3056.5	ν(C-H)	(3036)	3038.6	0.7	3038.9
	ν_3	ν(=CH₂) sym.	3019	3015.8	5.0	3016.1	ν(=CH₂) sym.	(3019)	3026.9	2.4	3027.1
	ν_4	ν(CH₃) asym.	2996	3015.8	5.0	-	ν(CH₃) asym.	(2996)	2991.7	0.3	-
	ν_5	ν(CH₃) sym.	2936	2932.6	0.8	2932.8	ν(CH₃) sym.	(2936)	2926.6	0.4	-
	ν_6	ν(C=O)	1705	1696.1	208.0	1696.7	ν(C=O)	1729	1717.6	123.7	1717.7
		combo band?	-	1691.1		1691.2					
	ν_7	ν(C=C)	1620	1657.8	8.3	1658.1	ν(C=C)	(1620)	1623.3	107.3	?
	ν_8	δ(CH₃) asym.	1426	1427.6	3.8	1427.7	δ(CH₃) asym.	(1426)	1424.5	12.2	1424.9
	ν_9	δ(CH₂) sym.	1400	1402.0	34.9	1402.1	δ(CH₂) sym.	(1400)	1396.7	42.1	1397.3
	ν_{10}	δ(CH₃) sym.	1355	1360.6	53.5	1360.7	δ(CH₃) sym.	(1355)	1352.0	29.6	1352.6
	ν_{11}	ν(C-C) sym., ν(CC(O)C) asym.	1283	1278.1	2.5	1278.2	ρ(CH)	1298	1297.9	1.8	1298.1
	ν_{12}	ρ(CH)	1249	1250.9	78.4	1251.0	γ(C-C) asym. / γ(C-CH₃)	1218	1179.5	104.9	1179.6
	ν_{13}	ρ(C-C)	1062	1053.4	3.4	1053.3	ρ(CH₂)	1180	1064.3	6.4	1064.3
	ν_{14}	ρ(CH₃)	1026	1023.1	10.2	1023.4	ρ(CH₃)	(1026)	1019.2	4.5	1019.6
	ν_{15}	ν(CC(O)C) sym.	758	758.2	3.1	757.9	ν(CC(O)C) sym.	772	774.6	3.0	775.0
	ν_{16}	δ(C-C-C=O)	530	526.7 (?)	7.2	-	δ(C-C=O)	609	601.0	20.9	601.0
	ν_{17}	δ(C-C-CH₃), δ(C-C=C)	492	-			δ(C-C-CH₃), δ(C-C=C)	492	-		
	ν_{18}	δ(C-C=C), δ(C-C-CH₃)	413	-			δ(C-C=C), δ(C-C-CH₃)	422	-		
a''	ν_{19}	ν(CH₃) asym.	2971	2979.1	3.6	2978.9	ν(CH₃) asym.	(2971)	2967.3	4.2	2967.8
	ν_{20}	δ(CH₃) asym.	1437	1435.5	8.1	1435.6	δ(CH₃) asym.	(1437)	1445.9	1.7	1445.8
	ν_{21}	τ(C=C), γ(CH₂)	1002	1005.1	3.2	1005.1	γ(CH₂)	1002	993.0	3.2	993.2
	ν_{22}	γ(CH₂)	987	999.0	23.1	999.1	ρ(CH₃)	987	987.0	32.7	987.3
		Fermi resonance band		951.3		951.6					
	ν_{23}	ρ(CH₃)	950	935.6	18.2	935.4	τ(C=C), γ(C-H)	968	967.2	25.2	967.5
	ν_{24}	γ(C-H), τ(C=C)	691	-			γ(C-H), τ(C=C)	662	668.0	8.2	668.1
	ν_{25}	γ(C=O)	292	-			γ(C=O)	272	-		
	ν_{26}	τ(CH₃)	125	-			τ(CH₃)	121	-		
	ν_{27}	τ(C-C)	116	-			τ(C-C)	87	-		

* Assigments from de Smedt

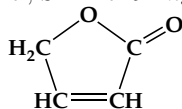ν = stretching γ = wag
δ = bending τ = torsion
ρ = rocking

(---) indicates same as ap-MVK

Table C.4: Calculated harmonic frequencies of 2(5H)-furanone [150] and assignments in Ar [19].

Sources:
Ar Matrix: Breda, Reva, Fausto. *Journal of Molecular Structure* 887 (2008) 75-86
Calculations: Würmel, Simmie. *J Phys Chem A* 118 (2014) 4172-4183

H₂C—O—C=O / HC=CH (2(5H)-furanone ring structure)

Symmetry: C$_s$ Frequencies in cm^{-1}

Sym. Species	Mode	IR Ar (Breda)	Intensity (Breda)	B3LYP (Simmie)*	Intensity (Simmie)	IR Ar (Urness)
a'	ν_1	-		3216	0	-
	ν_2	-		3178	2	-
	ν_3	2877.9	7.9	2998	23	2877.9
	ν_4	1796.8, 1793.5	479.2	1844	448	1796.9, 1793.5
	**	1925.5, 1827.2	11.2, 3.7			1925.5, 1827.3
	**	1823.0, 1805.5	6.8, 11.8			1823.0, 1805.7
	**	1780.3, 1751.2	33.6, 36.7			1780.5, 1751.3
	**	1726.7	12.4			1726.6
	ν_5	1610.8	3.1	1643	7	1610.8
	ν_6	1454.4	15.2	1476	7	1454.6
		1362.6	4.8			1362.6
	ν_7	1343.6	18.1	1352	7	1343.6
	ν_8	1330.3	8	1335	11	1330.3
	ν_9	1142.2	103.3	1130	61	1142.3
	ν_{10}	1097.6	73.4	1098	80	1097.9
	ν_{11}	1043.1	70.3	1046	51	1043.1
	ν_{12}	938.4	4.3	936	1	938.3
		881.6	1.9			881.8
	ν_{13}	866.5	49.2	862	43	866.5
		813	2.5			812.9
	ν_{14}	783.2	3.7	785	2	783.2
	ν_{15}	687.2	3.7	689	3	687.3
	ν_{16}	-		490	3	-
a"	ν_{17}	2935.1	5.5	3029	15	2935.3
	ν_{18}	1164.9, 1159.0	11.2	1192	0	1164.8, 1159.3
	ν_{19}	1008.3	6.8	1018	8	1008.2
	ν_{20}	938.4	4.3	960	4	938.3
	ν_{21}	804.9	51	810	47	805.0
	ν_{22}	660.4	6.8	668	6	660.6
	ν_{23}	-		346	6	-
	ν_{24}	-		204	0	-

* frequencies scaled by 0.99
** satellite bands of ν_4

Table C.5: Calculated harmonic frequencies of 2(3H)-furanone [150] and assignments in Ar.

Calculations:

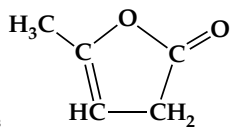Würmel, Simmie. *J Phys Chem A* 118(23) (2014) 4172-4183

Symmetry: C_s Frequencies in cm^{-1}
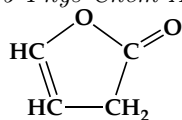
Sym. Species	Mode	B3LYP (Simmie)*	Intensity (Simmie)	IR Ar (Urness)
a'	ν_1	3229	4	-
	ν_2	3205	0	-
	ν_3	3014	6	-
	ν_4	1874	379	1818.2
	**			1764.8, 1767.1
	**			1800.6, 1821.9
	**			1866.7
	ν_5	1656	27	1618.1
	ν_6	1427	11	1403.5
	ν_7	1352	5	1345.5
	ν_8	1269	21	1256.3
				1245.4
	ν_9	1160	61	1150.2
	ν_{10}	1086	91	1093.2
	ν_{11}	1040	138	1039.1
	ν_{12}	975	25	982.9
				979.3, 975
	ν_{13}	833	29	831.0
	ν_{14}	800	23	803.5
	ν_{15}	669	8	669.9
	ν_{16}	487	2	-
a''	ν_{17}	3042	3	-
	ν_{18}	1152	4	1149.4 (sh)
	ν_{19}	954	0	-
	ν_{20}	912	2	-
	ν_{21}	721	23	708.0
	ν_{22}	565	18	-
	ν_{23}	438	13	-
	ν_{24}	172	2	-

* frequencies scaled by 0.99

** satellite bands of ν_4

Table C.6: Calculated harmonic frequencies of α-angelica lactone [150] and assignments in Ar.

Calculations:

Würmel, Simmie. *J Phys Chem A* 118(23) (2014) 4172-4183

H₃C, O, =O
C, C
Symmetry: C$_s$ HC—CH₂   Frequencies in cm^{-1}

Sym. Species	Mode	B3LYP (Simmie)*	Intensity (Simmie)	IR Ar (Urness)
a'	ν_1	3205	3	-
	ν_2	3094	13	-
	ν_3	3009	11	2940.7
	ν_4	3002	14	2935.2
	ν_5	1871	396	1822.1
				1842.1
	ν_6	1714	40	1687.4
				1690.7
	ν_7	1473	7	1447.3
	ν_8	1431	8	1406.6
	ν_9	1408	13	1387.9
	ν_{10}	1307	31	1296, 1292
	ν_{11}	1276	38	1265.3
	ν_{12}	1189	56	1187.8
	ν_{13}	1089	153	1093.3
				1103.5, 1100.1
	ν_{14}	1022	4	1015.1
	ν_{15}	974	31	974.3
	ν_{16}	937	110	939.8
	ν_{17}	824	28	826.4
	ν_{18}	693	6	695
	ν_{19}	597	5	599.8
	ν_{20}	512	4	-
	ν_{21}	294	0	-
a"	ν_{22}	3053	11	-
	ν_{23}	3035	4	2975.8
	ν_{24}	1456	9	1433.6
	ν_{25}	1150	2	1144.2, 1130.5
	ν_{26}	1062	3	1044, 1043
	ν_{27}	955	0	-
	ν_{28}	749	30	732.6
	ν_{29}	594	4	-
	ν_{30}	517	2	-
	ν_{31}	233	8	-
	ν_{32}	183	3	-
	ν_{33}	147	0	-

* frequencies scaled by 0.99